Probing nuclear effects on π^+ production with CLAS and enabling new HEP experiments with precision timing

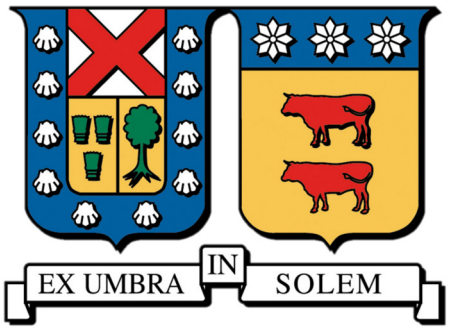

Claudio San Martín Valenzuela

Department of Physics

Universidad Técnica Federico Santa María

Submitted in partial satisfaction of the requirements
for the Degree of Master in Physics

Supervisor	Dr. William Brooks
Second Supervisor	Dr. Cristián Peña
Third Supervisor	Dr. Hayk Hakobyan

April, 2023

To my family and all the awesome people who supported me along this journey.

Acknowledgements

I want to acknowledge the support of CCTVal through grant ANID PIA/APOYO AFB180002 and the internal benefits given by the university.

This work would not be possible without the patience, support, and encouragement of the committee through all of this process. A special thanks to my thesis director Dr. William Brooks for all the opportunities he has given to me. I've improved and developed new skills, my English and programming to mention some, that I couldn't have done without his aid. He gave me the chance of travelling and to know and meet people and cultures I'd never thought I could one year ago. Thanks for your hospitality, patience, and for sharing part of your wisdom with me. Also, thanks for being a pretty good story teller, I still look forward to hearing more of your stories.

Ahora, en español, quiero agradecer a todas las personas que me acompañaron en este viaje. Este par (o un poco más) de años ha sido enormemente beneficioso para mi, desde lo profesional hasta lo personal. Me he visto enfrentado a desafíos completamente nuevos y creo que la escritura de este trabajo de tesis no ha sido la excepción.

Por el lado profesional, descubrí como la organización y el aprender 'dónde parar' en un trabajo es fundamental para no colapsar y poder cumplir con los objetivos. El documentar cada avance, con un simple escrito o una presentación, ayudan sobremanera a reforzar conocimientos y generar preguntas con las cuales seguir avanzando. En esta línea, me gustaría dejar documentado cómo llegué aquí y, de paso, agradecer a quienes lo hicieron posible.

Tuve la fortuna de llegar a un grupo en donde me recibieron como un miembro más desde el principio, todo gracias a la ayuda y apoyo de Hayk, de quien estoy enormemente agradecido por abrirme las puertas para ser parte de este equipo. Aprovecho de men-

cionar a algunos antiguos y actuales miembros del grupo que aportaron su granito para que este trabajo se concretara: Andrés, Jorge, Bruno, Antonio, Taya, Esteban y Matías, gracias. Lamentablemente, la pandemia complicó mi participación activa en el grupo en un principio, pero en ese periodo, bastante complicado, siempre recibí el apoyo de Jorge López, otra persona de la que estoy absolutamente agradecido y gracias a quien terminé por decidirme a trabajar con el profesor Will. Por esas cosas de la vida, el Profesor William Brooks me consideró para ser parte de otro proyecto, orientado más a hardware, pero siempre ligado al análisis de datos. Como estas oportunidades no se dan siempre, aceptar la invitación no fue difícil, y eso me llevó al segundo proyecto del cual se trata esta tesis. Nuevamente, por fortuna, caí en un grupo genial, liderado por Cristián Peña, a quien también agradezco la confianza y la paciencia que me ha entregado. Conocí a grandes profesionales en Fermilab, Chris y Ryan por nombrar algunos, y también locales como René. Entre una cosa y otra, terminé de estar encerrado 24/7 por la pandemia a una estadía de 5 meses en Fermilab. A la vuelta, ya todo más normalizado con respecto a la pandemia, llegué a trabajar por primera vez directamente a CCTVal. Aquí encontré un grupo humano gigante. Mis colegas y amigos, tanto físicos como ingenieros, me han demostrado como el trabajo en equipo de verdad logra hacer la diferencia. Esto último me lleva a la parte más personal de este tiempo.

Si estoy aquí, además de por las decisiones que me ha tocado tomar, es por el apoyo constante de un sin fin de personas. No exagero cuando digo que estos años y los recientes meses han sido los de mayor avance en mi vida, tiempos de gran aprendizaje y crecimiento. El año 2020 trajo varias cosas complicadas, que me enseñaron que uno no puede dar por sentado lo que se tiene. Hay que apreciar y aprovechar 'en el momento', porque nada cambia hasta que cambia.

Agradezco a mis amigos que me acompañaron desde el primer minuto, tanto dentro como fuera del ámbito académico. No puedo no mencionar a mis amigos *los fisikbros*, especialmente a mi grupito Gonzalo, Luciano, Ankai, Toloza, Cata y Bastián. Sus cafecitos, juegos de mesa, salidas a caminar, entrenar, conversaciones tan profundas desde temas personales o física hasta de memes y mucho más, siempre se los agradeceré, sobre todo por ser un apoyo para despejarme y aprender. Tampoco puedo olvidar a mis chicos Bari, partiendo por los colegas y amigos parte del grupo de física: Antonio y Bruno, sin lugar

a dudas ustedes mejoran la experiencia de trabajo en el centro; Estebitan, gracias por tu apoyo y consejo, siempre tienes algo que decir y de verdad que has sido un apoyo gigante. Sé que puedo esperar de ti un comentario muy culto o todo lo contrario, se agradece; Mati, gracias por las conversaciones sobre el laburo, que han sido de lo más productivas, y por los desvaríos, sobre todo cuando hablamos de las magnas obras del gran Brandon Sanderson, quien ha sido de los mayores descubrimientos del último tiempo (!). Espero con ansias ver como seguirá expandiéndose el *lore* del segundo piso.

Aunque llegaron ahora casi al final, tampoco quiero dejar de mencionar a los amigos que hice en el centro, con quienes tengo un aprecio muy especial, Jairo y Seba. En conjunto me han ayudado muchísimo, no tengo manera de retribuirles por su apoyo, especialmente en los momentos de mayor estrés.

Siempre me ha costado aceptar mi esfuerzo y darle valor a mi trabajo, pero creo que en este momento sí puedo mostrarme orgulloso de lo que he construído. Terminado este trabajo, tengo una mayor claridad de lo que es el mundo de la academia y la investigación, junto con una cantidad gigante de experiencia que espero ocupar desde ahora y en los futuros proyectos que se presenten.

Finalmente lo más importante, debo mencionar a mi familia, el apoyo fundamental que he tenido durante todo este proceso. Mi mami Myriam, mi papá Yuri, mi hermano Fabián (*my brother*) y mi cuñi Jemi. Han sido mi cable a tierra por mucho tiempo, entregándome su amor incondicional y el apoyo en los momentos más difíciles. Este avance y lo que soy, se los debo a ustedes. A mi sobrinita Sofi, que me enseñó un tipo de amor inefable y una conexión muy especial que logra recargarme en solo minutos de compañía. Agradecimientos especiales a mi Titi, mi Nina, mis primas y primos, tías y tíos, que también me demuestran constantemente su cariño y entregan soporte en cada ocación.

Como dirían mis amigos, *mucho texto*. Solo dejar mi más sincero gracias por todo y este será solo el siguiente paso de un camino que sigue y no para.

"The most important step a man can take. It's not the first one is it?
It's the next one. Always the next step."
- Brandon Sanderson (The Stormlight Archive, Oathbringer)

Abstract

Color confinement is a fundamental property of Quantum Chromo Dynamics (QCD), the theory of the strong force. Hadronization is the process whereby highly energetic quarks, stripped of most of their color fields, evolve back to color-neutral hadrons, thus satisfying confinement. This process has been studied in electro-nuclear scattering at two international laboratories by measuring the absorption or enhancement of hadrons produced in the scattering. The cross section for this process has a rigorously correct, known form that has three linearly independent terms. It has the form $A + B\,cos(\phi) + C\,cos(2\phi)$, where A, B, and C each depend on four kinematic variables, and ϕ is the azimuthal angle of the pion in the virtual-photon-nucleon reference frame. All studies of nuclear modifications of the cross section to date have been performed using only the first term. In this thesis we will extract the second term for the first time, and will constrain the third term, which is known to be small, while the second term is known to be large. This will illustrate the extent to which quantum effects are needed to describe the medium-modified scattering, which thus far have only been described using semi-classical approaches. The information gained will give a completely new way to look at the behavior of the in-medium hadronization process, helping to determine the mechanisms that enforce QCD confinement.

Table of Contents

Chapter 1

General introduction

Particle physics has been one of the most prolific branches of study in the latest years with advancements in the experimental area and successful theoretical descriptions given by the Standard Model. These experimental progress have been carried out in high technology laboratories, supported by diverse groups of multiple disciplines and from different cultures. This area of knowledge covers a variety of topics and could be split in sub-areas depending on the subject of interest, with two remarkable examples: *Nuclear Physics* and *High Energy Physics* (HEP). Both areas are not mutually exclusive, though, dealing with similar problems in the line of disentangling the basic components of matter and the way they evolve and interact with themselves and their environment.

Future experiments are designed to work in the frontier of our technological capabilities. This provides an exceptional potential for unveiling new mechanisms hidden inside nucleons or confirm/reject theories only possible with sufficiently sensitive devices. There are still some secrets to discover at the high energies regime or inner interactions only observable by means of polarization studies. All of these questions will be addressed by upgrades of current detectors and future planned ones. Major examples of this are the Electron Ion Collider (EIC) facility at Brookhaven National Laboratories that has been under construction since long ago, and the new CLAS12 detector built in replacement of the nowadays obsolete CLAS6 at Jefferson Lab.

In this work, Part I is a data analysis project of nuclear physics that describes the effects of different nuclear media in the production of positive pions (π^+) around a determined axis with the CLAS detector. Valuable information of the impact that non-measurable interactions inside the nucleon have in hadronization processes will be extracted. These

results would be an interesting starting point for future comparisons with new era data from CLAS12 and EIC. Part II introduces a new technology for sensors with excellent timing and spatial performances, along with a characterization of several samples. The first generation of this timing technology will be used in the HL-LHC upgrade soon. A good performance of these second generation samples would pave the way for their usage in future collaborations such as in EIC.

Part I

Analysis of nuclear effects in azimuthal asymmetries of π^+ off SIDIS processes with Clas

Chapter 2

Introduction

The production of charged mesons, with a special interest in π^+ as the lightest one, in Deep Inelastic Scattering processes has been widely studied in different experiments that cover varied kinematic regions. Confinement forbids us to measure sub nucleon structures directly, so we must use intricate methods to 'feel' the internal components and their inner mechanisms in an indirect way. A lot of information that can be contrasted with several theoretical models is encoded in the distribution of the hadrons produced. The CLAS spectrometer provides a good environment to test these phenomena with the capacity of housing nuclear media of diverse sizes. Unlike other similar accelerators, CLAS receives relative low energy electrons, which unlocks a kinematic sector that is not fully represented in more energetic ones. Additionally, another advantage of this configuration is the reduced contamination produced by decay of massive products.

A characterization of proper triggering for electrons and charged pions was developed by a former member of our group in [1]. In his analysis, the action of the nuclear media was accounted by the ratio of the production of π^+ with the so called *Multiplicity ratio*. A reduction in the generation of pions in bigger nuclei was found, with an accentuation at higher energies of the hadron. Other studies also demonstrated effects in the broadening of the momentum's transverse component, with bigger deviations from heavier nuclei [2]. These observations are evidence of a non-negligible contribution from internal interactions that are highly dependent on the nuclear sizes and that haven't been completely explained by theoretical models.

One of the remaining studies that could be developed with the available data is the impact of diverse nuclear environment in the generation of pions around the direction of

the virtual photon that mediates the interaction. The common representation of these kind of events include modulations around this axis that differs from a uniform distribution. Theoretical work has been devoted to understand and explain this behaviour with refined techniques. Some articles use transverse-momentum-dependent expansions and higher order contributions to predict them [3]. This would be the first time that these modulations are measured in heavier targets and at relative low energy.

In Chapter 3 a description of the state of the art in nuclear effects and azimuthal modulations is given. Chapter 4 introduces the detector and its components, as well as motivation and objectives of the experiment. In Chapters 5 and 6 the requirements for electron and pion identification are presented. Chapter 7 follows the corrections of data along with considerations. A method of quality check is introduced too. The main body of the work is in Chapter 8. A summary and outlook is discussed in Chapter 9.

Chapter 3

Physics background

3.1 Evolution of the cross section

Particle physics began as a phenomenological discipline. Back in the early XXth century, electron scattering experiments, regarded as β particles at that time, had revealed first evidence of a more complex structure of the matter[1]. Since then, numerous studies have been devoted to create models that can describe and predict the inner composition of matter and their interactions. Several attempts on this task have been successful, though always restricted to a reduced domain of energies.

The simplest model to begin with is the classical approach of a hard collision developed by E. Rutherford. The cross section has the form

$$\frac{d\sigma}{dq^2} = 4\pi\alpha^2\frac{1}{q^4}, \quad \text{or} \quad \left(\frac{d\sigma}{d\Omega}\right)_{lab} = \frac{\alpha^2}{4E^2\sin^4(\theta/2)}, \tag{3.1}$$

where α is the electromagnetic fine structure constant, E the energy of the incoming electron (equivalent to the module of its 3-momentum neglecting its mass), θ the deflection angle of the scattered electron with respect to its initial direction, and q^2 the square momentum transfer (more of it later in this chapter).

In order to avoid further misunderstandings, some conventions and notation to be used along this work will be quickly reviewed. Throughout this thesis we will work with natural units, where $c = \hbar = 1$, hence quantities such as energy, momentum, and mass

[1] Several advancements were produced before but this was the first time an experiment had clearly shown convincing evidence in line with the atomic theory.

have the same units, generally in GeV. In this case, a factor of $1/c$ and $1/c^2$ is implicit for momentum and mass, respectively.

A cross section has an intuitive interpretation as an effective area of interaction between two objects in relative motion towards each other. It relates the outgoing direction and distribution of particles after an interaction with a given incoming flux. Although this idea is easy to understand, it comes from a classical picture so its range of applicability is limited.

The development of Quantum Mechanics (QM) began gradually with studies of Max Planck and Albert Einstein between 1900 and 1905, but had to wait until mid-1920s where a complete mathematical formalism was developed by bright mind such as Niels Bohr, Erwin Schrödinger, Werner Heisenberg, Max Born, Paul Dirac, among others. This new paradigm required a new treatment of the interactions in terms of quantum numbers and abstract states in a Hilbert space. This description broke some basic conceptions of physical events and opened some philosophical discussions that continue even until today. Determinism is the key concept addressed by classical mechanics and QM introduced effects never seen before, even impossible to reproduce with the techniques available at that time, including interference phenomena, mixed states, and probabilistic events. The idea of reproducible results is at the heart of the scientific method, with its principle of falsifiability, and the proposed theory was bypassing it and producing measurable effects. Even though the non-determinism was real, events are not absolutely random and follow certain statistical distributions that could somehow fix the problem if we are good at dealing with a semi-deterministic description. In this scenario, a single event is not enough to probe a tendency but 'collective trends' is what matters.

After the intrusion of QM, efforts were put on including it in the theory of interactions. Special relativity was a new discovery too so a full scope description should have both phenomena covered. Don't forget that new models must be able to reproduce previous results as well, restricting even more the space of possibilities to test. Surprisingly enough, all of these preconditions were satisfied by the introduction of the Quantum Field Theory (QFT). The theory is built with a fundamental conceptual difference: ob-

servables are not fixed operators in time but are upgraded to fields that treat space and time on the same footing. The determination of cross section must be extended equally.

P. Dirac and E. Fermi derived an equation known as the *Fermi Golden Rule* to get the probability of evolution from an initial state i into a final one f:

$$\Gamma_{i\to f} = 2\pi \left|\langle f \left|H\right| i\rangle\right|^2 \rho(k), \tag{3.2}$$

where $\rho(k)$ is the density of states for a given momentum k and H is an operator/field representing the interaction. This quantity is related to the probability of transition from a quantum state to another [4] that is in turn related to the non trivial component of the scattering matrix. In general, the energy states are extended to a continuous spectrum, leading to a new and more general definition of cross section:

$$\frac{d\sigma}{d\Omega} = \frac{1}{64\pi^2 s}\frac{p_f}{p_i}\left|\mathcal{M}\right|^2, \quad \text{or} \quad \frac{d^2\sigma}{d\Omega dE'} = \frac{\alpha^2}{Mq^4}\frac{E'}{E}L_{\mu\nu}W^{\mu\nu}, \tag{3.3}$$

where p_i and E (p_f and E') are the magnitude of the 3-momentum and energy of the initial (final) state, $\mathcal{M}$ is the *invariant amplitude* related to the scattering matrix, M the proton mass, $L_{\mu\nu}W^{\mu\nu}$ are the leptonic and hadronic tensors contracted, and the remaining elements are defined as in Equation 3.1. An amazing consequence of this approach is that it is generic enough to be independent of the interacting particles. All that information is encoded in the invariant amplitude term and, equivalently, in the tensors that could be obtained by the use of Feynman rules.

Equation 3.3 is a wonderful result but could lack precision in certain cases. Depending on the interaction under study (electromagnetic, weak, strong, or a combination of them) the $\mathcal{M}$ element may not have a simple analytic form. This generally results in higher order loops with non negligible contributions. Some interactions such as $e^+e^- \to \mu^+\mu^-$ have an accurate description at tree level (no loop corrections) that differs from experiments by less than 10%, while others are susceptible to important corrections.

3.2 Comments on Quantum Chromodynamics

Internal symmetries in the interactions had given hints of a fundamental representation. Group theory is the mathematical tool that better reproduces these properties. The

three main interactions particles can feel at microscopic level are the electromagnetic, weak, and strong. All of them were associated with a group symmetry, $U(1)$, $SU(2)$, and $SU(3)$, that in turn has a set of quantum numbers: electric charge, weak isospin (and/or hypercharge), and color charge.

We are interested in the latter element: color. A theory of the color charge called Quantum Chromodynamics (QCD) is expected to shed light on the inner processes of the strong interaction. Its basic rules and components are derived from the group theory description. Hadrons are introduced as the particles that can feel the strong interaction. They are not fundamental entities but are composed of quarks and gluons. The former are particles with half-integer spin, thus follow Fermi-Dirac statistics and are subject to Pauli's exclusion principle. Quarks exist in six different flavours with different weights and unique quantum numbers, classified in three generations identically to leptons. Gluons are the massless bosons that mediate the interaction. Group theory predicts a total of eight gluons that, unlike photons, all could interact with hadronic matter and with themselves. This is why the strong interaction is hard to describe: self-interaction adds a huge amount of loop corrections that forbids the correct use of approximation methods. Alternative methods have been developed, say Lattice QCD and perturbative QCD (pQCD), but they generally attack limit cases where simplifications are feasible.

Among others, two main properties of QCD need to be highlighted: confinement and asymptotic freedom. The strong interaction is governed by a 'constant' factor α_s called *strong coupling constant* that defines the amount of strong coupling of the members. Though it's claimed as a constant, the magnitude of the interaction varies with respect to the total energy involved in the same sense as the other coupling factors do. Confinement is related to the impossibility of finding free quarks. Due to the large magnitude the coupling constant acquires at long distances, if someone attempts to take a quark apart, enough energy would be introduced to the system so that a new pair would be created and the individual halves would get a new partner. Asymptotic freedom refers to the opposite extreme case, where the scale of the interaction is small. At short distances, we can address the quarks as quasi-free particles and perturbative calculations are suitable.

Inelastic collisions, where the initial and final elements are not the same, are also possible with QCD. The process by which these new entities are created is called *hadronization*. These events are harder to describe in a detailed way due to the lack of information from the very interaction, hidden to any direct observation due to confinement. An indirect observation is the best we can try to get a feeling of the inner structure of nucleons.

Heuristic approaches have been introduced to test how detailed Equation 3.3 is. We can consider a modification of the fermionic current, part of the hadronic tensor, to include a structure distribution of the proton instead of the usual point-like assumption. This method already has accounted for the spin of the involved particles too, so differences might be expected with respect to the classical result. The corrections lead to the so called *Rosenbluth formula*:

$$\left(\frac{d\sigma}{d\Omega}\right)_{lab} = \left(\frac{\alpha^2}{4E^2\sin^4(\theta/2)}\right)\frac{E'}{E}\left\{\left(\frac{G_E^2 - \tau G_M^2}{1+\tau}\right)\cos^2(\theta/2) + \left(2\tau G_M^2\right)\sin^2(\theta/2)\right\}, \tag{3.4}$$

where $\tau \equiv -\frac{q^2}{4M^2}$, G_j^2 are the electric (E) and magnetic (M) form factors, and the other terms are as in the previous formulae. Interestingly enough, the classical estimation is part of the final expression but accompanied by modulations from the interaction with the electromagnetic field.

Using a generalized version of the hadronic tensor we could consider a richer internal structure of the proton. Resulting in a simple extension from the previous result

$$\left(\frac{d^2\sigma}{d\Omega dE'}\right)_{lab} = \left(\frac{\alpha^2}{4E^2\sin^4(\theta/2)}\right)\left\{W_2\cos^2(\theta/2) + 2W_1\sin^2(\theta/2)\right\}, \tag{3.5}$$

where the W_j terms are general form factors. They are not accessible theoretically without the introduction of a specific model. We can extract them from experiments, though.

3.3 Deep Inelastic Scattering and definitions

Deep Inelastic Scattering (DIS) is the study of interactions (scattering) in a sub nuclear level (deep) that leads to hadronization, thus breaking the initial configuration and leaving a final state with new particles (inelastic). Hadronization requires at least one meson or baryon to be produced. Our case of interest, and the one from which Equation 3.5 was

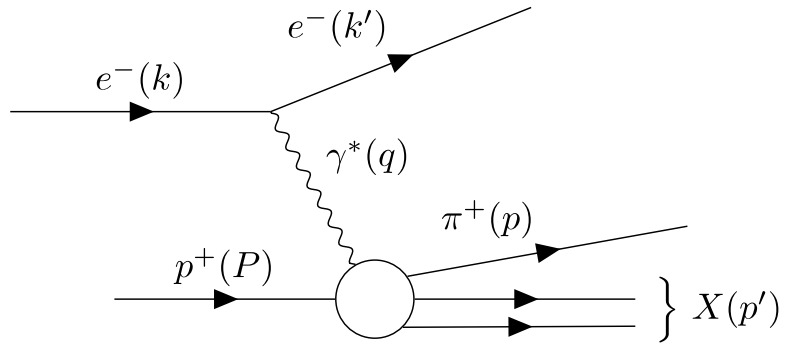

Figure 3.1: Diagram of SIDIS process with an electron scattered off a proton. The final hadronic state has a positive pion and undetected particles, labeled with an X.

obtained, considers a lepton interacting with an hadron, specifically a proton. Depending on the final state, we can define three types of processes:

- ◇ Inclusive: When only the single scattered lepton is detected.
- ◇ Semi-inclusive: When the lepton and a single final state hadron are detected. The other elements, if existing, remain undetected.
- ◇ Exclusive: When all of the final particles are detected.

Whether we decide to work in one or other group depends on the goals of the analysis. For instance, some studies on leptonic properties such as the g-2 experiment deal with the fired lepton in its initial and final states only making the *inclusive* frame adequate. On the other hand, studies on hadron production at high energy would be interested in saving as much information as possible, making the *exclusive* frame the natural selection. A middle step between these options is ideal for the study of individual hadrons like in this analysis, where the emphasis is in charged pion detection, although we still require the detection of electrons as triggers of the scattering. From now on, we will refer to our interaction of interest as Semi Inclusive Deep Inelastic Scattering (SIDIS).

We can use different systems of reference to describe the scattering and, based on the quantities under study, the selection of one or another comes in a natural way. Among others, the laboratory, center of mass and the infinite-momentum or Breit frames are the most useful in our context. For simplicity in the study, we define a general notation for the 4-momentum of each constituent of the interaction. A more specific definition relies on the frame of reference selected. The 4-momentum will always be labelled as shown in Figure 3.2.

The *Laboratory frame* (often just *lab frame*) is the most common and direct for under-

standing, since it is based on the physical distribution we get in the experiment. In this context, the initial lepton is assumed to go in the positive z direction with negligible mass in the case of an electron. The nucleon is considered at rest so that its 4-momentum has one element only, the temporal coordinate, relative to its invariant mass. The scattered lepton also receives a convenient form that could be directly extracted from the detector output.

The *Center of mass frame* (CM) is convenient for simplification of some expressions. This inertial frame is defined such that the initial state has a null total 3-momentum. When only two elements are present at the end, they are produced back-to-back.

The *Infinite-Momentum frame* (IMF) is a theoretical system in which the target nucleon is moving at a very high speed along the direction of the incoming lepton. In this frame, the target nucleon can be considered to be highly boosted, so that the momentum transfer of the virtual photon appears to be much smaller than what it would be in the rest frame of the nucleon. A scale variable x was historically introduced to account for the fraction of the nucleon's momentum carried by one of its quark. As a result of the boost, the struck quark appears to be moving nearly parallel to the direction of the incoming lepton, and its momentum can be approximated by its longitudinal momentum fraction only.

Sometimes we will talk about the *Gamma-Nucleon frame* (γN), which is related to the previous frame but not the same. This frame takes the virtual photon and the nucleon collinear, with zero transverse momentum too. Both elements have opposite momentum, so this model could be thought as a sort of CM frame between them. The nucleon presents a finite velocity that, in the limit of infinite momentum, comes back to the IMF. In this system of reference some kinematic variables get a simpler form, easier to extract from data at analysis time.

We can separate the kinematic variables observed in a SIDIS process in two groups related to the particle they are associated with. First, we get the leptonic variables, related to the upper half of the diagram of Figure 3.1. Listed below, a brief description of their interpretation and, in color, their usual representation in the lab frame are given.

- Q^2: Known in some texts as virtuality. It is an *invariant* quantity associated with the virtual photon 4-momentum. In our notation, $q = k - k'$. Since virtual photons

are off mass shell their invariant mass is not zero. Its value is negative and, for simplicity, we work with a positive version of it.

$$Q^2 = -q^2 = 4EE' \sin^2(\frac{\theta}{2}) \tag{3.6}$$

◇ ν: It's an invariant quantity by construction. However, its common interpretation as the virtual photon energy is true only in specific frames. We can apply this interpretation in the lab frame.

$$\nu = \frac{p \cdot q}{M} = E' - E \tag{3.7}$$

◇ x_b: Named X Bjorken, is an invariant that is not independent of the other leptonic variables. In the Breit frame it gets its usual interpretation as the fraction of momentum given to the struck quark in the partonic model (more on this later).

$$x_b = \frac{Q^2}{2p \cdot q} = \frac{Q^2}{2M\nu} \tag{3.8}$$

◇ y_b: Invariant quantity similar to the x Bjorken. In the laboratory frame it gives the fraction of the energy that is given to the virtual photon.

$$y_b = \frac{p \cdot q}{p \cdot k} = \frac{\nu}{E_k} \tag{3.9}$$

The second group has the hadronic variables. Some of them are exclusive of the semi-inclusive regime. The information is listed as in the previous case.

◇ Z_h: The mathematical definition suggests an interpretation as the comparison between two components from the struck nucleus, the numerator given to the final hadron and the denominator from the virtual photon. The laboratory frame provides a direct interpretation: it quantifies how much energy the hadron got from the virtual photon.

$$Z_h = \frac{p \cdot p_h}{p \cdot q} = \frac{E_h}{\nu} \tag{3.10}$$

◇ P_t^2: The transverse component of the hadron's momentum (squared) with respect to the virtual photon direction (in the γN frame). Since it is orthogonal to the

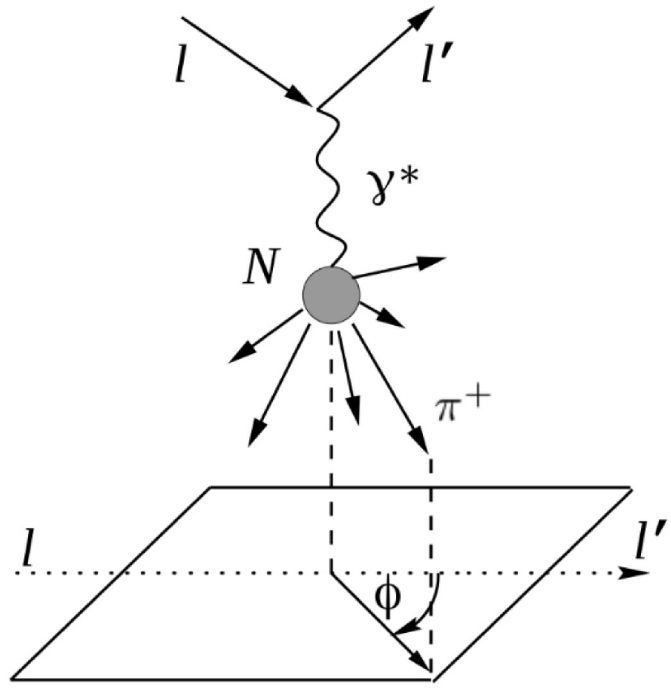

Figure 3.2: Depiction of the γN frame with z pointing down in the direction of the virtual photon. The hadronic variable ϕ_{PQ} is defined as the angle created between the detected hadron and the scattered lepton. Taken and modified from [5].

Lorentz boost directions, it's an invariant quantity. A usual approximation relates it with the expected quark transverse momentum in the same frame, by following

$$\left\langle P_t^2 \right\rangle \approx Z_h^2 \left\langle k_t^2 \right\rangle + \left\langle p_\perp^2 \right\rangle , \tag{3.11}$$

where k_t is the transverse component of the quark momentum with respect to the virtual photon and $p_\perp$ is the transverse component of the hadron with respect to the quark direction.

- ϕ_{PQ}: Azimuthal angle produced between the hadron's direction and the scattered lepton's plane. It's defined in the γN frame, with the standard positive z axis given by the virtual photon's direction of propagation. See Figure 3.2 for a depiction of the definition.
- W^2: It is the invariant mass of the whole resulting hadronic state after interaction. In elastic processes is equal to the target mass but it is larger in DIS.

$$W^2 = (p+q)^2 = M^2 - Q^2 + 2M\nu. \tag{3.12}$$

In general each particle needs four parameters to be fully characterized. Since on-shell particles have a fixed mass this number is reduced by one, leaving a total of three per final state particle. A SIDIS process is interested in two particles only, a lepton and a hadron (an electron and a charged pion in this study), which leaves six parameters to be

determined. In addition to this, unpolarized SIDIS processes have an angular symmetry associated with the scattered lepton that can be treated as a free parameter. Without loss of generality, this parameter can be fixed so that the lepton is described by only two parameters and the hadron by three. Every hadronization process of these characteristics can be completely understood knowing these five values. It is customary to choose Q^2 and ν or x_b as leptonic variables and Z_h, P_t^2, and ϕ_{PQ} as hadronic ones. Chapter 7 has the final selection of variables for this study as well as the binning selection.

3.4 Full SIDIS cross section

Further improvements to the cross section of Equation 3.5 could be added. Higher order corrections with quark and gluon loops, polarized particles, and more refined considerations are not included yet. This is not an easy task, though, because their implementation would require more sophisticated techniques. We begin by presenting a naive but effective idea, the *parton model*.

The parton model was developed by R. Feynman and is an intuitive model for understanding the internal interactions that lead to hadronization. The idea is a semi classical approach that assumes that nucleons are composed of fundamental entities collectively called *partons*. These elements follow the rules and properties of QCD mentioned in Section 3.2. For obvious reasons this is not the whole story and the approach might seem very limited. While its introduction could be regarded as a toy model, impressive results were obtained within this framework. For instance, we can obtain a term that is a crude version of the first gluon corrections associated to the Cahn effect (introduced later in this chapter). Partons are generally defined in the *infinite-momentum frame*, where the fraction of the momentum carried by the parton is x, later demonstrated to be the same as the x_b defined in SIDIS. This last discovery helped in recognizing partons as quarks and gluons.

Asymptotic freedom allows us to identify the individual components of the nuclei when they are at low energies. Customarily, $Q^2 > 1\,\mathrm{GeV}$ is the energy limit for a virtual photon in DIS to resolve the inner structure of nucleons. Since a point-like component

is not too realistic due to QM, we extend the idea of quarks to be distributed inside the nucleon, with a distinctive function called *Parton Distribution Function* (PDF).

The full set of mechanisms by which hadronization works at a fundamental level is not fully understood. Under certain requirements, we can apply what is known as the *factorization theorem*. This theoretical tool consists of a factorization of the SIDIS cross section into a product of a hard scattering coefficient, accessible using pQCD, and a soft partonic structure function, that describes the probability of finding a quark or gluon with a certain momentum fraction inside the nucleon (this is related to the PDFs). Among the conditions needed, the momentum transfer, associated with the virtual photon momentum, should be large enough to permit a reliable pQCD estimation and final state interactions should be weak to avoid a complicated description. Having that done, we can factorize both hard and soft components and separate the soft part in its contributions from the PDFs and a probability of decay called Fragmentation Function (FF) [6].

$$F(Q^2, x, Z_h) = \sum_i H_i(Q^2) f_i^N(x, Q^2) D_{i\to h}(Z_h, Q^2), \tag{3.13}$$

where the sum i is over all quark flavors, H_i is the hard part (usually written explicitly), f_i^N is the PDF for the parton i in the nucleon N, and $D_{i\to h}$ is the FF, which describes the probability of a parton i fragmenting into a hadron h.

One might wonder why there is a lack of P_t dependency in Equation 3.13. This is because it's customary to get the general expression with the momentum already integrated to avoid extra model dependencies. The formula may get this dependency back by noting that [7]:

$$F(Q^2, x, Z_h) = \int d^2\mathbf{P}_t \, F(Q^2, x, Z_h, P_t^2) \tag{3.14}$$

$$\propto \sum_i \int d^2\mathbf{k}_t d^2\mathbf{p}_\perp \delta^{(2)}(\mathbf{P}_t - Z_h\mathbf{k}_t - \mathbf{p}_\perp) f_i^N(x, k_t) D_{i\to h}(Z_h, p_\perp), \tag{3.15}$$

where the Q^2 dependency at the end has been omitted for ease of reading.

A redefinition of the structure function with the explicit P_t^2 dependence needs some assumptions. Introducing *Transverse Momentum Dependent* (TMD) functions as a factor that is added to the PDFs and FFs in order to include the momentum dependency. This separation requires an ansatz for the function to be meaningful, though. The usual se-

lection is a Gaussian spread with the internal quark transverse momentum k_t and the pure hadron contribution p_t associated with the PDF and the FF, respectively. A general implementation of this expansion is shown in Equation 3.15, and the usual ansatz can be found in Equations [13] and [33] of [7]. Both contributions could be mixed into a single function that uses the approximation of Equation 3.11 as characteristic parameter (the distribution's standard deviation).

These momentum considerations will help in giving a more detailed form of the distributions. The spin of the inner components of the nucleon also play a role that can't be dismissed and could be accounted for by TMDs. As part of the jargon, we define the term *twist* as the size of a contribution that has come from a P_t and spin expansions. Those sizes are usually expressed as powers of $1/Q$, but depending on the momentum regime the definition gets slightly loose. For instance, at low momentum a n-twist contribution is a term that goes as a power of $1/Q^{n-2}$, which is not the same as the one defined at high momentum [8]. These discrepancies are not of interest for us and from now on we will refer to twist as in the low momentum definition. Some theoretical work has been developed for accounting the use of the twist terminology in nuclear media. The expression's expansion is still reliable, though differences in the order of magnitude of higher twist contributions are visible. Multiple parton scattering is regarded as a possible source of this enhancement with increasing nuclear size [9].

The soft elements (PDFs and FFs) are expected to be unique for each nucleon, so factorization gives us a mechanism for acquiring sub nuclear information. Experiments with a simple environment are used to extract the functions associated and characterize the medium. These values are fully experimental and would be used as input for more complicated studies.

We stress that the use of TMD factorization is limited. One way of getting more confident about whether TMD is reliable or not is to check the region of production of the hadron. Three regions can be found, defined in [10]:

- Current Fragmentation Region (CFR): The hadron is produced from a quark that interacted with the virtual photon. This is the framework where TMD is suitable to correctly describe the PDFs and FFs.

- ◇ Target Fragmentation Region (TFR): The hadron is produced by a quark from the nucleus. Factorization could be used but the process is dominated by *Fracture Functions* that are not widely studied.
- ◇ Central (or Soft) Fragmentation Region (SFR): The hadron is produced by an intermediate process, this is, by higher order events such as gluon interaction or secondary internal events. Some sort of middle-step factorization might be used, but no precise information is known.

The CFR region has received the most theoretical attention and would be the ideal starting point for an attempt to extract the full structure functions. Depending on the energies available for an experiment, the regions may be more or less separated, so overlaps of the two former regions are likely. Though highly dependent on the energies of our experiment, a rough cut of regions could be done by analysing the rapidity of the hadron. A study related to this topic will be carried out in Section 8.3.2.

The non-existence of a complete model for the internal hadrons' creation process makes it challenging to simulate them. One of the most known models is the so called *Lund string model*. At short distances the potential of the strong interaction follows a Coulomb-like form, while at high distances it is found to increase linearly. In this last scenario, the model adds color tubes (or strings) that join the partons and get stretched [11]. At sufficiently high distance, the tubes get so thin that they get cut and a pair of partons with zero net color is created. With this simple idea, event generators such as Pythia have reproduced the hadronization process with successful results [12], even predicting reactions such as particle jets formation at high energy collisions.

With all definitions given above, we can get an idea of the process of derivation of a full formula for the unpolarized cross section. The development can be closely followed in [13]. The most general cross section formula that includes the polarization contributions of target, lepton, and virtual photon consists of 18 terms. Although more complete than our previous estimations, this is still just an approximation at twist-2 and twist-3, the usual higher level of interest.

$$
\begin{aligned}
\frac{d^6\sigma}{dxdydzd\phi_S d\phi_h dP_t^2} = \frac{\alpha^2}{xQ^2}\frac{y}{2(1-\epsilon)} \\
\times \Big\{ F_{UU,T} + \epsilon F_{UU,L} + \sqrt{2\epsilon(1+\epsilon)}\cos\phi_h F_{UU}^{\cos\phi_h} + \epsilon\cos(2\phi_h) F_{UU}^{\cos 2\phi_h} \\
+ \lambda_e\sqrt{2\epsilon(1-\epsilon)}\sin\phi_h F_{LU}^{\sin\phi_h} \\
+ S_\parallel\left[\sqrt{2\epsilon(1+\epsilon)}\sin\phi_h F_{UL}^{\sin\phi_h} + \epsilon\sin(2\phi_h) F_{UL}^{\sin 2\phi_h}\right] \\
+ S_\parallel\lambda_e\left[\sqrt{1-\epsilon^2}F_{LL} + \sqrt{2\epsilon(1-\epsilon)}\cos\phi_h F_{LL}^{\cos\phi_h}\right] \\
+ |\mathbf{S}_\perp|\Big[\sin\left(\phi_h-\phi_S\right)\left(F_{UT,T}^{\sin(\phi_h-\phi_S)} + \epsilon F_{UT,L}^{\sin(\phi_h-\phi_S)}\right) \\
+ \epsilon\sin\left(\phi_h+\phi_S\right) F_{UT}^{\sin(\phi_h+\phi_S)} + \epsilon\sin\left(3\phi_h-\phi_S\right) F_{UT}^{\sin(3\phi_h-\phi_S)} \\
+ \sqrt{2\epsilon(1+\epsilon)}\sin\phi_S F_{UT}^{\sin\phi_S} + \sqrt{2\epsilon(1+\epsilon)}\sin\left(2\phi_h-\phi_S\right) F_{UT}^{\sin(2\phi_h-\phi_S)}\Big] \\
+ |\mathbf{S}_\perp|\lambda_e\Big[\sqrt{1-\epsilon^2}\cos\left(\phi_h-\phi_S\right) F_{LT}^{\cos(\phi_h-\phi_S)} + \sqrt{2\epsilon(1-\epsilon)}\cos\phi_S F_{LT}^{\cos\phi_S} \\
+ \sqrt{2\epsilon(1-\epsilon)}\cos\left(2\phi_h-\phi_S\right) F_{LT}^{\cos(2\phi_h-\phi_S)}\Big]\Big\}, \quad (3.16)
\end{aligned}
$$

where $(x, y, z, \phi_h, P_t^2) \equiv (x_b, y_b, Z_h, \phi_{PQ}, P_t^2)$ in our notation, ϕ_S is the angle formed by the target's spin vector $\mathbf{S}$ with respect to the leptonic plane, ϵ is the ratio of longitudinal and transverse photon flux, and λ_e is related to the longitudinal polarization of the incoming lepton ($\lambda_e = 1$ corresponds to a purely right-handed beam). The structure functions $F_{ij,k}^l$ gets the information of the polarization of the beam i, the target j, and the virtual photon k when needed, taking values L for longitudinal, T for transverse, and U for unpolarized; l shows explicitly the ϕ_{PQ} function associated to the term.

We won't focus on all of the terms, but we will discuss a bit about the first lines of Equation 3.16. The first two terms, independent of ϕ_{PQ}, are different due to the polarization of the virtual photon. Free photons would contribute only to the first term, so the longitudinal component is attributed to the off-shell state.

The next term ($\propto \cos\phi_{PQ}$) is formally known to be composed of at least two terms at twist-2 and twist-3. These are known as *Cahn* and *Boer-Mulders* terms, respectively. The former could be obtained in different ways, the simpler is by adding the intrinsic momentum of the quark inside the nucleon (similar to the so-called Fermi motion) as a Gaussian TMD function. At first order we will find a term that is an approximation of the

twist-2 form obtained in a more worked out way (see Equations (32-38) in [14]). The latter term is a bit more intricate, since it arises from the coupling of the internal spin of the quarks with the whole target. There might exist a net polarization that is perpendicular to the whole-nucleon and quark directions, even though the overall distribution has null polarization [15]. An effect is produced over the final hadron, accompanying the $\cos\phi_{PQ}$ at twist-3 level. Moreover, a new contribution at twist-2 proportional to $\cos(2\phi_{PQ})$ is found. This later is of special interest since a non-null contribution would be likely a confirmation of the Boer-Mulders description [16].

The remaining terms are not of interest for us from now, since we will care about unpolarized components only. The final form of the formula for cross section will be a simplification for unpolarized targets and beam [8] that reduces the cumbersome representation given. Note that there is a change in the kinematic variables to match the experimental selection[2]. We will work with:

$$\frac{d^5\sigma}{dQ^2 d\nu dZ_h dP_t^2 d\phi_{PQ}} \equiv A + B\cos(\phi_{PQ}) + C\cos(2\phi_{PQ}), \tag{3.17}$$

where all four variables apart from ϕ_{PQ} are implicit in the factors A, B, and C.

[2]The ν dependency might be changed to x_b depending on the study. We will discuss this selection in Chapter 7.

Chapter 4

Experimental setup

The energy a particle accelerator can reach defines the physics that could be studied with it. Different ways of tuning these values exist, however. This fact leads to the appearance of several configurations for accelerators in order to better fit the physics requirements of a specific process under study.

Among others, the accelerator's geometry is one of the principal visual differences. We find linear and circular accelerators as the main geometries in laboratories around the world. The former is usually presented as a straight tunnel, being the most common, but space-optimized configurations also exist and will be discussed in this chapter. As an example of a linear accelerator (LINAC) we find the **S**tanford **L**inear **Ac**celerator (SLAC) in California, USA. On the other hand, the **L**arge **H**adron **C**ollider (LHC), at CERN, is one of the most known circular accelerators.

Both configurations present their own advantages and disadvantages. Firstly, the shape of a LINAC restricts the study to stationary target experiments mainly, while circular ones can be used for collision experiments as well as fixed target. This distinction also affects the energy regime since, at center of mass level, the energies obtained in a collider are doubled with respect to LINACs and the space required to produce the same energy beam is significantly lower in circular accelerators. On the other hand, a circular machine can't avoid the production of synchrotron radiation, which affects light particles the most. This last point explains why LINACs are desirable for electron experiments, while circular ones work with heavier particles such as protons. One last remark is the interaction length, that for fixed target experiments rely mainly on the target thickness

and, for beam collisions, depend on the bunch frequency (a higher rate will produce more interactions).

Despite these differences, every accelerator is composed of the same fundamental elements and needs a group of specialized detection devices to correctly identify a particle track. A description of the accelerator facility used for the experiment and its components is developed in this chapter.

4.1 The accelerator CEBAF

The **C**ontinuous **E**lectron **B**eam **A**ccelerator **F**acility (CEBAF) is a linear electron accelerator and the main facility at the Thomas Jefferson National Accelerator Facility (also known as Jefferson Lab or simply JLab) in Newport News, Virginia, USA. This accelerator has been used continuously since its first run in 1995, and has received some upgrades along its life, beginning with a maximum beam energy of $4\,\mathrm{GeV}$ up to the current $12\,\mathrm{GeV}$ that has been recently implemented. Despite its 'racetrack' shape (see Figure 4.1), the accelerator is considered a linear one, bent up to five times per side (ten curves in total) which makes it more compact. The experiments are located in halls coupled to the ends of the linear portions, where the structure begins to bend. There are four experimental areas, three of them since the beginning of the laboratory functions labelled from *A* to *C* in one side and the newest one, Hall *D*, inaugurated in the $12\,\mathrm{GeV}$ era, located in the opposite side. Each of them gathers different research groups developing diverse nuclear physics analyses of topics such as hadron spectroscopy or production and decay of light mesons, with detectors specialized for these purposes in their respective hall. In this work, we will focus on the Hall B specifications.

The CEBAF generates an initial electron beam with a frequency of $1.4971\,\mathrm{GHz}$, matching the frequency used in the accelerator magnets. The beam is said to be continuous, but in detail it is composed of electron bunches of $2\,\mathrm{ps}$ length separated by intervals of around $2\,\mathrm{ns}$. This could produce beams with a luminosity of around $10^{38}\,\mathrm{cm}^{-2}\mathrm{s}^{-1}$ at the time of performance of our experiment. However, this quantity is split in the different halls and limited by the maximum detection rate of each individual detector. This provided a maximum luminosity of $2 \times 10^{34}\,\mathrm{cm}^{-2}\mathrm{s}^{-1}$ in Hall B.

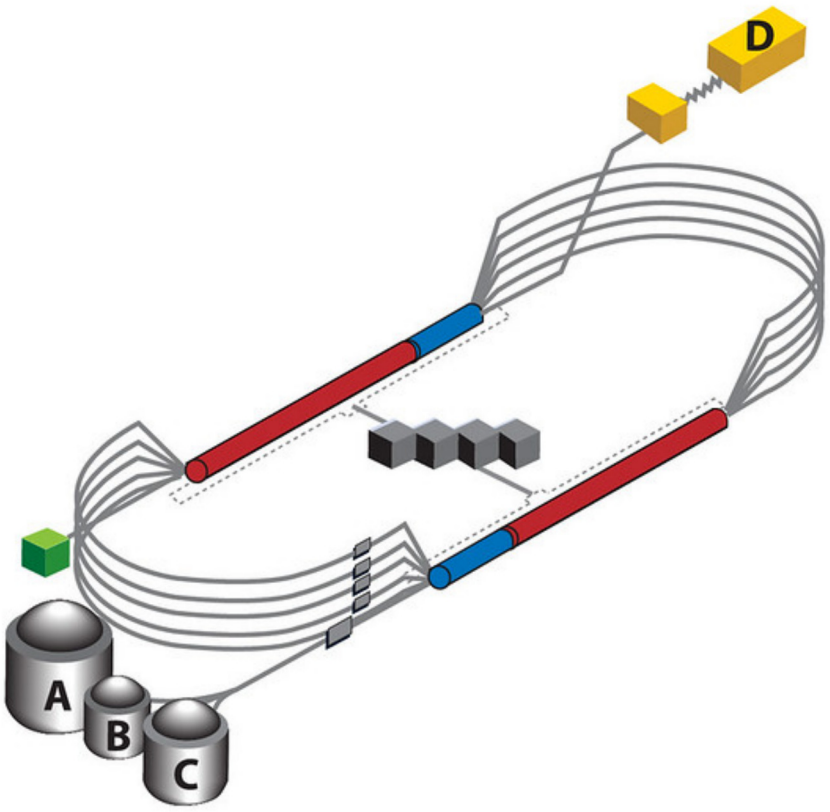

Figure 4.1: Depiction of CEBAF facilities with the new 12 GeV upgrade.

Certain experiments required the use of a polarized electron beam also. The CEBAF was designed to accomplish this requirement, with the capability to supply highly polarized as well as non-polarized beams.

4.2 The CLAS detector

The **C**EBAF **L**arge **A**cceptance **S**pectrometer (CLAS) detector is a fixed target particle-detector installed in the Hall B and the main interest of this thesis. It is compounded of several layers in an onion-like distribution. The structure can be separated in three main regions, going from inside to the outer layers, and in six sectors around the forward beam axis. From now on, in the laboratory system of reference, we define the z axis as going along the beam line, setting the zero in the center of the nutshell-like structure and going positive downstream the beam. The other two axes are defined as seen in Figure 4.3, with y pointing up to the ceiling and x according to the right-hand rule. It is important to recall the convention used for the spherical system of coordinates, where θ is defined as the angle that moves down from the positive z direction, and ϕ goes from 0° in the positive x direction, increasing positive towards the positive y direction. The

detector was built with a high angular acceptance in mind, covering a polar range of: $8^\circ < \theta < 142^\circ$ and full azimuthal range ($0^\circ < \phi < 360^\circ$), which makes a total angular covering of around 3π steradians.

Given the actual arrangement of components of the detector, we can separate them by their distribution along the polar direction in two sets. Firstly, we get the *Forward region*, where the predominant interest is in charged particles. A group of detectors are placed in order to tag them and are specialized in differentiate energetic particles such as negative pions from electrons, for instance. Secondly, a *Large-angle region* is implemented for high transverse momentum particles. It is composed of a smaller number of layers because we expect less energetic particles to reach here. This region is not a central part of the study and the emphasis will be on the former.

The whole structure of the detector and the distribution of its components was constructed based on the magnetic field generated inside. The main objective of the magnetic field is to deflect charged particles towards or away of the forward region of the detector depending on the charge polarity. Two magnets are installed at different radial distance inside the shell. The inner magnet is a *mini-torus* composed of six coils regularly distributed around the beam axis about $1\,\mathrm{m}$ away of the beam. This one is of great interest in studies of lepton-inclusive scattering and fundamental for removing contamination from Møller electrons. The larger magnet, known as the *main torus*, is also a six coil array with the same azimuthal distribution, but around $2 - 3\,\mathrm{m}$ away from the center[1]. This number of coils, though apparently small, can generate a non-homogeneous magnetic field sufficiently strong, with a maximum magnitude of integral magnetic field of $2.5\,\mathrm{T}\cdot\mathrm{m}$ when working with the highest current available of $3860\,\mathrm{A}$.

The magnets were designed so that the field's orientation is predominantly azimuthal. This would produce a deviation of the charged particles' trajectory in the polar direction, leaving the ϕ coordinate constant in an ideal scenario. For practical reasons, there is always another component of the field close to the coils, but it is expected to be negligible in a great part of the active area and ϕ should not change too dramatically. It's important to take care of the sections where this claim is not true, however. Large inhomogeneities

[1]The coils of the main torus have a diameter of $1\,\mathrm{m}$ approximately, so the shortest distance presented is with respect to the nearest side of the coil.

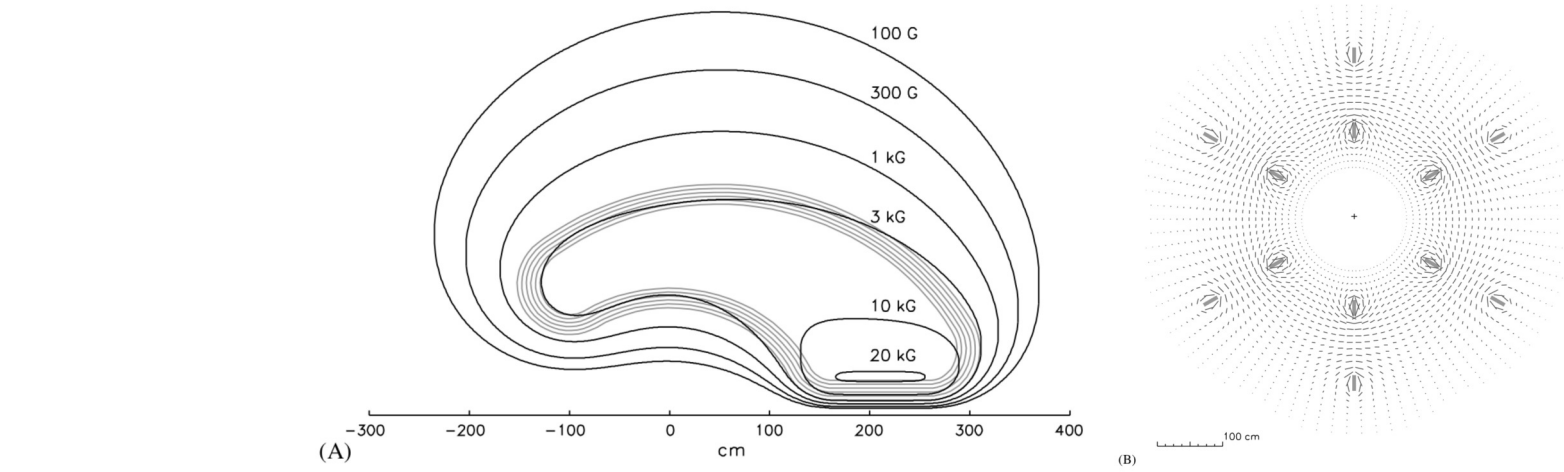

Figure 4.2: Magnetic field distribution: Slide in yz plane with field's magnitude represented as level curves (left) and xy plane transversal to the beam line with field's magnitude represented by the lines' length (right). Taken from [17].

are observed in the surrounding spaces around the coils as shown in Figure 4.2. This presents a significant constraint for the rest of the structure. To avoid this effect, the detector's layers are built in modules distributed in six sectors covering nearly $60°$ each in the azimuthal direction. The sides where these structures meet have a low efficiency and unmanageable border effects that are not desired and would be dropped from the analysis. Getting them aligned with the coils reduces the dead zones and maximizes the active area performance.

The CLAS structure was not constructed with a specific experiment in mind, so it should be flexible enough to work with diverse configurations. The shape of the system makes it easy to change between targets and add extra detectors if the study requires it. Certain experiments may require the use of polarized targets that could be easily affected by electromagnetic fields. This imposes the necessity of a field-free environment in the center of the detector, where the targets would be located.

4.3 Components of the detector

The detector is sensitive to charged particles with $p \geq 0.2\,\mathrm{GeV}$ and photons of energy $E_\gamma \geq 0.1\,\mathrm{GeV}$. The overall resolutions are presented in Table 4.1. These values are obtained after merging the contributions of all the layers.

A description of the different layers, the detectors implemented, and the purpose of each of them will be presented. More specifications can be found in [17].

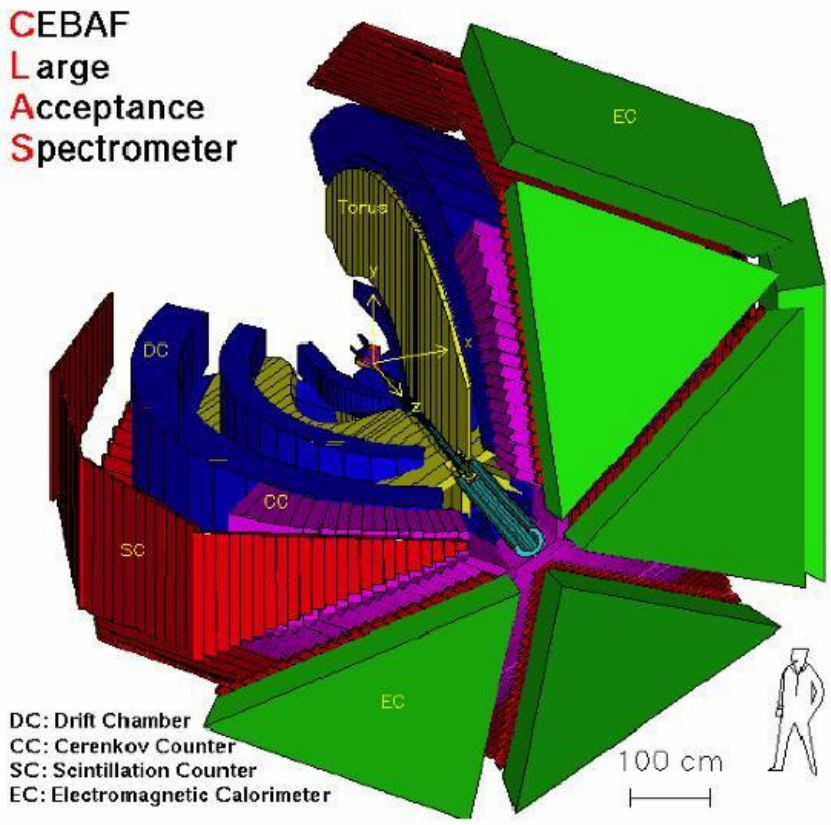

Figure 4.3: Depiction of the CLAS detector, its components, and scale reference. The detector's layers are presented in different colors: Drift Chambers (DC - blue), Cherenkov Counters (CC - violet), Time Of Flight (TOF or SC - red), Electromagnetic Calorimeter (ECAL - green), and Main Torus (Torus - yellow).

Table 4.1: Overall resolutions of the detector. The difference in the θ domain comes from the different sensors used in the Forward region and at higher polar angles.

	Resolution
Momentum ($\theta \lesssim 30°$)	$\sigma_p/p \approx 0.5\%$
Momentum ($\theta \gtrsim 30°$)	$\sigma_p/p \approx (1-2)\%$
Polar angle	$\sigma_\theta \approx 1\,\mathrm{mrad}$
Azimuthal angle	$\sigma_\phi \approx 4\,\mathrm{mrad}$
Time (charged particles)	$\sigma_t \approx (100-250)\,\mathrm{ps}$
Photon energy	$\sigma_E/E \approx 10\%/\sqrt{E}$

4.3.1 Drift Chamber

The first line of detection is composed of Drift Chambers (DC) in a three-layer structure. The inner and outermost are positioned in a low magnetic field region while the second one, in the middle, is in between a couple of magnetic coils thus embedded in a high magnetic field region. Each of these big-layers is known as a *region*. All three regions spans over a polar range: $8° < \theta < 142°$, and they are separated in six azimuthal sectors each leaving a total of 18 individual DCs. A single DC is composed of two super-layers

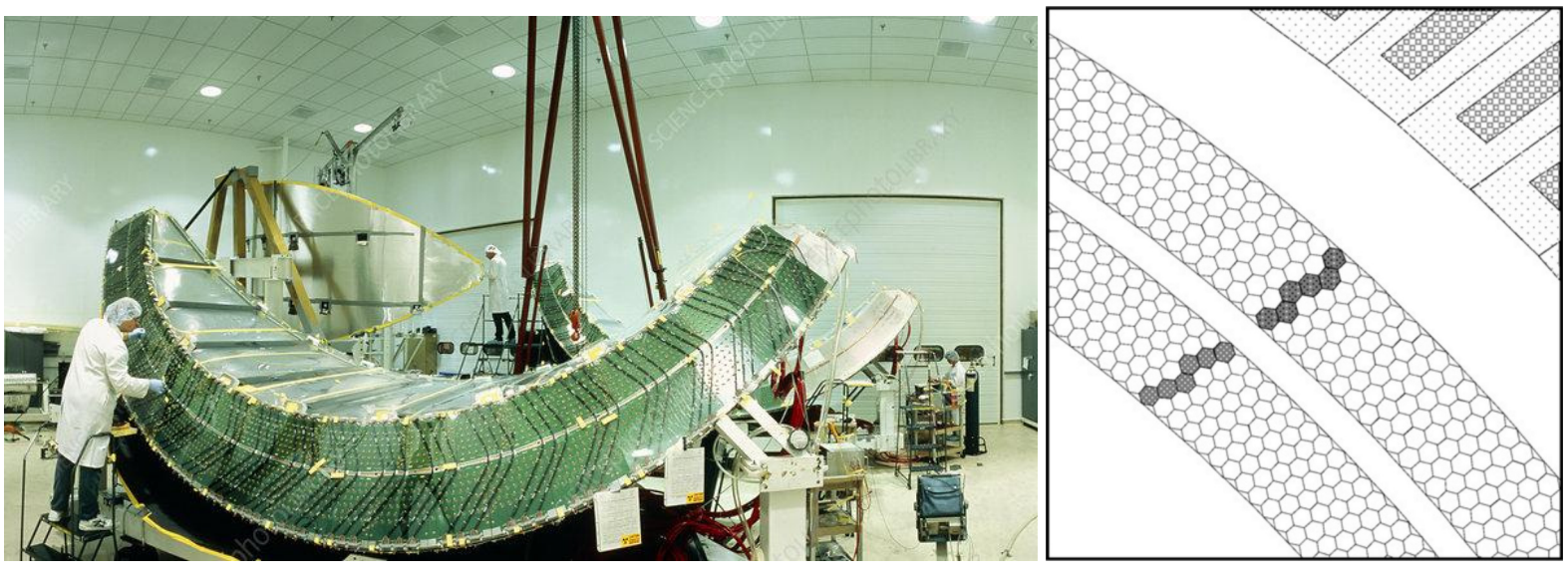

Figure 4.4: Photograph of one of the DC installed at Jefferson Lab (left). Depiction of the track left by a particle in two super-layers of the outermost region of DC (right). Credits of the photo to: David Parker / Science Photo Library.

that are a collection of six layers each[2] of hexagonal wire cells. One of the super-layers is placed over the other with a $6°$ tilt perpendicular to the radial direction to improve track determination. The chambers are all filled with a high purity gas mixture that enhances the drift velocity of the interacting electrons to improve tracking and momentum resolution.

The inner structure of a DC is composed of several wires separated into groups of seven, arranged in an hexagonal formation plus one at the center. The wires at the vertices are called *field wires* and are set at a negative potential. The central one is named *sense wire* and is set at a high positive voltage. The voltages are selected such that a charged particle can ionize the gas through its path in the chamber and an avalanche effect will create a signal in the sense wire, where electrons are naturally attracted due to the electric fields. The voltages and gas composition are tuned to give a reasonable recovery time between interactions, improving the rate of response and thus increasing the number of tracks detected.

It could be deduced from the last paragraph that a DC reacts only with ionizing particles. Its main focus is on the detection of charged particles. After a particle leaves its track in the detector, the signals generated can be correlated using specialized algorithms of reconstruction. Because the second region is exposed to high magnetic fields, the charged

[2]The only exception is the inner region with four layers instead, due to space limitation.

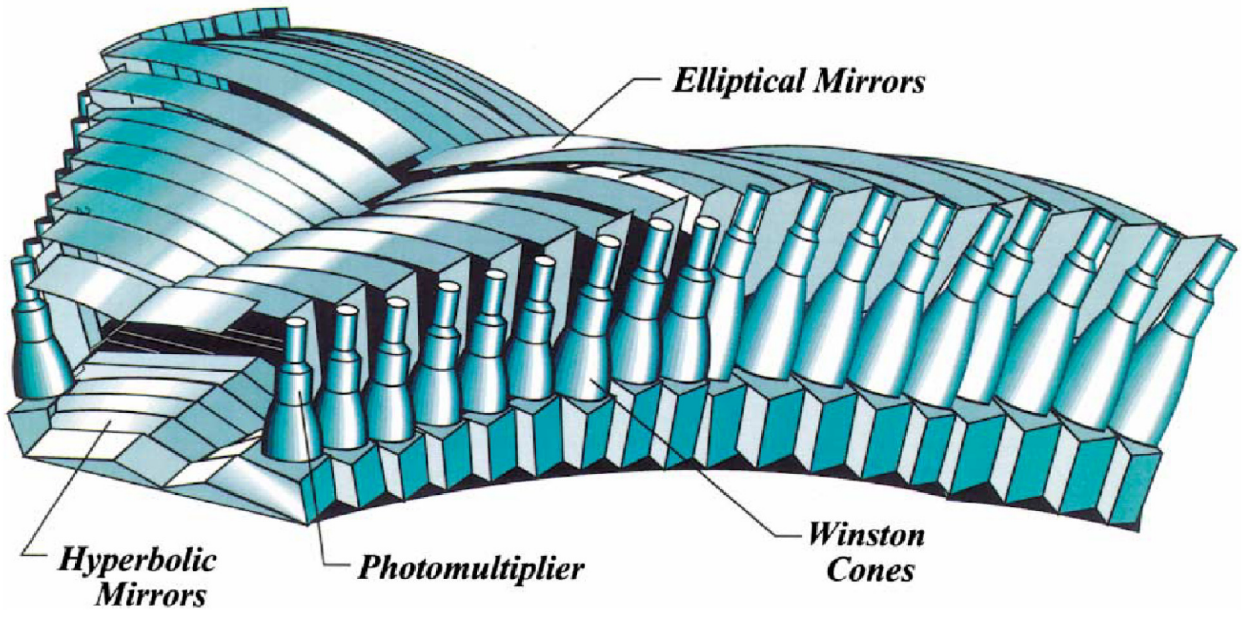

Figure 4.5: Cherenkov Counter.

particles will be highly deflected and its momentum can be easily found by the use of Lorentz's law over the curvature of the track.

4.3.2 Cherenkov Counter

In the forward region of the detector, behind the DCs, we find the Cherenkov Counters (CC). They are mirror-like structures with a geometry carefully design to focus the radiated photons into a photo multiplier tube (PMT). The whole array of CCs covers a polar range that goes from a few degrees up to $\theta < 45°$, and it follows the same azimuthal structure of sectors seen. To improve the polar resolution, eighteen (18) pairs of CCs are placed along the polar domain in each sector. The pairs are a mirror image of each other, joining in the middle of each sector (see Figure 4.5). This leaves a total of 216 individual CC.

The principle of operation of a CC is based on the well known Cherenkov effect that occurs when a charged particle passes through a dielectric medium at a velocity higher than the light's velocity in that medium. When this happens, the electromagnetic radiation emitted by the particle generates a wave front with a characteristic angle that is a function of the refractive index of the medium and the particle's velocity. This velocity can be found indirectly by measuring the signal recorded by the PMTs.

In order to get an optimum efficiency, the PMTs are placed behind the magnetic coils. This takes advantage of the dead zones with low efficiency in the vertices of the hexagon

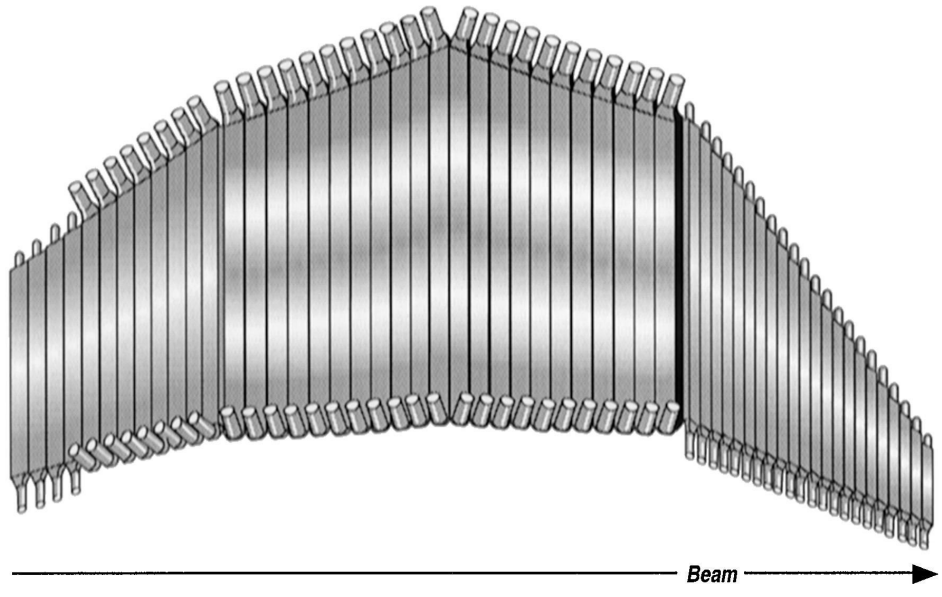

Figure 4.6: Time Of Flight system presented with the beam direction at the bottom. Note the different angles of the layers, specially at forward direction.

created by the six sectors, where the particles are hardly detected. The effects the magnetic fields could produce on the PMTs are significantly reduced by the use of special cases known as magnetic shields.

The CCs are of great importance in the detection of electrons because we can easily discriminate between them and other negative particles such as negative pions. This is possible due to the difference in the energy required by the particles to begin radiating in the chambers. For instance, electrons start to emit Cherenkov radiation when getting energies of $0.9\,\mathrm{GeV}$ in contrast to negative pions that begin around $2.5\,\mathrm{GeV}$. This restricts the range of application of this detector to the forward region, where the more energetic particles are, but presents a clever way of easily differentiating between similar particles. Because of the clear determination of electrons we use this detector as a trigger for events.

4.3.3 Time Of Flight

The Time Of Flight (TOF) detectors are placed after the CC in the forward region ($\theta < 45°$) and behind the DCs in the large-angle region ($45° < \theta < 142°$), fully covering the azimuthal direction.

The TOF system is composed of several rods made of a scintillating material with a PMT in both ends, joined in arrays forming planes. One of these planes covers the forward region and three are in the remaining polar zones. These layers are placed one per sector

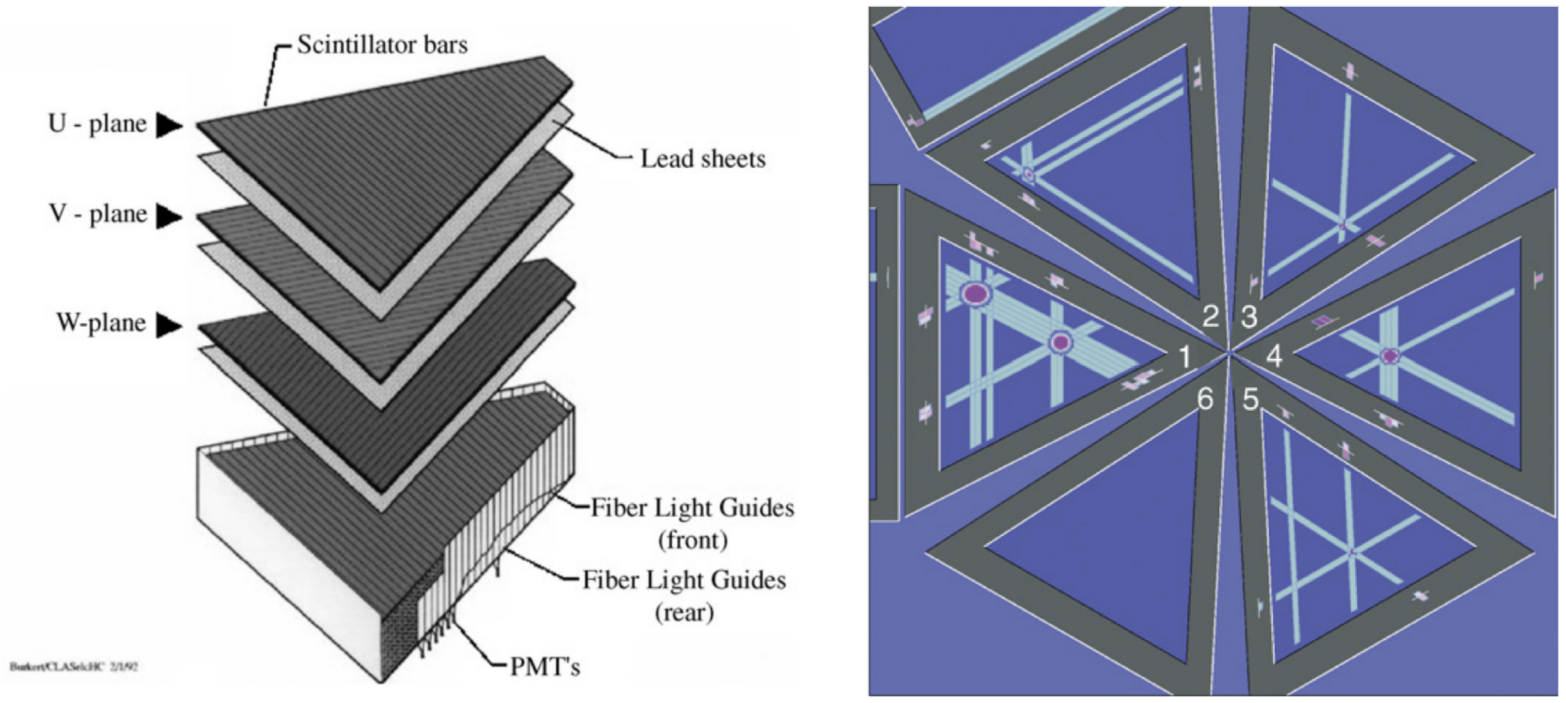

Figure 4.7: Electromagnetic Calorimeter: layers detail (left) and example of triangulation of track reconstruction (right).

and positioned perpendicular to the average particle direction in each section (as seen in Figure 4.6). They interact with ionizing particles, generating a light signal amplified by the PMTs that is used as a timestamp for the track. Its velocity is easily found as long as we have a good estimation of the total track length.

The dimensions of the rods are variable, depending on their position. Since the planes have a triangular shape in the forward region, the length of these bars vary between 32 and $376\,\mathrm{cm}$. The remaining planes, forming a barrel around the center of the detector, have a similar length to the longest one in the forward region. Every rod subtends a polar angle of around $1.5°$.

The timing resolution obtained by the counters depend on their dimensions but are in the order of the hundreds of ps (values of 60 - $120\,\mathrm{ps}$ have been found). This make time measurements very precise, improving the identification of leading-process and sub-leading-process particles. The timing discrimination has been useful to differentiate between pions and kaons, for instance.

4.3.4 Electromagnetic Calorimeter

The last layer of detectors is composed of Electromagnetic Calorimeters (ECAL), placed in the forward region behind the TOF system and spanning over a polar range similarly to the other forward detectors ($\theta < 45°$) and ranging over the whole azimuthal domain.

There is one module per sector, giving a total of six, each with 39 layers of scintillators and lead stacked in a sandwich-like composition. The layers have a triangular structure, almost equilateral, with a cut in the portion that is nearer to the beam line (low θ). The total thickness of the detector is 16 radiation lengths. The layers are made of two materials: $10\,\mathrm{mm}$ thick scintillators and $2.2\,\mathrm{mm}$ thick lead sheets.

Similarly to the TOF system, a group of parallel scintillator rods are joined to create a layer, with PMTs at each end placed behind the magnetic coils. To get a better position reconstruction each layer is rotated $120°$, parallel to one of the three sides of the triangular structure in an alternate pattern. The different orientations are labelled as U, V, and W, and the module has 13 layers of each. Sheets of different thicknesses are used, grouping the first 5 with the name of *inner layers* and the 8 remaining called *outer layers*. This distinction is useful to better reject π^- contamination and for other applications like neutron detection.

When an ionizing particle passes through the ECAL, it generates a signal in the scintillator system. Then, it will interact with the sheet of lead, radiating and reducing its energy. A dense material such as lead is required since this would produce a higher probability of interaction, improving the effectiveness of the system. A shower of particles, mainly electrons and photons, is generated after the interaction. This shower will leave several tracks in the next scintillator layer and, after this, will interact with another lead sheet. The process is repeated until the initial particle has released all its kinematic energy or exits from the back of the detector. Whatever happens first, the final energy of the particle will be lower and we can trace back its path using the scintillators' information. Moreover, the pattern of energy loss is characteristic of each particle type. This presents another method of particle identification.

The ECAL is mainly used for triggering electrons as well as the CC. Only electrons with energies above $0.5\,\mathrm{GeV}$ can be reconstructed by this detector. Neutral particles such as neutrons and photons also can be registered, with a threshold of energy of $0.2\,\mathrm{GeV}$. This is useful in the reconstruction of processes involving 2γ decays, such as for π^0 and η mesons.

4.4 The Eg2 experiment

The process of data taking was performed following the requirements and descriptions given in [18]. The main feature of this setup is the implementation of a double target system in the center of the detector.

The double target apparatus is the support structure where samples of diverse materials are located. The samples are solid disks made of *Carbon (C)*, *Iron (Fe)*, *Lead (Pb)*, Tin (Sn), or Aluminum (Al) and an extra liquid target of *Deuterium (D)*. Every solid disk has approximately $3\,\mathrm{mm}$ of diameter and a thickness chosen to be less than 3% of the radiation length of the material. A similar number of nuclei are expected for each disk, thus their different dimensions. The liquid deuterium is $2\,\mathrm{cm}$ long and is stored in a special case with refrigeration, where its properties are barely changed. Only one solid target is present at a time with the liquid target. A thin aluminum layer is placed in the middle between targets too. Both targets are located with a separation of $4\,\mathrm{cm}$, in order to minimize acceptance issues. The two targets are aligned with the beam line, deuterium first and the solid disk behind.

At running time, all of the solid targets are placed in 'metallic fingers' around the beam axis, as seen in Figure 4.8. They are remotely controlled to be positioned in the beam line one by one. To reduce second scattering processes and background sources, the rods are bent so that the unused targets are aligned with the dead zones of the detector.

This setup was proposed to make different studies of hadronization with nuclear media, using the simple deuterium medium as reference. An unpolarized beam and targets were required to simplify certain quantities such as cross sections. In practice, the beam had less than 5% of polarization. The advantage of a system with two targets is the reduction of uncertainties given by systematic effects. Whenever we are interested in quantities that depend on ratios between the two targets, luminosity factors should be introduced. However, this configuration produces a direct simplification of them, removing the source of uncertainty.

The magnetic field needs to be tuned with a polarity such that negative charged particles get in-bend deflected, this is, towards small θ values. Although this gives a higher rate

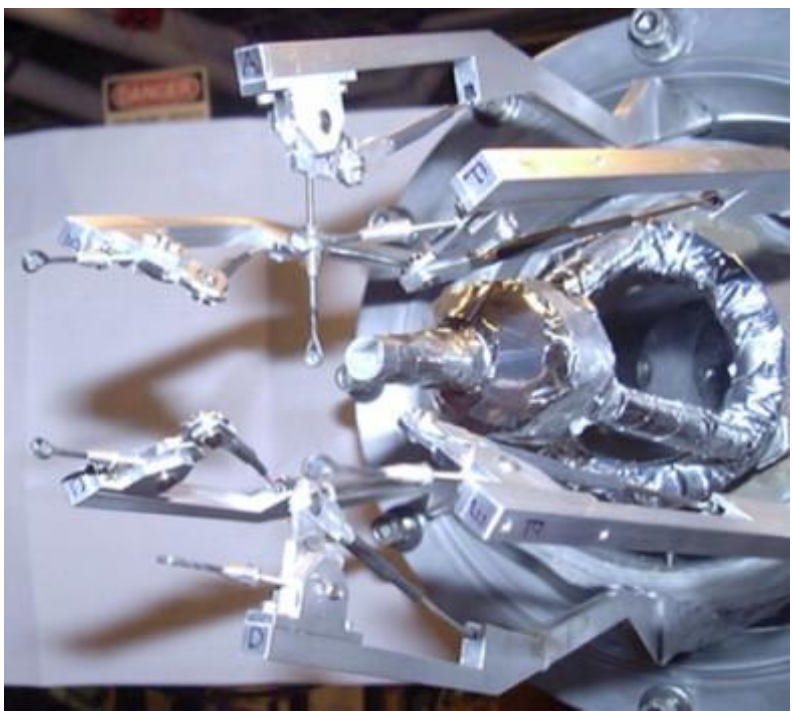

Figure 4.8: Double target support structure with deuterium target's case at the center and one of the solid targets aligned with the beam, attached to the top finger.

of electrons in the forward region, where we can detect them in a more precise way, a significant number of events is still lost if they reach low acceptance regions. This problem was solved by moving the targets from the very center of the structure to negative z values, away from the forward detectors. The final position in z of the solid and liquid targets is around $-30\,\mathrm{cm}$ and $-26\,\mathrm{cm}$, respectively.

At analysis time, a misalignment in the beam with the definition of the origin of the xy plane was found. A deep study on this was developed by T. Mineeva [19] with valuable results. This issue will be covered in Section 5.2.5.

Chapter 5

Data management

The process of data taking was performed in three separated groups of runs at different beam energies ($4.0\,\mathrm{GeV}$, $4.5\,\mathrm{GeV}$, and $5.014\,\mathrm{GeV}$) between Summer of 2003 and March of 2004. The third campaign, with the highest energy, collected the largest set of statistics. This is why we chose this set to develop our studies.

The targets tested in this run were *Carbon*, *Iron*, and *Lead*, with their respective liquid Deuterium companion upstream. The triggering and storing of data processes are performed in several steps both online and offline. A description of it is explained below.

The offline reconstruction uses the online triggers as inputs plus extra quality cuts in each component. The reconstruction used in this analysis is known as *pass2* and will be presented too. Later, a description of the selection rules for the fine Particle Identification (PID) is also shown.

5.1 Data processing

The direct interaction of the beam with the targets is expected to generate a huge number of particles. Unfortunately, this is not the unique source of them. Background could be produced from astroparticles, external sources, or unwanted interactions with the experimental structure. Moreover, all of them could create a signal in different components of detector and there is always chance for noise produced by electronics. All of this must be considered to optimize the recording of data.

Saving every single response is impossible due to limitations on the storage space. Additionally, a sophisticated online selection is not manageable because of the limited ve-

locity of processing and the rate of interactions. Also, cutting too tight on the selection of events would impact on the record of false positive and miss events.

The solution to this problem was to divide the process of data collecting in several steps. The essential information is stored as *raw* data, with a first selection based on the detector's response and its quality. Simple matches between different components are applied too in order to reduce the effect of random signals. The resulting data set should be larger than the ideal one. Nevertheless, an offline pruning process is expected to improve the quality of the final sample.

The Data Acquisition System (DAQ) is responsible for saving the events and to process them. The DAQ begins with a two level triggering system and a subsequent offline reconstruction known as *cooking*. The *Level 1 Trigger* receives as input a simultaneous signal with a certain threshold coming from the ECAL, CC, and TOF detectors. If there is a coincidence signal in more than one component inside a defined time window, the event is preliminarily accepted. For the first lepton found, this response is presumably the scattered electron. The positive signal is sent to the Read-Out-Controllers (ROCs), where a specific criteria is followed to determine if the hit is actually a real event or if it comes from another source.

The *Level 2 Trigger* is accessed only if the first level was successful. The DC information is computed to find the best candidate for a track using different reconstruction algorithms. If a positive result is obtained the event is sent to the Event Builder (EB) where the information from all of the detectors is gathered and stored in *banks*. On the other hand, a negative result would be registered and the Level 1 would be repeated searching for new triggers. After the EB action, the Event Recorder (ER) and Event Transfer (ET) processes are in charge of writing the data into the Redundant Array of Inexpensive Disks (RAIDs). The quality of the measurements is monitored and transferred later to the magnetic tape, known as *silo*. Everything saved in this structure is permanently stored. Each run creates a separate file with around 10 million events. The raw data is saved in Bank Object System (BOS) format and it is set ready to access for future manipulations.

The second half of the DAQ is performed offline in three steps. Firstly, a calibration of the signals from the detector subsystems is carried out. The information gathered by the

Analog-to-Digital Converters (ADCs) and Time-to-Digital Converters (TDCs) are used to determine the energy deposited in each component and the time of the hit, respectively. Secondly, the calibrated signals are stored again in BOS format, making use of the Simple Event Builder (SEB). Geometrical matching and timing tracking are utilized to generate a preliminary Particle Identification (PID). This PID, however, might be considered a crude version and should be regarded as an initial reference only. Further stages will improve this selection based in refined methods. The last step in this chain consists in passing the BOS output file through the offline event reconstruction software (RECSIS). The information gathered by the sensors, such as charge deposited, momentum and energy of a track, and timing stamps, are written in a more friendly readable way. The processed data can be saved in different formats, being BOS banks and ROOT ntuples the most widely used.

The cooking process was initially performed by Lamiaa El Fassi and Lorenzo Zana in 2005. Later, in 2009, Taisiya Mineeva recooked the full data set due to several changes in the tracking and reconstruction procedures. These changes led to an improvement in the amount of statistics of nearly 50% in electrons and doubled the pion counts. Further information about the whole cooking and previous steps can be found in [19].

After the last cooking, the data was stored in ROOT files in a standard format referred to as ClasBanks, a set of classes defined in *ClasTool*. For easiness in the study, these files are reprocessed one last time. The content of the tuples is pruned with a proper PID according to previous works [1] [20] and translated to a vectorial-tuples format. A program called *GetSimpleTuple (GST)*[1] developed by J. López and A. Bórquez makes this process faster.

The GST program has the electron and pion's PID cuts implemented. A matching process relates a prompt electron, the first lepton detected of a bunch, with hadrons, fermions, and photons. These particles are considered candidates of being produced by the direct interaction of the electron with one of the targets. A *ROOT TTree* stores the relevant information of these particles in the following form:

- The scattered electron's information is saved as an entry with several branches.

[1] Github repository: https://github.com/utfsm-eg2-data-analysis/GetSimpleTuple/tree/csanmart/analysis-pion-phipq

These branches have information from different levels, such as momentum, energy, kinematic variables of it and of the virtual photon like Q^2, ν, x_b, detector coordinates, among others.

- ◇ The candidates are also saved but already matched to the electron they could come from. A vector-branch for each variable of the candidate is saved, with information of their energy and momentum, Z_h, $\gamma - p$ frame's variables such as ϕ_{PQ}, and the result of the PID using the Particle Data Group (PDG) numbering scheme. This means that every electron will have a set of vector-branches with as many elements as particles are associated to its initial interaction.

A crucial step in the offline reconstruction is a proper particle identification. New selection rules have presented samples with improved statistics and quality, as seen for charged pions for instance. A deeper explanation of the cuts used in the identification of electrons and positive pions for this analysis will be given. These selections were proposed and implemented in previous studies with remarkable results. The GST version utilized in this study has some updates with respect to other works [21]. The changes are introduced in order to be in line with the final selections implemented in the latest Analysis Note of the group [22].

5.2 Electron identification

A correct electron identification is crucial for the rest of the analysis since this will be the starting point of an event. A mis-identified electron could lead to a group of particles paired to the incorrect prompt lepton. We work under the assumption that the first electron of a bank is the scattered one.

The process begins by getting access to the data, saved in the silo. The data is read with the help of the ClasTool framework, that mimics the structures of the BOS banks. Firstly, from the ClasTool format, the response of every detector is saved as a number in reference to the quality of the measurement. Each bank has as many rows as particles with a track in the detector. The element must fulfill the following requirements to be preliminarily recognized as an electron:

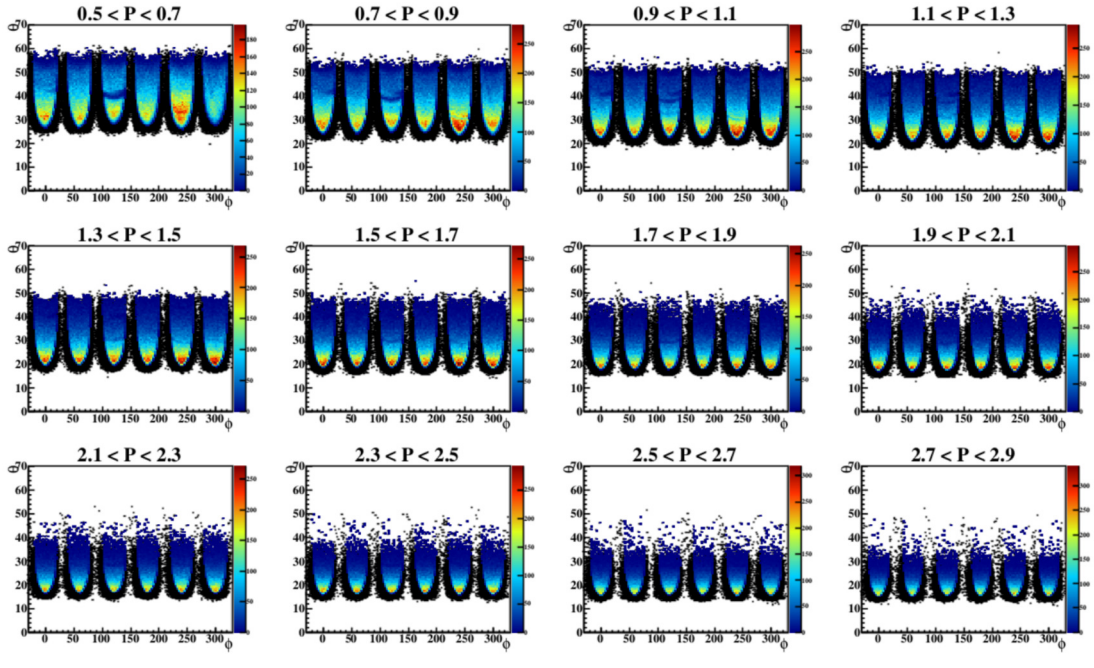

Figure 5.1: Fiducial cuts on DC.

- It is the first element (row 0) in the bank.
- The quality of the response in every detector (this is: DC, CC, TOF, and ECAL) must be greater than zero.
- The DC must get a positive outcome in both Time Based Tracking (TBT) and Hit Based Tracking (HTB) during the reconstruction process.
- The charge associated to the track must be negative (this is done by observing the direction of bending of the track in the DC).

Note that these initial rules were demonstrated to be insufficient to properly address the event as an electron. Certain detector effects, such as inefficiencies or track reconstruction issues, as well as the presence of other particles that could give a positive signal with this selections, make the identification more difficult.

In consequence, a long process of refinement has been developed to reduce these unwanted events. Cuts on the edges of the sectors, vertex cuts to limit the position of the initial interaction, and other methods have been studied and have presented a significant improvement in identification. A detailed overview of the selections is given in the next subsection, ordered by detector.

Table 5.1: Lower limit of the number of photoelectrons saved in the CC detector per sector. Extracted from [22].

Sector	0	1	2	3	4	5
n	25	25	26	21	28	28

5.2.1 Drift Chambers (DCs)

The six-sector structure of the system in the forward region has intrinsic dead zones in the gaps between layers. These zones should be uniformly distributed in the azimuthal direction, separated by 60° of each other, with a small length. However, effects on the edges of the active areas are not negligible and must be carefully studied. A rigorous method for removing these inefficient sections was performed in a previous Analysis Note by L. Zana [23]. They are known as *fiducial cuts* and restrict the laboratory coordinates θ and ϕ per sector. Note that this also removes the most-forward region (low θ) where energetic particles are not well reconstructed.

5.2.2 Cherenkov Counters (CCs)

The readout of the signal in the CC uses PMTs, making the response very sensitive to any other source of electromagnetic radiation. Fortunately, the main source of contamination comes from negative pions that are minimum ionizing and can be easily spotted by the number of photoelectrons recorded. A peak at low count values is attributed to this contamination. Better results were observed by removing the peak sector by sector using a slightly different threshold. For practical purposes, the number of photoelectrons stored internally is 10 times the actual measurement. We will use this definition and omit the factor for ease of reading.

The final cut requires

$$N_{phe} > n, \tag{5.1}$$

with n presented per sector in Table 5.1.

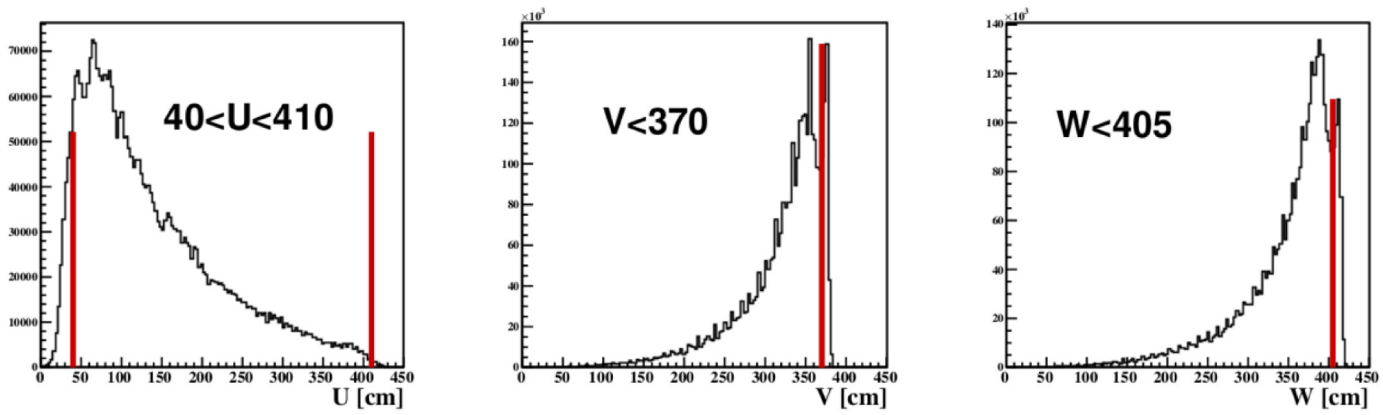

Figure 5.2: Fiducial cuts on ECAL.

5.2.3 Electromagnetic Calorimeter (ECAL)

Similarly to the DCs, a fiducial cut is implemented at the edges of the ECAL layers, where low efficiency is expected. Depending on the orientation of the layer we define a cut in its coordinate system. The position of the hit is defined perpendicular to the scintillator-bars.

Using the labeling given in Section 4.3.4, the cuts have the form (in cm units):

$$40 < U < 410, \qquad V < 370, \qquad W < 405, \tag{5.2}$$

and their effect can be seen in Figure 5.2.

The two sets of layers in the ECAL (inner and outer layers) will be useful in the removal of less energetic candidates. We denote the energy deposited in each group with the names E_{in} and E_{out}, respectively. Negative pions are the main source of contamination and in this section of the detector they can be considered Minimum Ionizing Particles (MIPs). This means that they are in a minimum region in the energy loss curve and, for all practical purposes, can be studied as if depositing an almost constant rate of energy through their pass in the inner layers. This feature will be exploited to remove the π^- contamination with the next two restrictions:

1. $E_{in} > 0.06\ \mathrm{GeV}$: This cut ensures that MIPs are removed. It is very effective since the π^- can be easily differentiated from the electron track as function of the energy deposited in the calorimeter.

2. $E_{out} > 0$: Since electrons should be energetic enough to still being alive at the

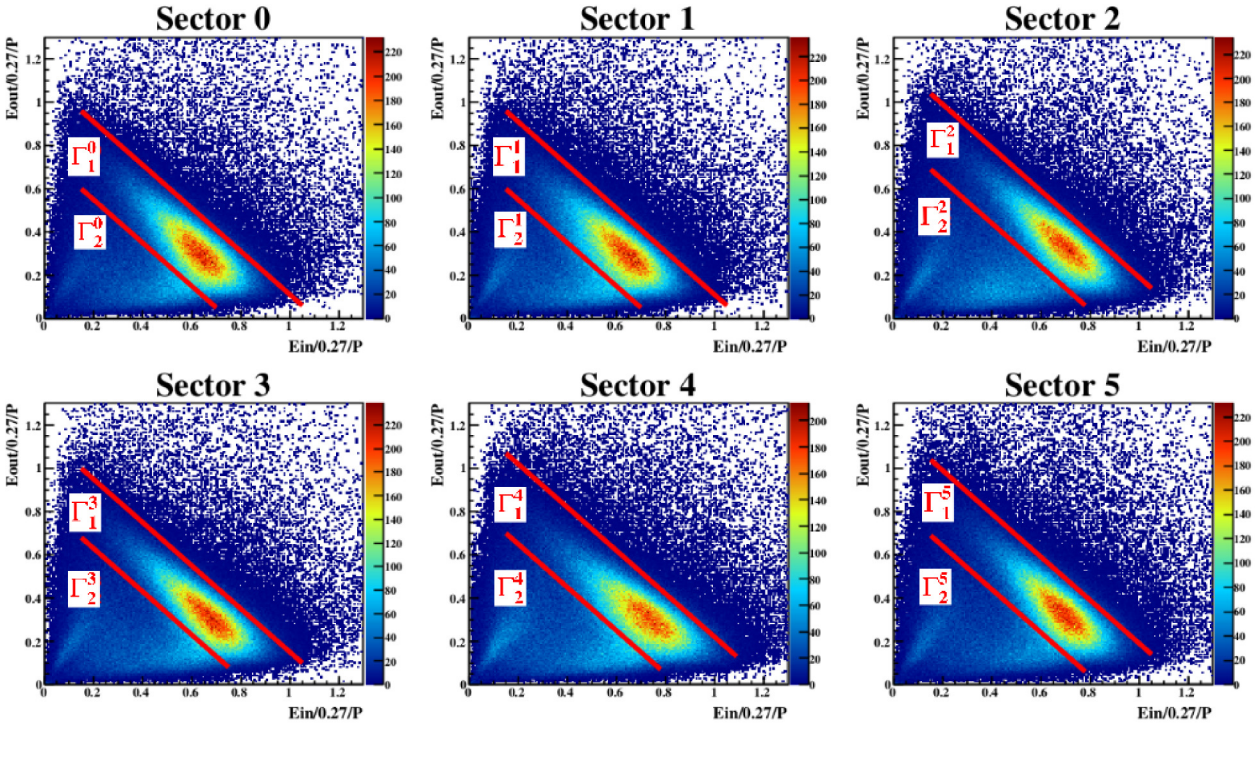

Figure 5.3: Energy cut on inner and outer regions of ECAL.

outer layers, this cut prevents contamination from low energetic particles, in line with kinematic restrictions presented later.

Using the momentum information extracted from the DCs, some extra conditions can be established for the energy-momentum ratio. Previous studies based on CLAS Geant simulations (GSIM) have demonstrated that the energy-to-momentum ratio for electrons should give values around 0.27. This number will be our reference.

The first condition relates both E_{in}/p and E_{out}/p ratios. Their dependence should lie between a band as seen in Figure 5.3, giving the general cut form:

$$a_1 p < \frac{E_{in} + E_{out}}{0.27} < a_2 p, \tag{5.3}$$

where the parameters a_1 and a_2 are found from a fit to the data in order to remove events that are far from the expected response. Moreover, a sector dependent study showed better results in reconstruction efficiency, leading to a total of twelve parameters to be determined.

The second condition is applied over the total energy in the ECAL. This quantity is expected to depend on the momentum in a linear way, giving the form:

$$b_1 p + b_2 < \frac{E_{tot}}{0.27} < b_3 p + b_4. \tag{5.4}$$

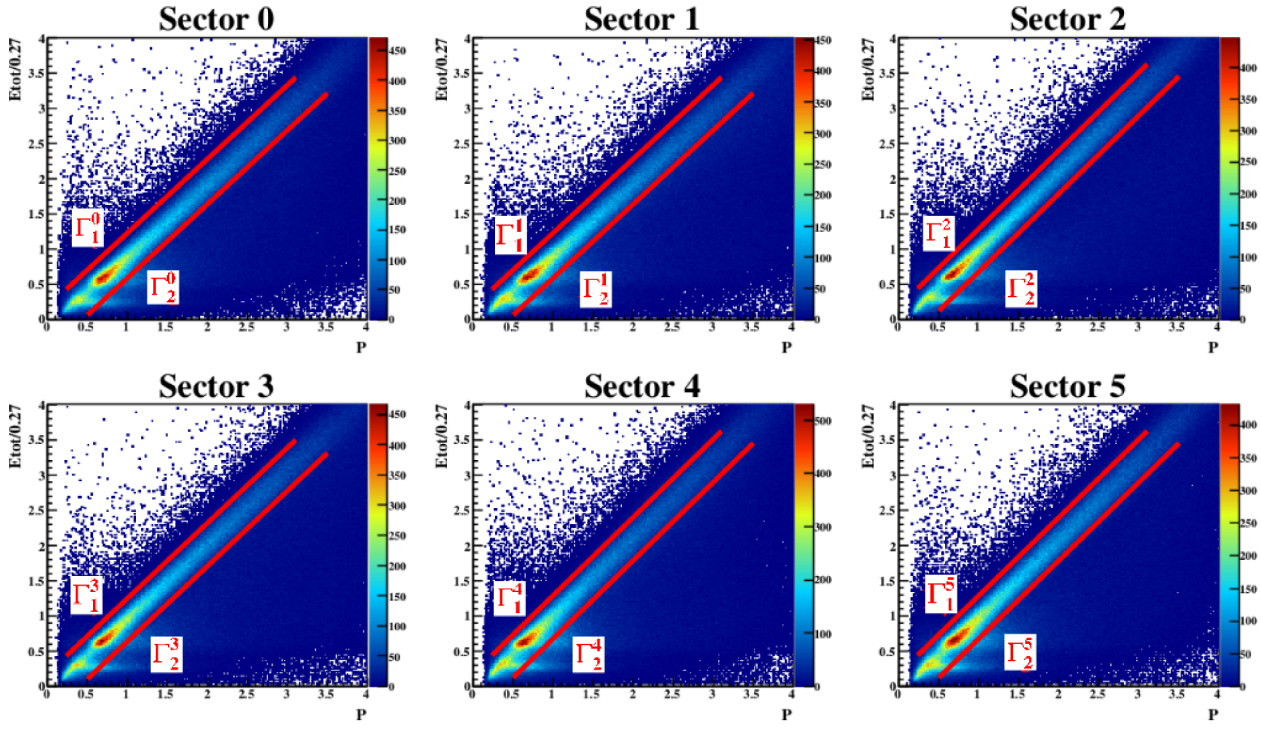

Figure 5.4: Energy cut on total energy of ECAL.

Similarly to the previous cut, the b_i parameters are established by inspecting Figure 5.4 in a sector dependent basis.

The final values obtained for both cuts are presented in Table 5.2.

Table 5.2: Energy-momentum ratio parameters for data per detector sector. Extracted from [22].

Sector	a_1	a_2	b_1	b_2	b_3	b_4
1	0.75	1.11	1.05	-0.46	1.05	0.18
2	0.75	1.11	1.05	-0.46	1.05	0.18
3	0.84	1.19	1.11	-0.43	1.11	0.18
4	0.83	1.15	1.07	-0.43	1.07	0.18
5	0.85	1.22	1.11	-0.43	1.11	0.18
6	0.84	1.19	1.11	-0.43	1.11	0.18

Since we have dealt with two definitions for the deposited energy in the ECAL, we will try to standardize it by working with $E \equiv \max(E_{in} + E_{out}, E_{tot})$. Another quality cut denoted as *sampling ratio* depends on p and presents a smeared distribution with a highlighted peak identified as the region of interest, presented in Figure 5.5. In order to improve the selection, we restrict the study to events lying inside a band defined by

$$\left| \frac{E}{p} - \mu(p) \right| < 2.5\sigma(p), \tag{5.5}$$

where both functions μ and σ are functions of p and are determined by a fit to the data.

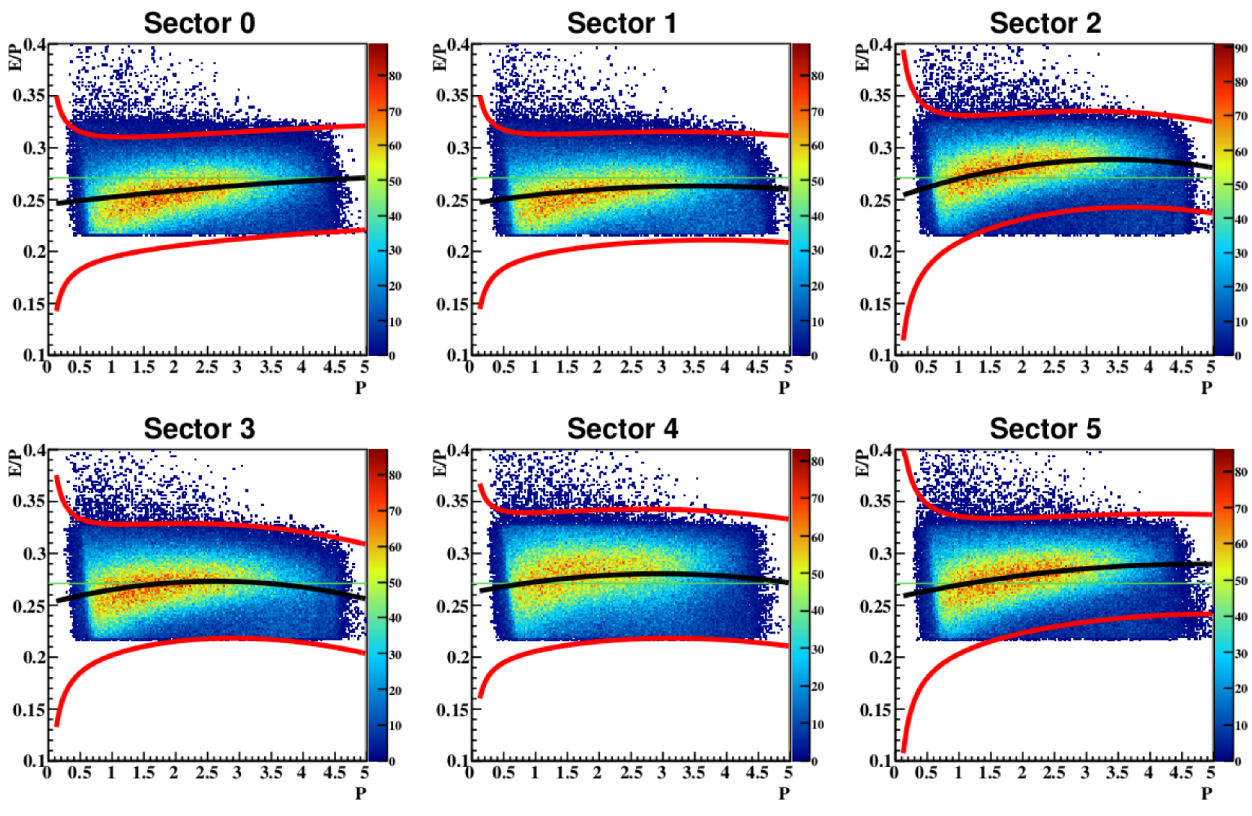

Figure 5.5: Sampling fraction in ECAL.

The functions were previously modelled by simulations and making use of the detector calibrations they were refined to follow the next expressions:

$$\mu(p) = c_1 + c_2 p + c_3 p^2, \tag{5.6}$$

$$\sigma(p) = \sqrt{d_1^2 + \frac{d_2^2}{p}}. \tag{5.7}$$

The fit of each function was initially performed by T. Mineeva [19] and revisited by S. Morán [22]. The values taken in this study come from the latter. It's important to stress the fact that the values were obtained depending on the sector and are different for different targets.

5.2.4 Time Of Flight (TOF)

A last cut relates the timing information from the TOF with the ECAL. Since both detectors are placed in a fixed position and the velocity of forward electrons doesn't change dramatically, we expect the difference of both time readouts to be approximately constant. Due to fluctuations, its value is assumed to be Gaussian-spread.

More precisely, the selection requires

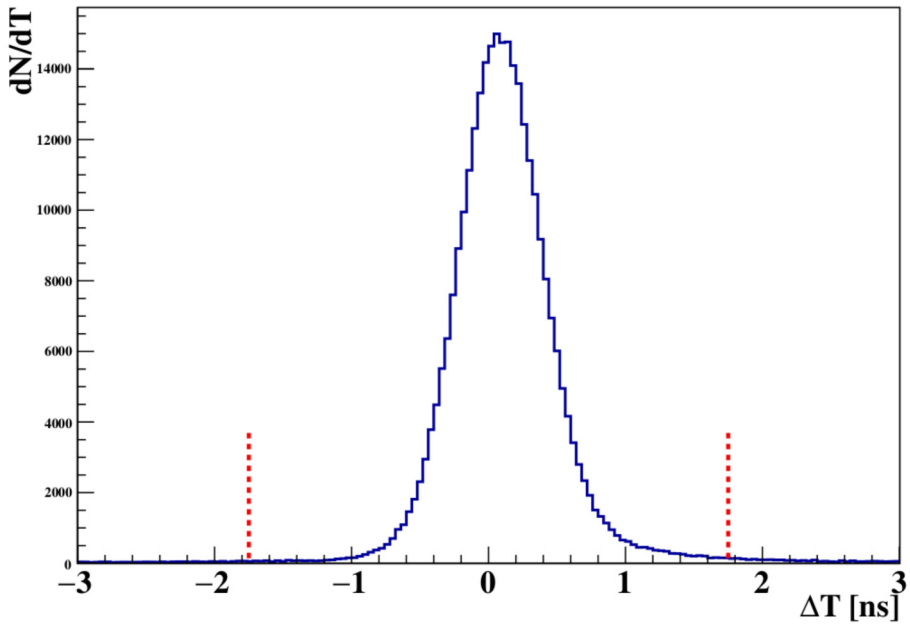

Figure 5.6: ΔT distribution in TOF system.

$$\Delta T \equiv \left| t_{\text{ECAL}} - t_{\text{TOF}} - \left(\frac{l_{\text{ECAL}}}{c} - \frac{l_{\text{TOF}}}{c} \right) \right| < 5\sigma, \tag{5.8}$$

where t_i and l_i are the arriving time recorded and fixed path length in the detector i, respectively, and σ is the standard deviation of a Gaussian fit performed over the distribution. The standard deviation required has a fixed value of $\sigma = 0.35\,\text{ns}$. The effect of this cut in the ΔT distribution is shown in Figure 5.6

According to previous reports, the total effect of applying all these cuts is a reduction in the counts of 80% to 85%. Given the high statistics of the experiment this is not prohibitive and the quality of the sample is increased. The same selection is applied for positrons but with positive charge required.

5.2.5 Vertex correction

Some comments are necessary in regard of the vertex determination. The vertex information is of high importance to address the event as a liquid or solid target interaction. As discussed in Section 4.4, the actual beam was found to be misaligned with the detector structure, making necessary a shift in certain quantities.

The three coordinates of the reconstructed vertex are saved as x, y, and z. A corrected version of the first two, shifted in the xy plane, is saved as xc and yc. This leads to a recalculation of z using an extrapolation of the interaction's location zc. A quality

cut is performed for the yc variable, restricting it to values of $|yc| < 1.4\,\mathrm{cm}$ to reduce background contamination in the zc position.

Even though the remaining entries have a clear vertex, some contamination is still visible especially from particles coming from the aluminum layer between the solid and liquid targets. A proper selection of interacting media can be done by adding another vertex cut on the expected position of the target.

This target determination follows (in cm):

$$\begin{aligned} &\text{Solid C target :} && -25.33 < zc < -24.10, \\ &\text{Solid Fe target :} && -25.65 < zc < -24.26, \\ &\text{Solid Pb target :} && -25.54 < zc < -24.36, \\ &\text{Liquid D target :} && -31.80 < zc < -28.40. \end{aligned}$$

The number of electrons is reduced in around 15% from the data over the remaining events after the detector-cuts. An in-depth explanation of the method used to get these values and the number of events rejected is presented in Reference [1].

Some post-processing cuts are also applied to restrict the kinematic region and reduce contamination. A further cut has been applied in W, the mass of the undetected particles. In order to reduce contamination from delta resonances we require $W > 2\,\mathrm{GeV}$. Also, the electron is required to carry a momentum that surpasses the minimum sensitivity threshold of the detector. The minimum value is slightly raised for purity reasons to $p > 0.75\,\mathrm{GeV}$. This is equivalent to impose the candidate to carry $y_b < 0.85$.

5.3 Positive pion identification

Candidates for electron/positron that have not passed all cuts are included in a second list of candidates for charged pions. In principle the same analysis should be applicable to both positive and negative pions. However, the polarity of the magnetic field affects the trajectory of them in opposite ways and the efficiency of detection with some components of the detector is not as good as with electrons. For instance, a detector that gave a sufficient signal to identify an electrons by its own might not have interacted with a

less energetic candidate to pion. This forces us to join information from more than one sensor at a time. Also, the principle of operation of detectors such as the CCs requires an energy threshold to leave a track, requiring different selection's criteria at different levels of energy.

In a similar way to the first requirement for electrons, the ClasTool format must follow:

- ◇ There is a correct electron trigger associated with the event (this is, the first element in the bank's row was an electron).
- ◇ The quality of the response in every relevant detector (DC, CC, and TOF)[2] must be greater than zero.
- ◇ The DC must get a positive outcome in both Time Based Tracking (TBT) and Hit Based Tracking (HTB) during the reconstruction process.
- ◇ The charge associated to the track must be positive.

Later, we apply new detector cuts similarly to the exposed in the last section.

5.3.1 Time Of Flight (TOF)

The TOF system extends over a big momentum range (see Section 4.3.3), interacting with all kinds of ionizing particles. This motivates the definition of a time window between the detection of the scattered electron and the pion candidate for a correct correlation of the events. It has been demonstrated, however, that the method must be momentum dependent. Since the more momentum carried the less time of travel through the TOF, this hinders the response of scintillators. Also, the interaction of other positive particles such as kaons or protons produce a peak that, in certain momentum regions, is indistinguishable from the pion's one.

The time correlation's expression has the form:

$$\Delta T_{\pi^+} \equiv \left(\frac{l^{e^-}_{\text{TOF}}}{c} - \frac{l^{\pi^+}_{\text{TOF}}}{v^{\pi^+}} \right) - \left(t^{e^-}_{\text{TOF}} - t^{\pi^+}_{\text{TOF}} \right), \tag{5.9}$$

where l^{j}_{TOF} and t^{j}_{TOF} are the track length and timestamp of the interaction measured in

[2] Note the absence of an ECAL signal due to the limitations commented above.

Table 5.3: Time window limits of ΔT_{π^+} cut with the momentum range of applicability. A double horizontal line marks the maximum momentum value where the method is useful. The last rows are used for consistency.

Momentum (p_{π^+}) GeV	τ_{min} ns	τ_{max} ns
[0.00, 0.25]	-0.70	0.70
]0.25, 0.50]	-0.70	0.65
]0.50, 0.75]	-0.70	0.65
]0.75, 1.00]	-0.70	0.65
]1.00, 1.25]	-0.55	0.55
]1.25, 1.50]	-0.50	0.55
]1.50, 1.75]	-0.50	0.40
]1.75, 2.00]	-0.48	0.40
]2.00, 2.25]	-0.50	0.40
]2.25, 2.50]	-0.50	0.40
]2.50, 2.70]	-0.50	0.40
]2.70, 3.30]	-0.60	0.45
]3.30, 3.70]	-0.60	0.50
]3.70, 6.00]	-0.60	0.50

the TOF system for the particle j being the trigger e^- or the π^+ candidate, and c and v^{π^+} their respective velocities.

The cut imposes $\tau_{\text{min}} < \Delta T_{\pi^+} < \tau_{\text{max}}$, and the τ_j values are presented in Table 5.3 with their momentum range of applicability. Note the distinction in the row that ends in $p = 2.7\,\text{GeV}$, which is the maximum momentum value where this method is reliable. For consistency, the cut is still applied after that value, though its impact is negligible.

5.3.2 Cherenkov Counters (CCs)

High momentum pions (over $p = 2.7\,\text{GeV}$) are usually at the forward region and are energetic enough for leaving a track on the CC. A geometrical matching is required between the position of the CC and TOF hit, as well as a minimum number of photoelectrons. The angle subtended by the two hits position must be smaller than 5° and photoelectrons follow $N_{phe} > 15$.

Around 9% of the events pass the successive cuts, making the cuts tight enough for getting significant statistics.

5.3.3 Vertex correction

Pions coming from extra decays or external processes are not desired and the same idea of correlating two hits used so far is useful here. We can extrapolate the vertex position of the hadron and impose this position to be near the scattered electron vertex (after correction, of course). This relation is expressed as (in cm):

$$\Delta z \equiv |z_{\pi^+} - z c_{e^-}| < 3.0, \tag{5.10}$$

where the electron vertex is corrected as described in Section 5.2.5.

This cut does not impact significantly on the statistics of the data set, so its relevancy is a matter of consistency.

Chapter 6

Simulations management

Long before the actual data acquisition, the experiment and its objectives must be specified in great detail to be approved and to foresee and fix any possible problem on the experiment regarding the samples, readout system, or detector's component response. One of the main tools we have for demonstrating the feasibility of the experiment even before its commissioning is the use of *simulations*. Moreover, the use of simulations is crucial for accounting for any inner source of unwanted signals, making possible to get a cleaner environment only by optimization. These considerations are fundamental for this study and will be discussed along this chapter and in the next one.

Different specialized software can be utilized for simulating the interaction of a beam of particles with a sample of interest. The specifications of the setup are inputs in the software. The description given in Chapter 4 are followed, requiring an electron beam and the different media corresponding to the solid and liquid targets.

Among the mostly known programs we find *LEPTO* and *Pythia*, which introduce specific features that make one or the other a better candidate for the study. Pythia was the generator selected and more information on its capabilities, a presentation of the simulation set and its characteristics will be described bellow.

In the last section, all the cuts performed are treated in an identical way to the previous chapter.

6.1 Simulations and processing

There exist plenty of models and softwares with their own implementation available. However, regardless of the generator selected, the process for getting the simulation final files follows this sequence of steps:

- ◇ Monte Carlo (MC) generation
- ◇ CLAS Geant simulation (GSIM)
- ◇ GSIM Post Processor (GPP)
- ◇ Offline event reconstruction software (RECSIS)

The two former elements (MC and GSIM) are simultaneously implemented. The selected generator has a physics model for the interactions and restrict what processes are possible or forbidden. This creates a file using a Monte Carlo technique. Note that every model has its own limitations thus defining a range of applicability for them. This step is important since the hadronization process must evolve in a realistic way and should be properly modelled to be able to represent the quantities of interest for the study in the most correct form. In other words, quantities such as cross sections, multiplicity ratios, P_T distributions, among others, in general depend on the input and the interactions that are available in the generator.

Along with the MC step, the detector response and its impact over the generated particles' output, like degradation of the signals, must be considered. For instance, recall the position of the deuterium target upstream. This could induce to extra interactions of the scattered particles with the solid target that's in front or the support structure. The interactions mentioned comprise effects such as energy loss, deviation of the tracks, and radiation of secondary particles. The simulations will quantify them and an optimized configuration should reduce them to a negligible level.

The detector is implemented using a set of GEANT3 simulation packages for the CLAS structure, making use of the so called CLAS Geant simulation (GSIM) program. This step was carefully thought out in advance for the preparations of the data taking campaign. The packages were initially developed by CERN with their own installations in mind. Nevertheless, adapted versions with the base CLAS spectrometer configuration were created

by the CLAS collaboration. Furthermore, a package with the double target system was developed and implemented by H. Hakobyan. For the sake of simplicity, the only parameters required for tuning after getting the full experiment configuration implemented were the targets' geometry, this is, their dimensions, composition, and location inside the structure. Ideally, a large number of events should be simulated in order to cover all phase space with significant statistics. This was partially achieved, limited by the reduced running speed of the simulation program.

Although the output is essentially what we want, fine considerations should be addressed for better results. The GSIM Post Processor (GPP) is a software that passes the simulation through an extra layer with the real information of the state of the detector at running time. That is, it's in charge of adding detector defects such as problems on reading strips or broken tubes in the scintillators, for instance. The output is a more realistic version of the simulation and can be directly compared with data.

The last step is the offline reconstruction RECSIS that was also present in Chapter 5. The reconstruction's algorithms are exactly the same as in data and were run in an identical way for consistency.

Returning to the MC generator, *Pythia* was chosen because it satisfies the requirements of the experiment the best. Pythia contains a model of soft (non-perturbative) processes, as well as perturbative DIS available at different ranges of virtuality (Q^2) of the interaction. Initially, Pythia was mainly intended to be useful for leptonic collisions and was extended to hadron's interactions with an evolution's model based mainly on earlier experiments, this was a more phenomenological modelling. This last technique is not uncommon since QCD is not fully understood at theoretical level and those interactions that were not well described, could be fixed by retrieving past results. This approach, however, is not perfect and makes the generator even more sort of a ´black box'. A solution on one of the crucial parts of the process, the hadronization, came along with another parallel generator known as *Jetset*. Jetset was developed by the same group precursor of the Lund string model (comments on this in Section 3.4). In the late 90's both programs converged and ended up merged in a new version of Pythia. With all the previous features of both sides, Pythia represents a robust tool that has also demonstrated its capabilities

by predicting PETRA results on e^+e^- annihilation and helping in results from plenty of laboratories around the world such as LHC and Tevatron, among others [24]. Since the generator was specialized on high energy collisions, some parameters were tweaked to match the configuration in CLAS. Taking as starting point another Pythia's implementation made for HERMES, the final production covered the semi-inclusive region required for CLAS.

A full characterization of the hadronization process and QCD unresolved features such as color confinement are topics of interest for our group. The study of hadronization in the parton model had some features not yet implemented in the generators at running time, so they were included with other techniques. This is the case of the Fermi motion that affects the bounded partons. This was done 'outside of the model' by adding a smearing in the initial transverse momentum of the quark with a Gaussian distribution as explained in [20]. Another consideration relevant for the analysis is the inclusion of some runs with a displaced beam position. This is very important since at running time the beam is ideally kept perfectly centered, but it is impossible to maintain its position absolutely steady. Moreover, as explained in the previous chapter, a striking displacement of the beam was found [19] making this contribution even more valuable. One last interesting remark is the assumption of factorization and negligible interference terms in higher order processes such as photon or gluon bremsstrahlung and loop diagram corrections. This allow us to consider them in a post-processing level separately (see Radiative Corrections, for instance).

The final simulation files were created by Hayk Hakobyan making use of *Pythia 6.319* as the event generator and saved in *root* format. They still require the use of extra packages such as *ClasTool* to get access to the full information, however. The set was stored at the Jefferson Lab's silo and is available for members of the collaboration. The simulations in this state are useful and ready for analysis, but they are heavy and recent studies have presented improvements in the particle identification [22]. Also, the cuts described below are not expected to vary during the analysis so all of them will be applied in an extra pruning of the data carried out by the GetSimpleTuple program already introduced for data. This will leave the files in their final state, ready to work and only with the

required information, improving the performance of the analysis and accelerating time-consuming studies.

6.2 Electron identification

For the sake of completeness the large majority of cuts implemented in data are applied in the very same way to simulations. Nevertheless, some coefficients were tested and recalculated to obtain a better performance.

The initial requirements (such as positive detector response) and the following selections in DC (fiducial cuts), CC (photo-electrons' cut), and TOF (coincidence time with ECAL) systems are identical to data and can be checked in Section 5.2. Some cuts, like the CC cut introduced before, are intended to remove features that were observed in data, such as a prominent N_{phe} peak at values near zero. Even though this kind of issue is not present in the simulations, we keep using the cut with a negligible impact for consistency reasons.

6.2.1 Electromagnetic Calorimeter (ECAL)

We find some differences in the cuts applied on the ECAL response. The fiducial cuts (in U, V, and W orientations) and the minimum energy deposited in the layers of the calorimeters ($E_{out} > 0$ and $E_{in} > 0.06\,\mathrm{GeV}$) are the same as in data. However, the parameters tuned for the boundaries of energy deposition and the sampling fraction are specific for simulations.

The expressions presented in Equations 5.3 and 5.4 need five parameters that were fitted from simulations. The values are summarized in Table 6.1. The nominal values are not very different from what was obtained in data, but its impact in the rejection of events was not trivial so a correct tuning for these sets was required.

The same happens with the sampling fraction defined in Equation 5.5. The values are not presented here but can be found in [22] with a detailed description of the numbers found for the different targets and sectors. The details include the values obtained for the different targets, including deuterium. Note that data imposes the same cut in deuterium

Table 6.1: Energy-momentum ratio parameters for simulation per detector sector. Extracted from [22].

Sector	a_1	a_2	b_1	b_2	b_3	b_4
1	0.79	1.13	1.03	-0.42	1.05	0.21
2	0.79	1.13	1.03	-0.42	1.05	0.21
3	0.79	1.14	1.05	-0.46	1.05	0.21
4	0.79	1.14	1.03	-0.44	1.03	0.23
5	0.79	1.15	1.06	-0.46	1.06	0.20
6	0.79	1.14	1.04	-0.47	1.04	0.22

as in the corresponding solid target studied in parallel, thus a dedicated deuterium result is not suitable and we will separate the study of them restricted to the use of a specific solid sample. However, simulations don't have to deal with this issue and dedicated simulations for deuterium were processed. This is considering the displaced vertex from the upstream location of the liquid target. The nominal results are not extremely different from those found in data, but it's better to use their own results.

6.2.2 Vertex correction

The vertex determination is important in the identification and some words are saved for it. In the data we applied an explicit correction of the beam's position due to a shift found with respect to the center of the detector. In simulations we have a y_{shifted} set that emulates the effect of a displaced center in barely half of the files. However, the restriction in the yc coordinate is not implemented. Also, the determination of the target the track is coming from is not made using a vertex cut but just looking at the target used in the simulation, since all three solid plus deuterium liquid targets were simulated separately. Some variations of this cut have been tested in other studies, but this approach is simpler and results demonstrated to be the same in practice.

The post-processing cuts in W and y_b presented in data are also applied to simulation. So a minimum of $W > 2\,\text{GeV}$ and a limit $y_b < 0.85$ are required.

6.3 Positive pion identification

The positive charged pions had the same treatment in simulations as in data. The requirement of a non-null signal in the detector layers, positive charge of the track, ΔT within a range in the TOF system, as well as a N_{phe} threshold in the CC for tracks with momentum higher than $2.7\,\mathrm{GeV}$ are all presented and described in Section 5.3.

Consistency pushes us to leave as many cuts untouched as possible. For instance, the vertex cut presented in Section 5.3.3, where the vertex position reconstructed for the electron and the pion must lie closer than $3.0\,\mathrm{cm}$, does not remove any significant amount of events. However, it is still applied to keep a certain uniformity in the analysis.

Chapter 7

Acceptance and Closure Test

One of the crucial steps in the analysis regards the interpretation of the data with as few systematic detector effects as possible. This includes the possibility of getting certain portions of the phase space not fully covered. Empty or less populated regions could lead to biasing in the interpretation of data or to incorrect results. A variety of sources could produce these effects, including efficiency of detection and reconstruction, the intrinsic resolution of the detector's components, unexpected events at data taking that were not issued with simulations, or the geometry of the detector. In an ideal situation, the detector's response is perfect and both, simulations and data, are exactly the same so no correction should be needed. In real life, certain kinematic regions are not fully covered and we must compensate these effect by means of simulations.

The acceptance is introduced as a factor that accounts for the effects exposed above. Some studies use different factors, splitting our definition into a product of contributions from a variety of sources. This approach is ideal to quantify the effect of those sources individually. A quality test was developed in order to quantify how reliable these factors are. The method denoted as *Closure Test* is presented along with a description of its applicability and some results. Note how all these results depend directly on the binning selection, since the statistics in certain regions could hide features in the distributions, for instance. A discussion on possible alternatives to acceptance or better tests is shown at the end of the chapter.

7.1 Acceptance

Our objective is to extract the original distribution of electrons and pions from the data. As it was claimed, there are effects in data that distort the real distributions and our only way to fix it is simulations. The discussion in Chapter 6 presented the extensive work developed for getting an accurate model of the whole process. The files have a realistic detector's response that makes the data correction more direct. However, limitations of the experiment that forbid us to cover the full phase space can impact on our capacity of correction. To avoid this problem, some kinematic regions of the simulation have been artificially populated, i.e. got more statistics, in order to have a more complete characterization of the detector.

The correction method is called *Acceptance correction* and it is a scale factor applied in an event by event basis. Running over an established binning in the data, the acceptance is introduced in a five-dimensional grid to the data in order to compensate for the reduction of the counts produced by the inevitable effects described before. Depending on the statistics available and the observable under study, some analyses could be benefited by the use of a lower-dimensional grid in the process. This could increase the statistics at the cost of a higher dependency on the initial physics model of the interaction.

Mathematically, the factor for a given bin of Q^2, ν, Z_h, P_t^2, and ϕ_{PQ}, is determined by

$$A\Big|_{Q^2,\nu,Z_h,P_t^2,\phi_{PQ}} = \frac{N_{\text{reconstructed}}(Q^2,\nu,Z_h,P_t^2,\phi_{PQ})}{N_{\text{generated}}(Q^2,\nu,Z_h,P_t^2,\phi_{PQ})} \tag{7.1}$$

If the reconstructed and generated bins should be selected by their kinematic variables at reconstructed or generated level is a matter of discussion. Given certain circumstances this factor can be thought of as an efficiency of reconstruction. This last interpretation, however, is valid only when the effects of bin migration and/or other reconstruction flaws are negligible, which is generally not the case.

The different combinations are defined below and for the sake of completeness they will be contrasted. In order to denote whether a variable is at generated or reconstructed level, a left subscript is added (${}_gQ^2$ or ${}_rQ^2$, respectively).

1. Direct selection: The reconstructed event is selected independent of the generated (that is, there are mis-matched events accepted).

$$A\Big|_{Q^2,\nu,Z_h,P_t^2,\phi_{PQ}} = \frac{N_{\text{reconstructed}}({}_rQ^2, {}_r\nu, {}_rZ_h, {}_rP_t^2, {}_r\phi_{PQ})}{N_{\text{generated}}({}_gQ^2, {}_g\nu, {}_gZ_h, {}_gP_t^2, {}_g\phi_{PQ})}$$

2. Matching selection with reco. vars.: The reconstructed event is accepted only when it is correctly associated with a generated particle. The reconstructed bin is selected according to its *reconstructed* coordinates.

$$A\Big|_{Q^2,\nu,Z_h,P_t^2,\phi_{PQ}} = \frac{N_{\text{reconstructed}}({}_rQ^2, {}_r\nu, {}_rZ_h, {}_rP_t^2, {}_r\phi_{PQ}|\text{match generated})}{N_{\text{generated}}({}_gQ^2, {}_g\nu, {}_gZ_h, {}_gP_t^2, {}_g\phi_{PQ})}$$

3. Matching selection with gen. vars.: The reconstructed event is accepted only when it is correctly associated with a generated particle. The reconstructed bin is selected according to its *generated* coordinates. This last difference is of major importance since the numerator will always be smaller than the denominator by definition which leads to the interpretation of this method as an efficiency.

$$A\Big|_{Q^2,\nu,Z_h,P_t^2,\phi_{PQ}} = \frac{N_{\text{reconstructed}}({}_gQ^2, {}_g\nu, {}_gZ_h, {}_gP_t^2, {}_g\phi_{PQ}|\text{match generated})}{N_{\text{generated}}({}_gQ^2, {}_g\nu, {}_gZ_h, {}_gP_t^2, {}_g\phi_{PQ})}$$

A discussion on the interpretation of each method would clarify what information is actually given and could help in understanding what is the best option.

Starting from the last presented, when we require a match in the selection of the event we are explicitly removing possible mis-matches from errors in the algorithm of reconstruction or detector inefficiencies produced in the reconstruction process. Also, the use of generated variables in both numerator and denominator, gives the possible interpretation of the factor as an efficiency of detection. Basically, we select a generated particle and add a count when it was correctly reconstructed as a pion (independent of its kinematics) and none if it is not reconstructed. This last point reflects the flaw of this method: we only see if we correctly reconstruct a pion, but not the kinematic bin (i.e. assumes or neglects bin migration).

The previous method ("Matching selection with reco. vars.") matches the pion but it

also accounts for the reconstruction. This explicitly accepts and quantifies bin migration, so its implementation gets better the smaller the migration.

The first method presented ("Direct selection") is the easiest to implement but harder to interpret since it hides different effects in a single factor. For instance, we are mixing reconstruction, bin migration, and matching effects without clear understanding on their individual effects. However, this level of detail might not be necessary under the assumption of a well behaved reconstruction. This statement will be revisited later, by comparing the results obtained with the different methods in a simple quality check.

Before going further it is worth mentioning the propagation of uncertainty present in the calculation of these factors. It is clear that independent of the method under use both numerator and denominator are related sets of values (the reconstructed and the generated, respectively). The response of the detector in the presence of a particle in this scenario can be modelled as a binomial event, this is, the event is dichotomous because the response of the system after getting a particle generated can be positive (correctly detected) or negative (not detected).

Remember that for a binomial distribution with $A_i = N_i^{\text{reco}}/N_i^{\text{gen}}$ the standard deviation is given by

$$\sigma_i^A = \sqrt{\frac{A_i\left(1 - A_i\right)}{N^{\text{gen}} - 1}}, \tag{7.2}$$

taking N^{gen} (the number of generated events) to be equal to the number of entries in this bin of acceptance. Even though this expression looks reliable, a second look at it reveals that it is incomplete because the uncertainty information of both, numerator and denominator, is not playing a role so there is information loss. A correct formula was proposed and has been already implemented in *ROOT* under the option 'B' when using the method `TH1::Divide`. The expression was derived using a maximum likelihood approach proposed in [25] and takes the form

$$\sigma_i^{\text{acc}} = \sqrt{\frac{\left(1 - 2A_i\right) \cdot \left(\epsilon_i^{\text{reco}}\right)^2 + A_i^2 \cdot \left(\epsilon_i^{\text{gen}}\right)^2}{\left(N^{\text{gen}}\right)^2}}, \tag{7.3}$$

where A_i and σ_i^{acc} are the acceptance factor and the error associated to it for a given bin i, N^{gen} is the number of generated events, and ϵ_i^j is the error in the i bin for $j = \{\text{gen}, \text{reco}\}$.

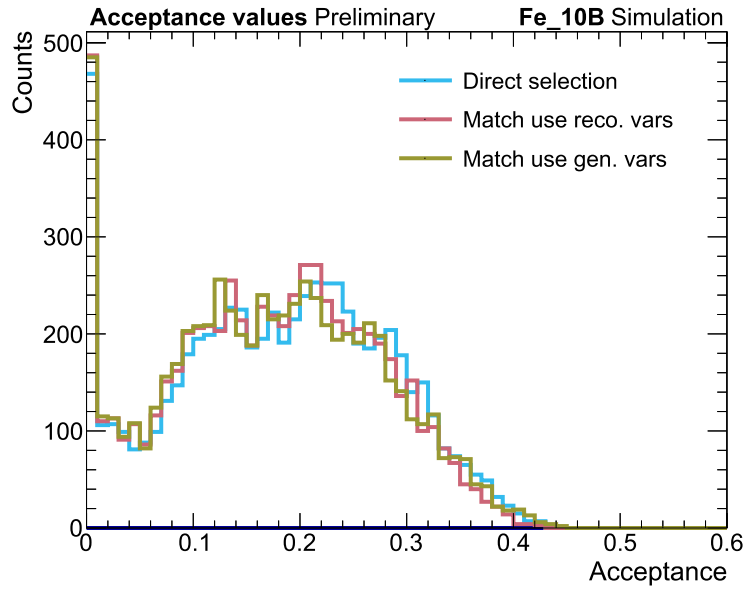

Figure 7.1: Acceptance factors calculated in a 5-fold basis. The methods are named as described in the text.

All three definitions of acceptance were implemented with similar results presenting small deviations only, as shown in Figure 7.1. The factors obtained by the three methods are very similar when comparing them bin by bin. Nevertheless, the presence of a peak at zero reveals a lack of entries in the simulation in a large number of bins. The presence of these empty bins in the simulation is dangerous since the correction of data will be incomplete, reducing the quality of the correction and affecting the validity of any result.

To get intuition about the source of these problematic bins, the empty elements were projected as a function of the kinematic variables. Special care was taken inspecting the ϕ_{PQ} dependence, presented in Figure 7.2. The zero factors were present over all the azimuthal space but with a predominant peak in the center (around $\phi_{PQ} \sim 0$). This trend resembles a historical issue in the data, where an enormous peak at this very same section is presented and attributed to unknown processes of higher level. Further studies on the impact of the acceptance and the treatment of this peak in the data are part of next steps in the study and will be discussed in Section 8.1. Even though this problem can not be easily attacked, the analysis can still be done by making use of different strategies presented in the referenced section.

7.2 Binning

Selecting a suitable binning is an important task and there is no unique way of testing if the choice is the right one. Different properties of the samples and features on the

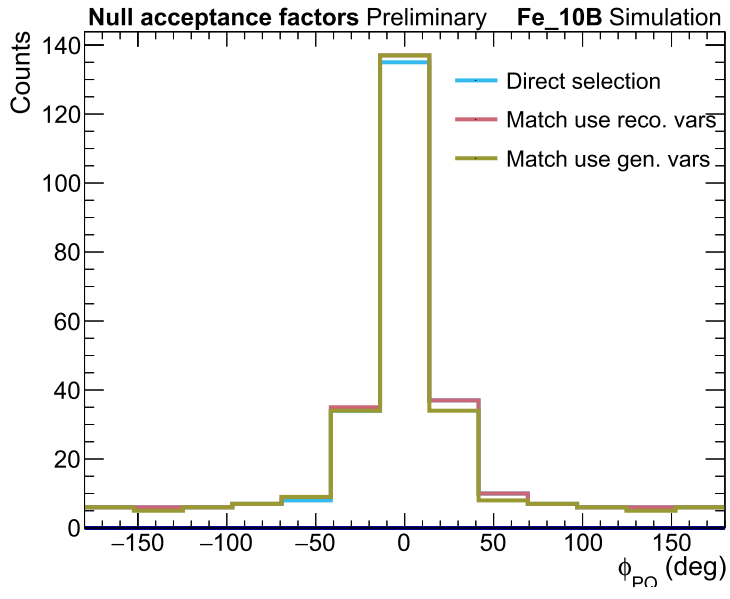

Figure 7.2: Empty bins distribution as function of ϕ_{PQ} for the different methods of acceptance calculation. The methods are named as described in the text.

Table 7.1: Resolution values of the kinematic variables' reconstruction. These numbers are regarded as a lower boundary for the bin width.

Variable	Q^2	ν	X_b	Z_h	P_t^2	ϕ_{PQ}
Resolution	$9{\cdot}10^{-3}\,\mathrm{GeV}^2$	$8{\cdot}10^{-3}\,\mathrm{GeV}$	$5{\cdot}10^{-3}$	$3{\cdot}10^{-3}$	$4{\cdot}10^{-3}\,\mathrm{GeV}^2$	$0.4°$

binning can help us to determine if a selection could be improved but no method can give 'the best' bin.

We begin by introducing the reconstruction's resolution of a variable. This number quantifies the inaccuracy of the reconstruction and restricts our bin's length to be smaller than it. It can also be interpreted as a measure of bin migration. If the bin length chosen is comparable or smaller than the resolution found, aliasing effects as well as other distortions of the distributions could happen, making the process less reliable. For instance, small bins in the acceptance will impact with an inherent huge bin migration, reducing the effectiveness of the correction. The resolution is not constant across the kinematic region studied. The average values were found for the variables and will be used as a limit for the length chosen. These numbers are presented in Table 7.1.

Another consideration in the binning selection must be the statistics. Each block should be selected so that contains a significant number of events, in order to give a trustful result. This last reason makes the approach of an irregular binning desirable for accounting regions with less statistics. Moreover, to get a better result of the corrections in regions that are expected to receive less interactions, the simulations had accounted this by increasing the amount of events recorded in those zones. This solution might seem ar-

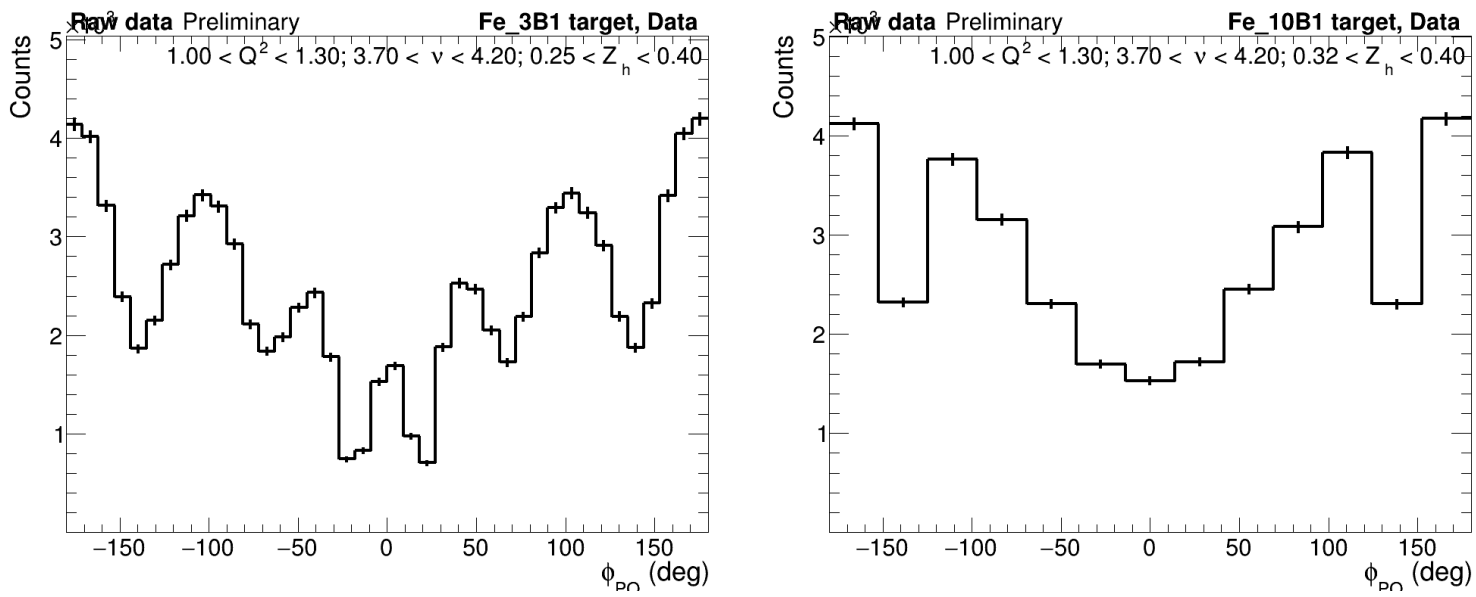

Figure 7.3: Different selections of ϕ_{PQ} binning: 40 bins (left) and 13 (right) in not corrected (raw) data. Coarser bins average over a higher zone, reducing the granularity of the study and removing important features.

Table 7.2: Nominal binning used in the analysis. The first half represents leptonic variables and the second half hadronic ones. Only ν or X_b is used at a time.

Variable	Bins limits	# bins
Q^2	[1.00, 1.30, 1.80, 4.10]	3
ν	[2.20, 3.20, 3.70, 4.20]	3
X_b	[0.110, 0.220, 0.290, 0.560]	3
Z_h	[0.10, 0.22, 0.32, 0.40, 0.50, 0.60, 0.75, 0.85, 1.00]	8
P_t^2	[0.047, 0.073, 0.112, 0.173, 0.267, 0.411, 0.633, 1.2]	7
ϕ_{PQ}	[-180.00, -152.31, -124.62, -96.92, -69.23, -41.54, -13.85, 13.85, 41.54, 69.23, 96.92,124.62, 152.31, 180.00]	13

tificial at first but we need to recall that the necessity of simulations, at least for the correction point of view, arises as a means to account for the detectors' effects, which is independent of the original distribution. Also, getting higher statistics in some regions would only improve the performance of the corrections in there.

The shape of the distribution is also an aspect to consider. There might be features that are easily spotted with a given bin's length but a coarser option could hide them by imposing an implicit average of the mixed bins. Uniform regions provide a good environment for wide bins. On the other hand, distributions with sections of varying height will require a narrower selection. This is the case observed in the ϕ_{PQ} distribution presented in Figure 7.3, where certain selections tend to reduce the height of the peaks and, in some cases, get them completely removed.

The final bin selection is presented in Table 7.2.

7.3 Closure Test

Although our binning satisfies the minimum requirements, the acceptance could have deficiencies we would like to account. One way of checking the quality of the acceptance is known as *Closure Test*. The method uses part of the simulation as data to reproduce the effect of the acceptance correction in a safe environment. For doing so, the whole simulations' set is separated into two groups. The first half will be used to calculate the acceptance factors as usual (see previous section). Having the resulting factors saved, we apply the correction to the second half of **reconstructed** variables. Since the simulations have both generated and reconstructed information, we can easily verify any discrepancy between the expected (generated) and the 'corrected' set. Ideally, both quantities perfectly match and the acceptance is trivial, giving a Corrected:Generated ratio of 1. Any deviation of the ratio from 1 implies an inaccuracy in the correction. Though fluctuations are always expected, big effects are a bad symptom of a poor acceptance. If the curve lies within a band of tolerance near 1, the acceptance is said to be *Closed*. If not, the correction is *Not closed* and it is not applicable.

A five-dimensional acceptance was calculated using the nominal binning. The Closure Test is presented in a three-dimensional basis, that is, the results will be given in bins of Q^2, ν, and one of the hadronic variables: Z_h or P_t^2, as a function of ϕ_{PQ}. The remaining variable is integrated out (P_t^2 or Z_h). An example of a good and a bad bin is presented in Figure 7.4.

The values of closure are summarized in Figure 7.5. There exist some bins with clear problems, especially at central values of ϕ_{PQ}. Low statistics regions in simulation also reduce the quality of the correction by introducing empty acceptance bins, for instance. In summary, we see a resulting close level of 0.98 ± 0.12 for the Z_h dependence and 0.99 ± 0.07 for P_t^2. The local differences with the ideal response per bin could be addressed as a systematic error when correcting the data.

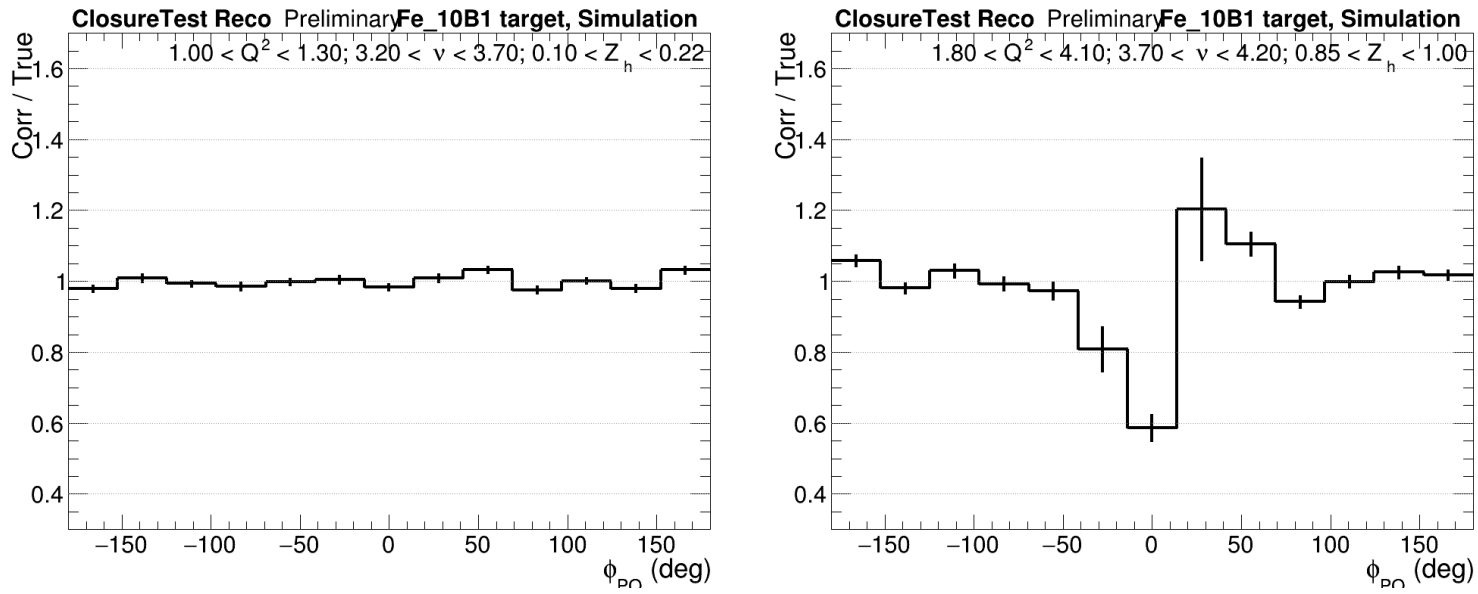

Figure 7.4: Result of Closure Test in a well-behaved bin (left) and a bad one (right). The 3-dimensional bin depends on Q^2, ν, and Z_h. Note the worse performance is predominantly at central events.

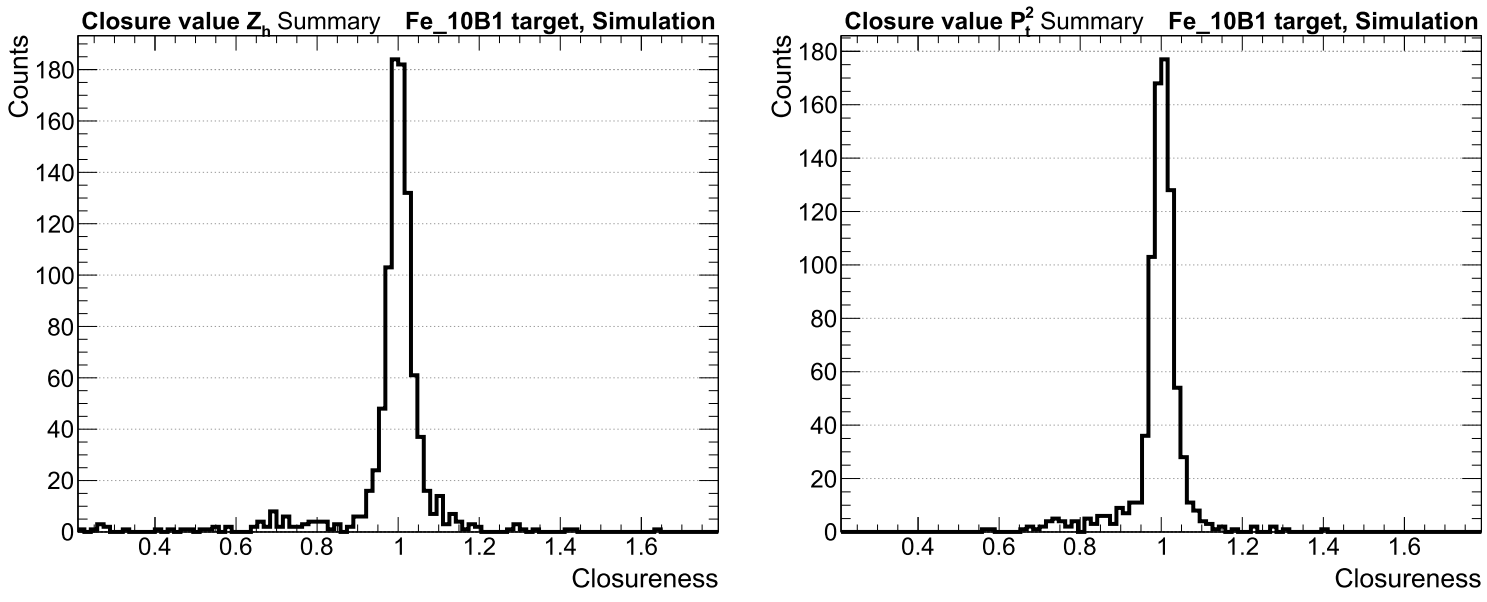

Figure 7.5: Summary of the values of closure of our acceptance calculation. The values are obtained from a 3-dimensional binning of Q^2 and ν, plus Z_h (left) or P_t^2 (right).

7.4 Discussion: Correction methods

Even though our approach has presented positive results so far, there are several other methods of correction available. Whether a method is useful or not will depend on the specific characteristics of the simulations and the detector. For example, a detector with low angular coverage will certainly require a careful treatment since the response will be highly biased. Also, limited statistics will make a binned approach hard for fine tuning, since empty spaces in the grid will deteriorate the performance of the correction.

Other methods of correction were found, though the main idea behind their implementation is the same as with acceptance. Among others, we are interested in two: the *unfolding* and *Omnifold*. These methods are closely related to acceptance and could be interpreted as refined evolutions of it.

Unfolding, also known as 'deconvolution' or 'unsmearing', is implemented in a very similar way to the usual acceptance, requiring to have the information binned and calculating correction factors in the form of the elements of a transformation matrix that acts over a reconstructed event, returning the true values (previous to detector effects). Recent implementations introduce sub-methods that improve the effectiveness of the method in conditions of high bin migration by making use of elaborate deconvolution algorithms. A limitation of this method is the dimensionality since the procedure is feasible only at low dimensions (two-dimensional bins is the usual selection). High dimensions could be implemented but the algorithms are not optimized for it and the computation time increases unbounded.

A smart approach called *Omnifold* utilizes Machine Learning techniques to bypass the intrinsic limitations of separating information in bins. The idea behind this method is the same as in unfolding, looking for the elements of a matrix that can easily move from true values to reconstructed, and vice versa. This is a hard task from a discrete point of view for the reasons discussed in Section 7.2 due to unavoidable approximations and distribution smearing coming from these 'arbitrary' separations. Nevertheless, this implementation learns about the distribution of the variables of interest and their relationships in an unbinned basis taking those problems out of the equation. What's more, the

program is optimized to work in a multi-dimensional way, making feasible to study the behaviour of the data in, say, the five-dimensional phase space of a SIDIS process.

As widely known, these algorithms are composed of three stages:

1. Training: A sub-set of information is given to the software to be trained by learning about the distributions of the variables and their dependencies.

2. Testing: To ensure the program is truthful, the correction is tested with the remaining entries that were left outside of the sub-set.

3. Implementation: After making sure the results are correct, the trained software is ready to act over actual data.

Note the similarities of this iterative process with the application of the Closure Test. This is the standard way of making sure a method is fine and self-consistent.

Studies have contrasted the effect of using these different methodologies in reconstruction with successful results pointing towards the advantage of machine learning techniques over traditional methods [26]. This conclusion is not in tension with old results, however, presenting only small improvements in the corrections over three-dimensions studies. The main improvement, then, is the reduction in the statistics necessary to proceed with the correction and the time and space of storage needed.

Despite having these alternative methods available, they work as a 'black box' for the majority of the process making some steps rather obscure and hard to follow, making more difficult the understanding of the process in detail. Future updates on the study with the implementation of these techniques can be performed.

Chapter 8

Results

With a correction method chosen and the acceptance factors calculated, we can proceed with the analysis. From the discussion at the beginning of Chapter 3, we expect the corrected data to follow a distribution with the form $A + B\cos\phi + C\cos 2\phi$ for our unpolarized data. This function will be used as the model for the fit.

Although the corrections should behave well where the Closure Test gave good results, we have to develop strategies to treat features that are still present. Tighter cuts in the event selection and other analysis tricks will be introduced. A discussion on their impact in the data and the final results is presented too.

8.1 Correction

The acceptance values previously calculated are stored in five-dimensional histograms using the ROOT class `THnSparse`[1] for ease of access. The acceptance factors are added to the data event by event, choosing the value in correspondence with the kinematics of the event. This correction was named 'direct selection' in Chapter 7 and will be the default selection. An extra quality cut for acceptance is introduced, removing unhealthy factors with a relative error of $\sigma_A/A > 10\%$. The error propagation considers the statistical uncertainties from the data and the acceptance error of Equation 7.3 added in quadrature and without correlations in principle.

The azimuthal distribution from data before and after correction is presented in Figure 8.1 for the same bin. Note how the predominant characteristic of the raw data is

[1] This class provides an easy way to handle high-dimensional histograms very efficiently.

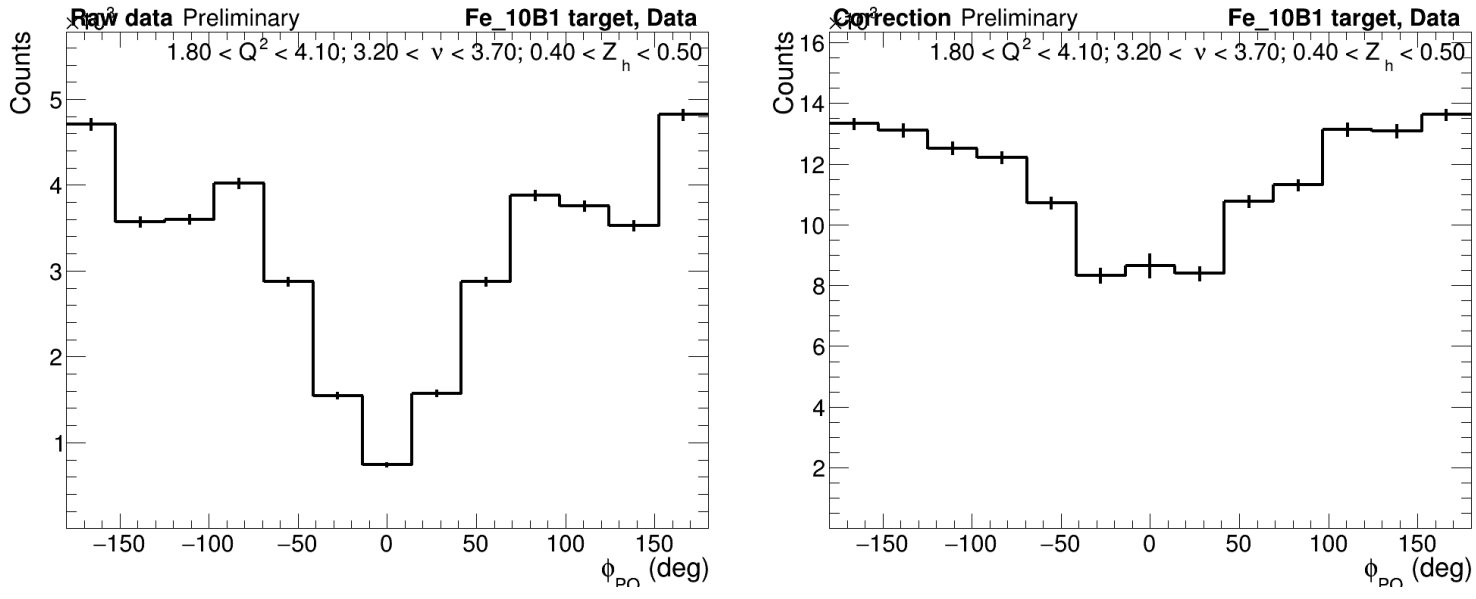

Figure 8.1: Raw data (left) and acceptance corrected data (right) for a three dimensional bin in Q^2, ν, and Z_h (P_t^2 integrated).

the set of bumps at a constant rate. The position of the peaks is distributed at regular intervals of around $60°$ from each other. This structure resembles the six-sector distribution defined by the CLAS geometry. The resultant correction gets rid of these issues in some portions of the distribution. Nevertheless, a part of the bins preserve some of the structures, specially around $\phi_{PQ} \approx 0°$ and $\approx \pm 90°$ to a lesser extent.

Though the peaks could be attributed to imperfections in the correction process, the central peak has been spotted in other contexts, see Section 7.1. An anomalous highly populated region is found at the center of the ϕ_{PQ} distribution in data. This behaviour is barely reproduced in simulations with a small peak at the center. The null correction factors presented in Figure 7.2 supports the non-existence of a large number of entries in this region. Moreover, this lack of factors increases the problem by leaving this region not corrected or with a less reliable correction. More on this subject will be developed in the next section of the chapter.

Due to limitations in the statistics available, a full five-dimensional analysis is not feasible. The integration of Z_h or P_t^2 increases the counts at the cost of biasing the sample and hiding dependencies. Both options will be studied in parallel so that their individual effect in the results can be contrasted. As an example for checking the differences between both approaches, the same bin in Q^2 and ν is presented in Figure 8.2.

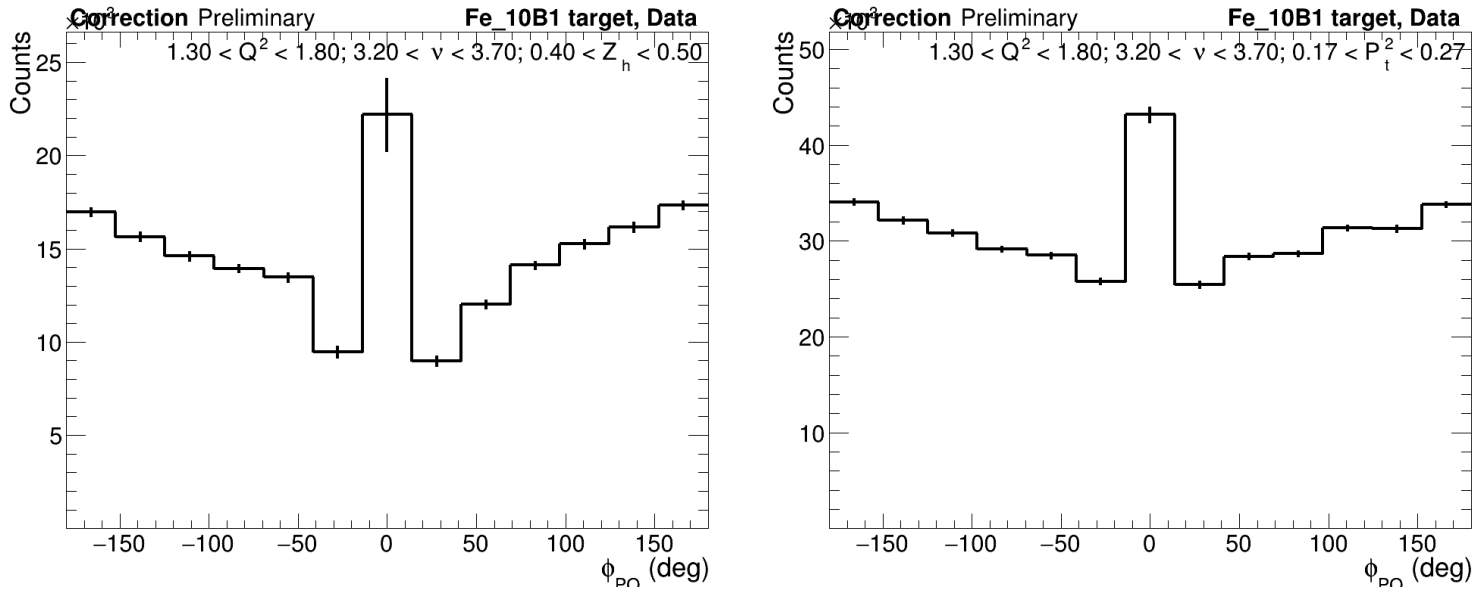

Figure 8.2: Corrected ϕ_{PQ} distribution for a three dimensional bin in Q^2, ν, and Z_h (left) or P_t^2 (right). The remaining hadronic variable is integrated out.

8.2 Fit and quality

The resulting distributions were all fitted with the expression $A + B\cos\phi + C\cos 2\phi$ introduced in Chapter 3. We perform the fit using the `TMinuit` algorithm implemented in the ROOT's method `Fit`. This algorithm presents some changes with respect to the default, giving equal or better results with an optimized method of minimization. The output of the function provides the covariance and correlation matrices associated with the parameters.

A brief disclaimer on the notation. It's an abuse of notation to represent the asymmetry factors in the same form independent of the integrated quantities. For instance, the five-dimensional cross section of Equation 3.17 will lead to a concrete definition for the parameters A, B, and C. However, under certain circumstances we will work with one or more integrated variables, say,

$$\frac{d^3\sigma}{dQ^2 d\nu dZ_h} = \tilde{A} + \tilde{B}\cos\phi + \tilde{C}\cos 2\phi. \tag{8.1}$$

In this case, the factor are not the same as before and are related by

$$\tilde{B} = \tilde{B}\left(Q^2, \nu, Z_h\right) \equiv \int B\left(Q^2, \nu, Z_h, P_t^2\right) dP_t^2. \tag{8.2}$$

For simplicity we will avoid the introduction of a different symbol for each integration and will use the same symbol regardless of the dependencies. The context will make its interpretation clear.

A critical issue regards the central peak aforementioned. Since the distribution is centered at $\phi_{PQ} = 0°$, the fit gets highly impacted by its presence. Some strategies were developed to bypass this complication at fitting time:

- ◇ Full range fit: The fit uses the full range, including the peak. This could be used as a reference to check the real impact the peak has on the results.
- ◇ Left and right ends independently (LR): We proceed by skipping the middle region of the distribution and make two independent fits.
- ◇ Fold and mix both ends (Fold): An implicit assumption is made by expecting a fully symmetric distribution. The number of entries in each bin is roughly doubled.
- ◇ Shift distribution: The distribution is shifted and centered around $180°$. A single fit is performed with the end tails cut.

Each strategy has its own advantages. The LR method gives us a direct measure of the symmetry around $0°$ of the azimuthal distribution. The Fold method increases the entries in each bin, roughly doubled, at the expense of making the resulting mix particularly sensitive to asymmetries between both sides. The Shift method doubles the number of degrees of freedom available for the fit, hence making the fit more accurate.

Since the number of events per target is not the same, we will work with a normalized version of the parameters. This approach makes the comparison between different targets more direct. Instead of using the B and C parameters of Equation 3.17 as a measure of the modulations, we will present results in terms of B/A and C/A. These quantities also reduce the dependency of the results on the experiment's luminosity by cancelling out the factor coming from the formal cross section expression. It is important to consider the full formula of error propagation in this scenario, where correlation factors get values of around 0.2 and their effect is not negligible.

Remember that the setup is arranged so that a deuterium target is placed aligned with the solid target. To reduce systematic effects on treating the deuterium data, we will separate the set by their solid partner, labelling the sub-sets as DC, DFe, and DPb. Any ratio that compares liquid and solid targets will use their respective partner's information.

Previous studies on the subject have presented results on deuterium asymmetries with

different notation. Though the distributions should follow the same trend, the introduction of certain factors needs to be carefully considered in order to quantify the effects correctly. The relation between the notation found in the bibliography and the parameters defined in this work is

$$A_{\cos\phi}^{UU} \equiv \frac{B}{A}, \qquad A_{\cos 2\phi}^{UU} \equiv \frac{C}{A}, \qquad \langle \cos\phi \rangle_{eX} \equiv \frac{B}{2A}, \qquad \langle \cos 2\phi \rangle_{eX} \equiv \frac{C}{2A}, \tag{8.3}$$

where the two first terms explicitly show the function of ϕ associated and a superscript remarking that both incident lepton and target are unpolarized (U). The next two terms introduce an extra factor of 2 coming from the integration in ϕ to get the average or 'expectation value'. Note the subscript where e represents the electron and X the target nuclei. Due to ease of reading the second definition will be used for the rest of the text. In this notation X will be A when dealing with solid targets and D for deuterium. The 2 factor in the denominator is applied in the summary plots. Note this decision leaves the ratios unaltered.

8.2.1 First asymmetry term

The normalized factor accompanying the $\cos\phi$ term is regarded as the *first asymmetry*. Previous results have demonstrated a hierarchy in the magnitude of the asymmetry factors. The free term of the cross section, A in Equation 3.17, predominates. The modulation terms present sizes in the order of

$$\mathcal{O}\left(\langle \cos\phi \rangle_{eX}\right) \sim 10^{-1}, \qquad \mathcal{O}\left(\langle \cos 2\phi \rangle_{eX}\right) \sim 10^{-2}, \tag{8.4}$$

making harder to identify high order terms due to statistical issues and the necessity of higher sensitivity in the experiment.

The first asymmetry value is obtained for deuterium and the solid targets with the different techniques described above. The deuterium behaviour of the three batches of data is summarized in Figure 8.3 with the use of the shift method. An acceptance quality cut and the removal of the peak from the fit are also implemented. Note the identical trend in almost the whole kinematic range followed by all three sets, as we would expect

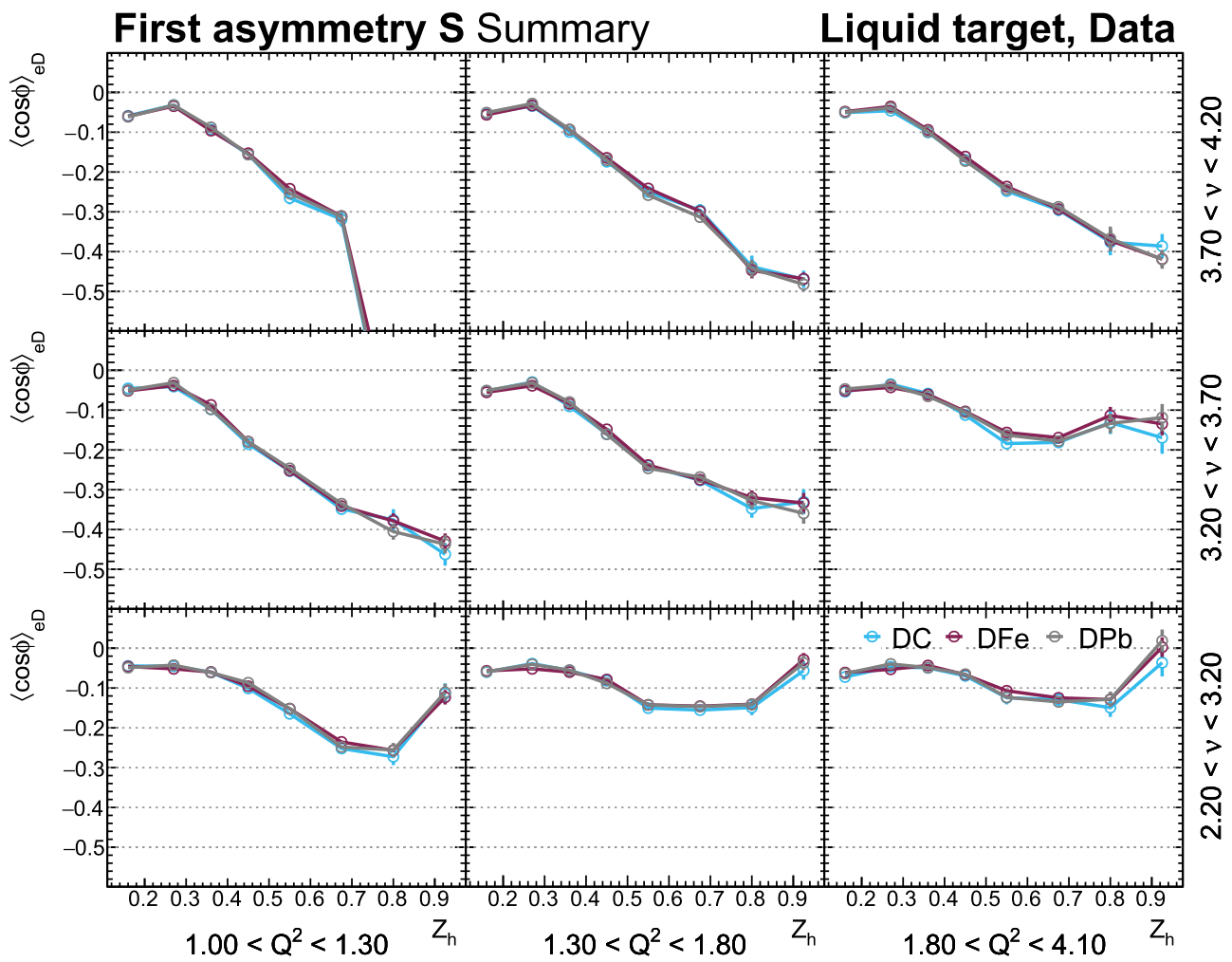

Figure 8.3: First asymmetry parameter of liquid targets in bins of Q^2 and ν as a function of Z_h. The points are separated by the associated solid target.

in absence of external effects. High Z_h has reduced statistics, explaining the worse performance at the edges in some bins. Low Z_h gets a small and uniform asymmetry in all of the bins, though at around $Z_h = 0.3 - 0.4$ an abrupt change in the tendency is followed by a linear enhancement, that tends to be reduced again at higher Z_h. The asymmetry has a very subtle dependence on Q^2, more predominant in energetic pions with high Z_h. A strong dependency in ν is observed, doubling the effect on energetic pions. This result will be revisited in terms of x_b for a more direct interpretation.

In Figure 8.4 the asymmetry of the iron target is extracted with the diverse methods proposed. Apart from the *full* method, the other methods skip the central peak. Even though this last method gets the quality of the fit impacted (high χ^2/ndf), the nominal values are barely affected. The same is observed in the other solid targets. At this point, the first asymmetry of solid targets presents a similar trend as deuterium. Surprisingly, the results are almost independent of the method in general, within uncertainties. The uncorrected *full* method presents the greatest mismatch mainly.

The P_t^2 dependence is studied too, since its response has a fundamental link with the

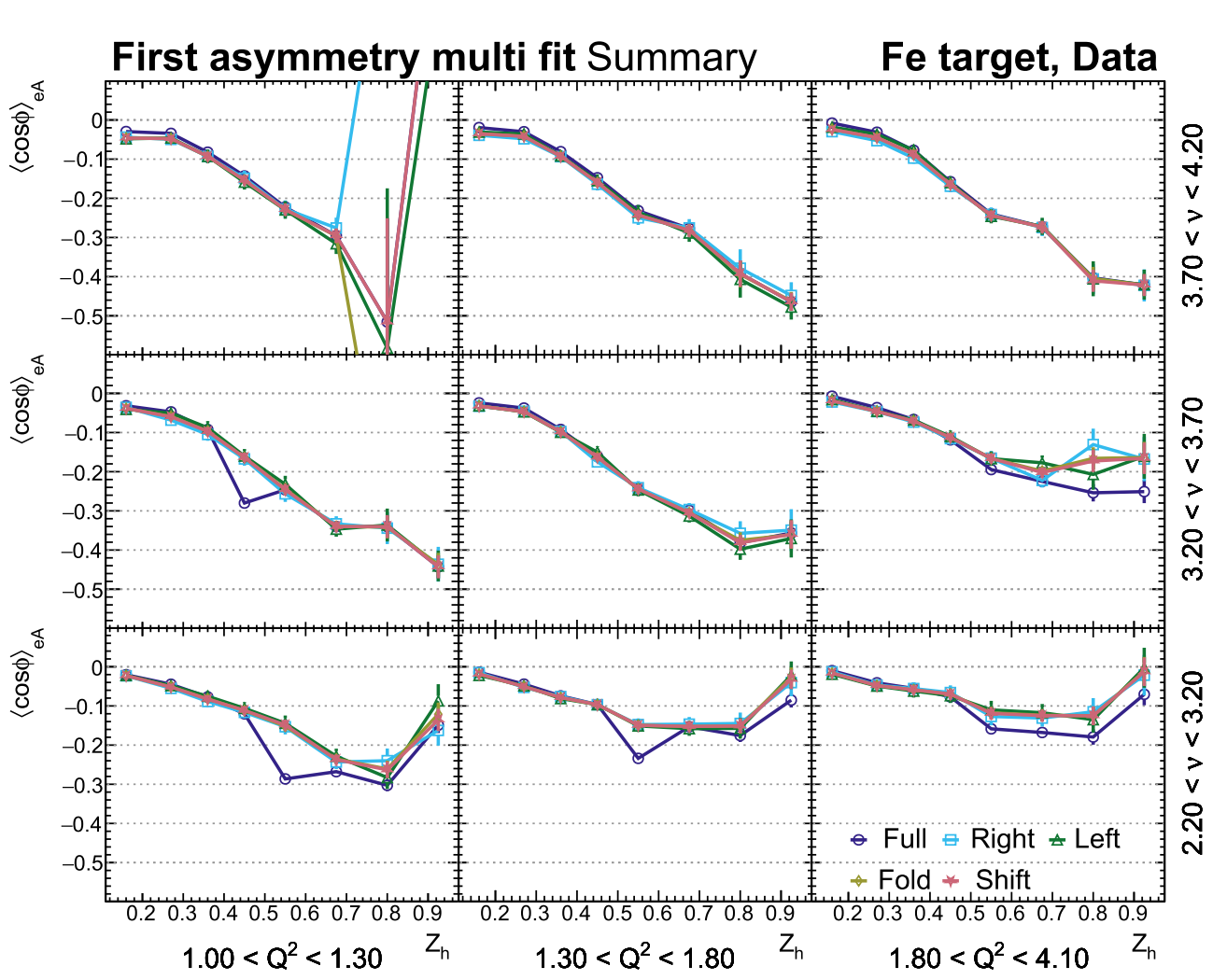

Figure 8.4: First asymmetry parameter from iron target obtained with different techniques in bins of Q^2 and ν as a function of Z_h. The names in the legend reference, from top left to right, the *full* fit, right and left wing of the *LR* method, *fold* method, and shifted distribution.

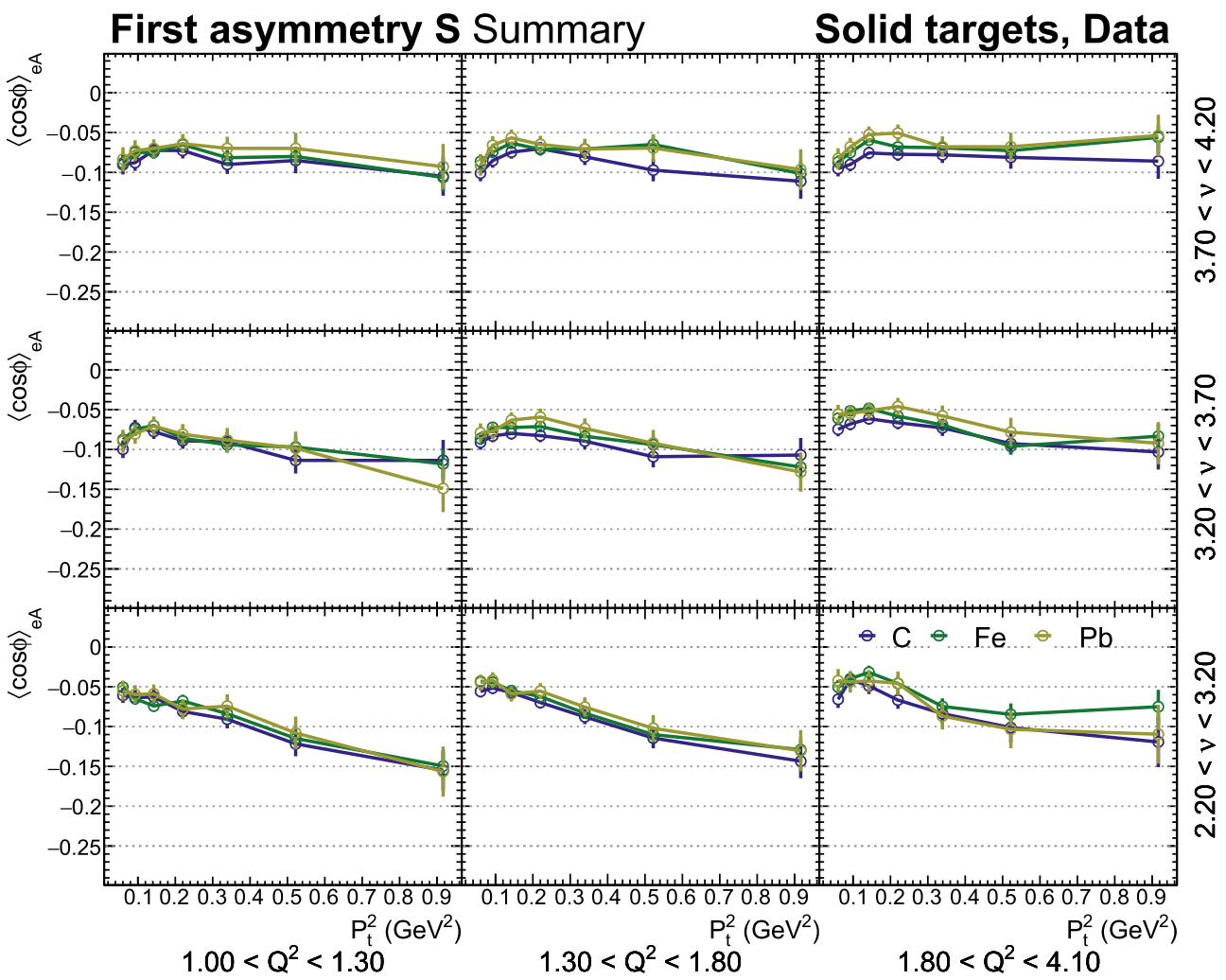

Figure 8.5: First asymmetry parameter for solid targets in bins of Q^2 and ν as a function of P_t^2.

inner dynamics of the quarks and plays a central role in broadening analyses. In Figure 8.5, the results as function of P_t^2 are presented for the solid targets. Note the subtle differences in the tendency along the P_t^2 axis especially at high ν. Numerically, we see a small increment of the asymmetry that gets doubled at most in some regions of low ν. There is no clear Q^2 dependency. An almost constant value of around -0.1 is obtained along the different bins. This uniformity is more evident in the whole range as ν increases. Recalling the results of Z_h dependence, we observe the opposite response, this is, the asymmetry is emphasized at low ν instead of at high values.

In general, theoretical derivations prefer x_b as second leptonic variable due to its direct interpretation as the momentum fraction of the struck parton. We reproduced the same results as before with x_b instead of ν. Recalling the relation between these variables (in the Lab frame)

$$x_b \equiv \frac{Q^2}{2M\nu}, \tag{8.5}$$

we expect a similar response, following an inverse trend with respect to ν and with cer-

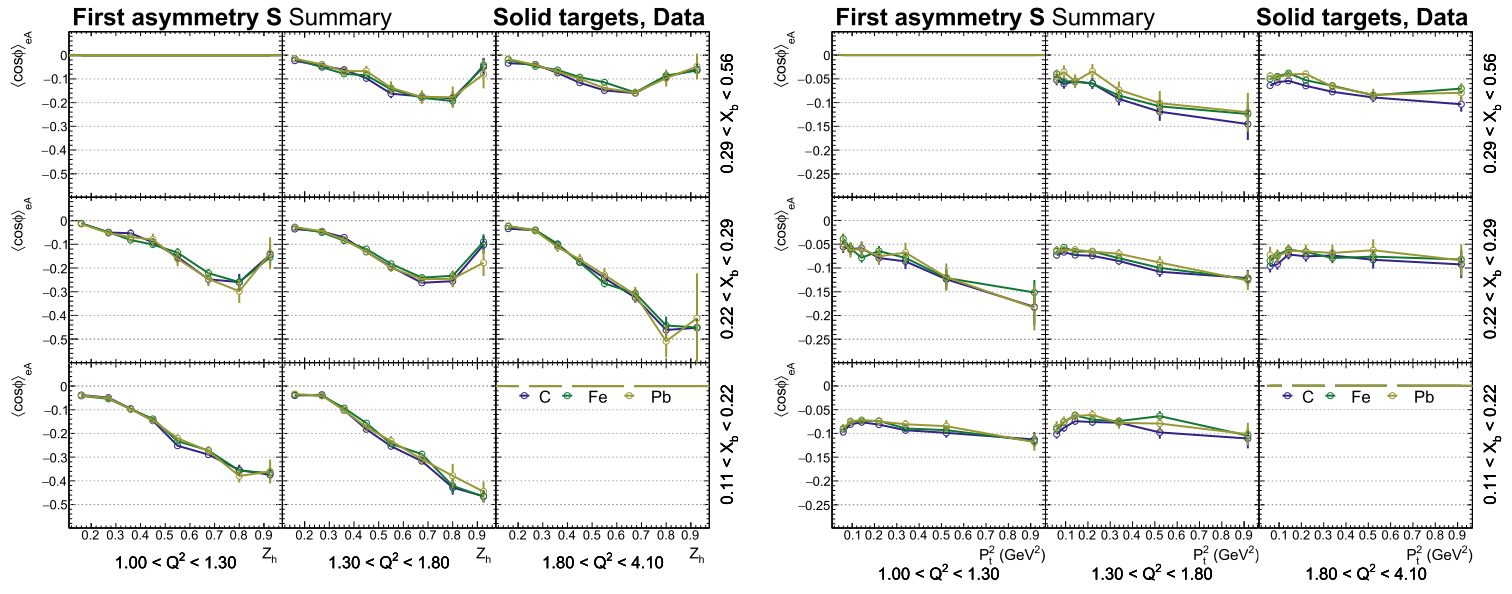

Figure 8.6: First asymmetry parameter for solid targets in bins of Q^2 and x_b as a function of Z_h (left) and P_t^2 (right). Two bins are empty due to lack of statistics in those regions.

tain modulations given by the Q^2 term. The results are presented in Figure 8.6. No significant qualitative nor quantitative difference is found.

In general terms we found the first asymmetry to be consistently negative independent of the phase space region and if it's function of Z_h or P_t^2. This claim is in line with some theoretical derivations (see Equations 4.4 and 4.20 in [6]) where the term is explicitly negative by construction. Moreover, deuterium results are in agreement with previous experimental measurements developed by the *COMPASS* [27, 28], *ZEUS* [29, 30], and *HERMES* [31, 32] collaborations.

The ratio of solid over liquid target's first asymmetry is presented in Figure 8.7. A clear trend is followed as function of Z_h for all of the samples. Low energy pions see a reduction of at least a 20% in this first parameter. These pions cannot have a big momentum so, though integrated, these events are composed of small P_t mainly. This could indicate an accentuation of the asymmetry for solid targets due to the contribution of events from the Target Fragmentation Region (TFR), given the apparent low contribution of the quark intrinsic transverse momentum, following Equation 3.11 (this idea will be revisited later). A remarkable enhancement in the asymmetry is found at around $Z_h = 0.3 - 0.4$. Middle range values present no visible effect of nuclear media, with uncertainties that tend to leave the ratio close to 1. No conclusive reaction is seen at high hadrons's fractional energy.

A more uniform tendency is found when the P_t^2 dependence is studied. All of the bins

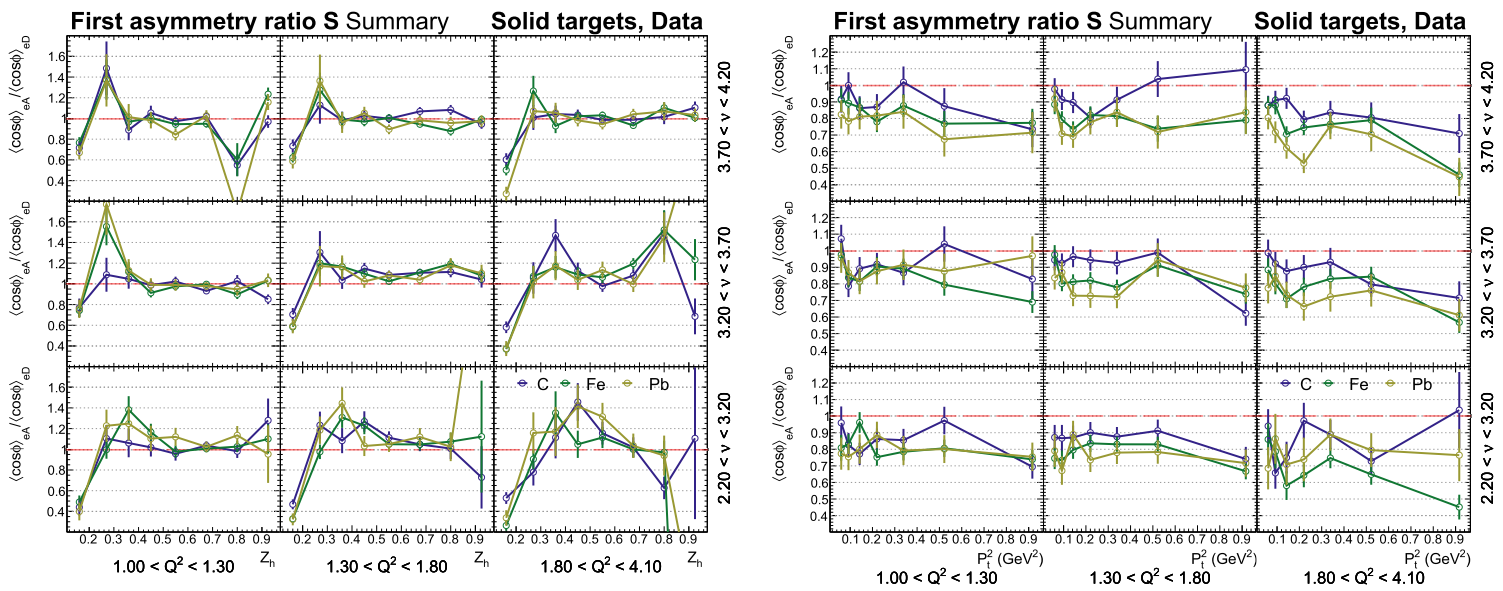

Figure 8.7: Ratio of the first asymmetry parameter (solid over liquid target). The distributions are presented as a function of Z_h (left) and P_t^2 (right). A red-dashed line marks the ratio value 1 as a reference, meaning no nuclear effects.

show a reduction in the asymmetry from a few $\%$ to 30%. Those points that are closer to unity have significant error bars. A nuclear size dependence is present at middle range values. Larger nuclei such as lead present the higher reductions of around 20% in average in contrast to carbon, the smallest of the samples, with 10% at most. The distributions seem to start at 1 for zero momentum and get a reduction in this low P_t^2 section. The whole range presents a very uniform behaviour until $P_t^2 \approx 0.5\,\mathrm{GeV}^2$,where a small bump closer to 1 is visible in some bins. This feature is not as clear as in other distributions so its presence is anecdotal. After this point we observe a further decrease in the limits of P_t^2, where statistics begin to drop thus increasing uncertainties.

8.2.2 Higher order asymmetries

The third parameter will be called the *second asymmetry* and will be the highest order term we can access with the experiment's sensitivity. Figure 8.8 presents the second asymmetry for the same Q^2 and ν bins as before. Unlike the last case, this asymmetry gets values close to zero with big uncertainties at the edges. The scale is reduced by half with respect to Figure 8.4, stressing the smaller contribution of these terms.

As a function of Z_h, the modulation acquires mainly negative values. The trend dependence on Q^2 and ν is unlike the first asymmetry. Here we can see a stronger dependence on Q^2, that's more evident at middle values of ν. The effects in asymmetry are rather small, with an average of 5%. The P_t^2 dependence shows an even smaller effect.

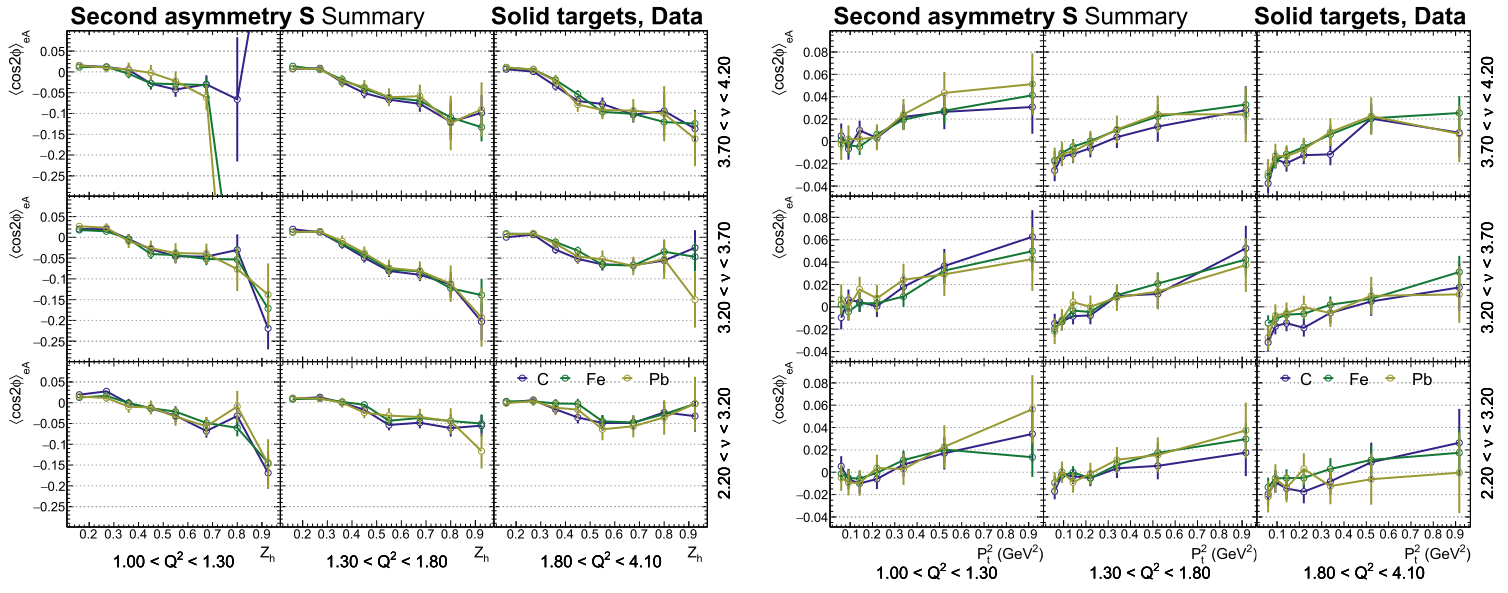

Figure 8.8: Higher order asymmetry parameter from solid target. As a function of Z_h (left) and P_t^2 (right).

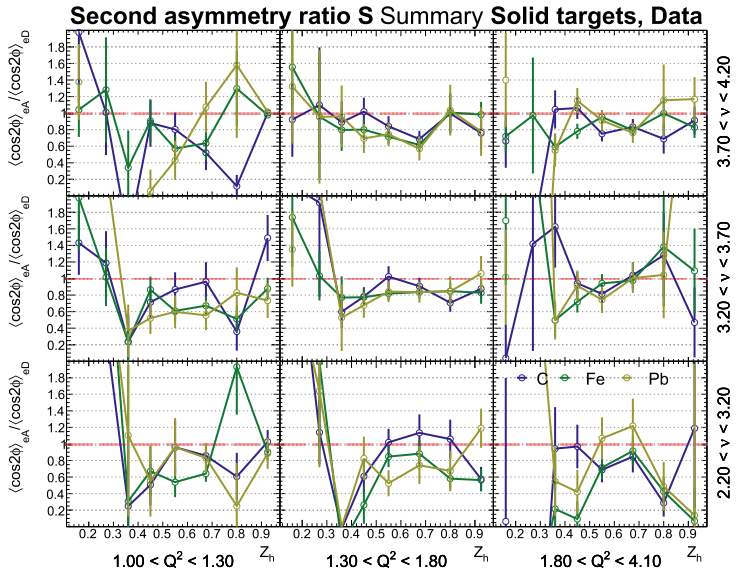

Figure 8.9: Ratio of the second asymmetry parameter (solid over liquid target). The distributions are presented as a function of Z_h (left) and P_t^2 (right). A red-dashed line marks the ratio value 1 as a reference, meaning no nuclear effects.

Some values cannot be regarded as positive nor negative given the dominant error bars at low momentum. However, at values higher than $P_t^2 \approx 0.3\,\mathrm{GeV}^2$ positive numbers are predominant. These effects are similar for all solid targets and reach values of a few $\%$.

The ratios found for this parameter are summarized in Figure 8.9 with results not as conclusive as with the previous one. Reductions in the order of $20 - 40\%$ are observed in central values. Suppression and enhancement as high as 80% can be found, especially at edges values (low and high Z_h). Enormous error bars and no clear trend hinder a clear conclusion.

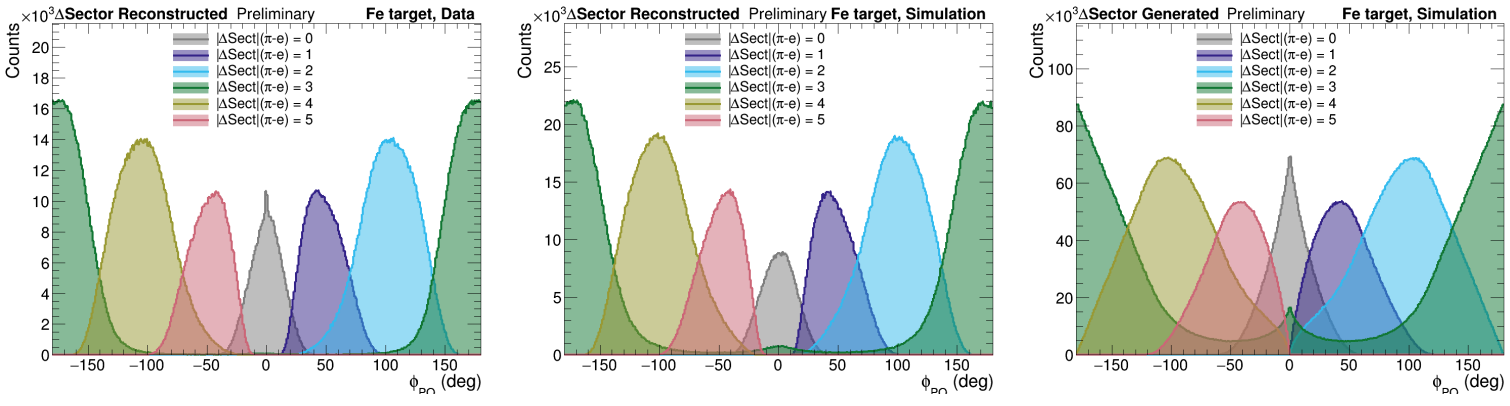

Figure 8.10: Raw data (left), reconstructed simulation (center), and generated simulation (right) distributions with ΔSector detail for iron target.

8.3 Sector dependency

Previously, we stated that the different structures found in 8.1 resemble the detector's sector distribution. We inspected some possible sources of the peaks by different means in order to refine our selection and reduce the big modulations observed, specially the central peak.

The definition of our variable of interest ϕ_{PQ} requires the detection of an electron and a pion. Since in principle this doesn't depend explicitly on the individual sector each particle interacted with, we use their difference instead. The distributions of data and simulation with the sector difference detail are presented in Figure 8.10. It's clear how each of the peaks present in raw data is connected to a sector difference as we conjectured. To predict this relation is not trivial since the ϕ_{PQ} variable is not defined in terms of the beam direction, but the virtual photon's direction. Additionally, note that the central peak issue is coming almost entirely from events that present both particles in the same sector. These central events are also present at generation level, but with large contributions from the other sectors. The detector effect reduces these contributions and produces an almost one-to-one relation of the peaks with ΔSect that's visible in reconstructed simulation and data. Note also the presence of a second smaller contribution from events in opposite sectors at $\phi_{PQ} \approx 0°$ in simulation that is highly suppressed in data.

The intensification of events at the center could be produced by sources of different nature. Contamination from sub leading scattered events, detector defects that haven't been solved with the acceptance, low quality in some measurements, or even offline re-

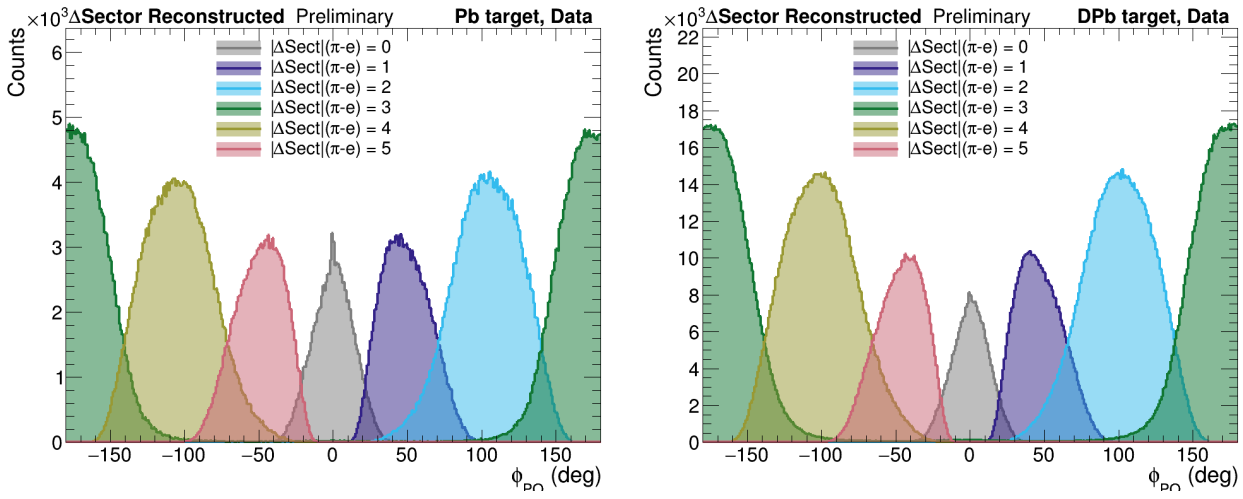

Figure 8.11: Reconstructed distribution for solid lead target (left) and liquid deuterium target associated (right). Note the similarities in the majority of peaks and the increment in the central one for the solid target.

construction issues are among the possibilities. A quick view of the solid and liquid response for the same data set is presented in Figure 8.11. This hints at some nuclear dependence of the central events. Moreover, this increment is clearer in bigger nuclei such as iron and lead, and is still present but in a minor amount with carbon.

Some extra cuts have been tested to reduce the presence of these events. An explanation of them and their impact in the parameters' results will be presented in the next subsections.

8.3.1 No same sector events

As a first approach to the problem, an extreme case will be studied. Since the central peak has been demonstrated to be produced mostly by same sector events, we will test the effect of removing this situation entirely. Regardless of the huge enhancement observed in the center, ideally we don't want to remove the whole structure since the modulations expect its presence. This procedure completely eliminates these events 'by hand' so its effect should be regarded as a limit case, setting boundaries for the contribution of the peak in the final results.

Looking at the effect in Figure 8.12, we note a clear effect on the ratios. The Z_h dependence plots are the same for values of $Z_h > 0.3$. A suppression of the effects found in the free-cut results for lower values is appreciated. The reduction of asymmetry at the low edge is no more and the peak spotted in the middle region was diminished, though it is still present.

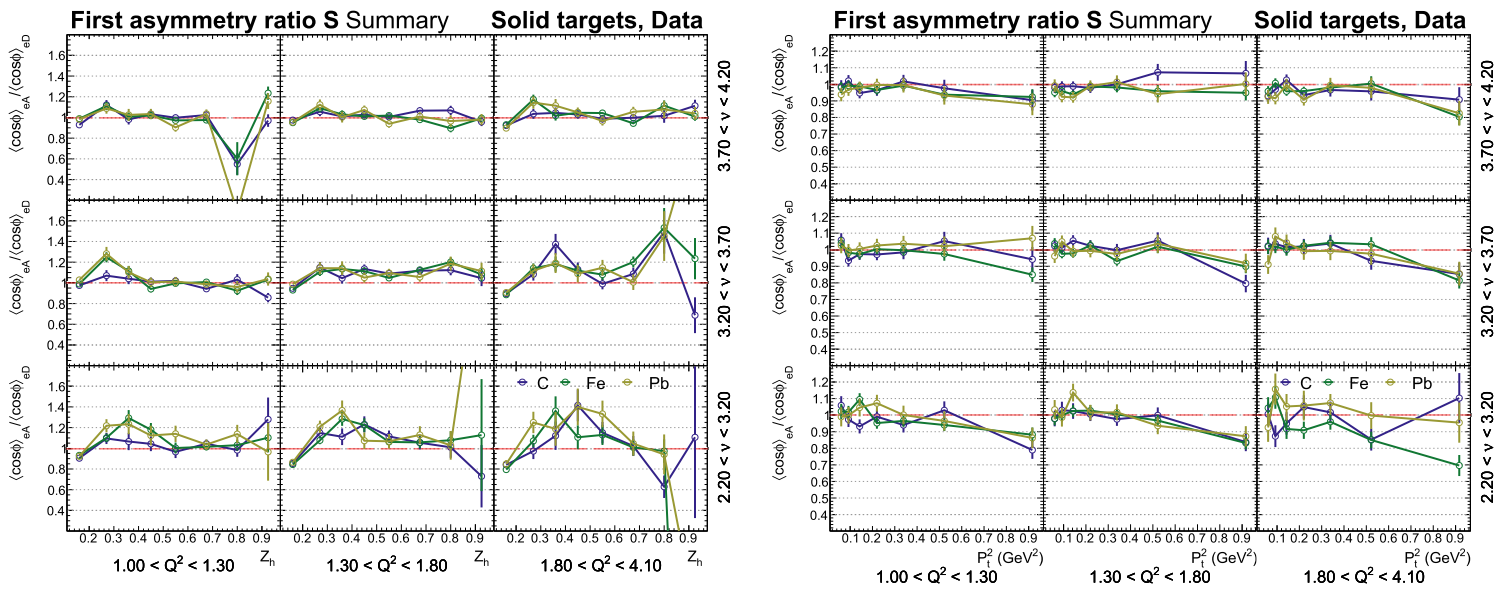

Figure 8.12: Ratio of the first asymmetry parameter (solid over liquid target) with a hard cut removing events with π^+ and e^- in the same sector. The distributions are presented as a function of Z_h (left) and P_t^2 (right). A red-dashed line marks the ratio value 1 as a reference, meaning no nuclear effects.

The same effect is reproduced in the P_t^2 dependency, though its impact is even stronger. A full suppression of the tendency is observed systematically through all of the bins. No nuclear effect at all is found. The nuclear hierarchy is no more visible, presenting a critical limitation for the study.

We can hypothesize a high contribution to the first asymmetry coming from the low transverse momentum events. This is in line with the models that predict the Cahn effect as the major contributor to this term.

8.3.2 Current and Target fragmentation region

The *Current* and *Target fragmentation regions* (CFR and TFR) were introduced in Chapter 3. The determination of the interaction's region is relevant for some studies on direct measure of structure functions and was studied in previous analyses of our team. One way of measuring the origin of the hadronization process is by inspecting the Feynman-X variable associated to the hadron, defined as:

$$X_f \equiv \left. \frac{P_L}{P_L^{\max}} \right|_{CM}, \tag{8.6}$$

where both P_L terms are the longitudinal component of the final hadron's momentum in the center of mass frame.

By definition, this quantity depends on the frame of reference (i.e. it's not an invari-

ant quantity) and is bounded by -1 and 1. Depending on the kinematic region of the experiment a certain range of X_f could characterize an interaction region. However, this differentiation is not definitive and overlaps of both main regions are expected. A crude approach is done by requiring $X_f > 0$ for *CFR* and $X_f < 0$ for *TFR*.

The study was also developed in terms of the (pseudo-) rapidity variable y that is commonly used in higher energy physics experiments, as mentioned in Section 3.4. Though this quantity is semi-invariant[2] and its implementation could be less complex, its definition is less accurate depending on the kinematics, this is, depending on the energy of the process the pseudo-rapidity and rapidity variables differ. This is not likely to happen in high energy colliders but might introduce problems in its interpretation at our energy levels. A one-to-one relation between y and X_f has been found, however, making both approaches equivalent.

The impact of these cuts in the first asymmetry term is shown in Figures 8.13 and 8.14. Though there is a detriment in the shape of some distribution attributable to the reduction of around half of the total statistics available for each fragmentation region, a trend is found especially when compared to the full response of Figure 8.7. Beginning with the Z_h dependence, the TFR events are predominantly at low values leaving empty spaces at high Z_h. On the other hand, the CFR events are distributed along all the space and with a shape that resembles the original one. Although the initial suppression at small Z_h is not visible, the following enhancement peak of $40 - 60\%$ is still present. This initial feature at low Z_h is then attributable to TFR events, and the peak to CFR ones.

A remarkable difference in the behaviour is found in the dependency with P_t^2. The presence of significant error bars complicates the quantitative study of the result in some zones. However, a qualitative description indicates an increase of asymmetry or null effect at middle range values followed by a suppression at high P_t^2 for CFR events. Also, the overall suppression stated in Figure 8.7 is suggested to be produced by TFR events, given the accentuated decrease of more than 30% in almost all of the bins. The sum of both contributions is presumed to be dependent on the nuclear size.

[2]This is not standard terminology but it references to the peculiar behaviour of Δy which turns out to be invariant.

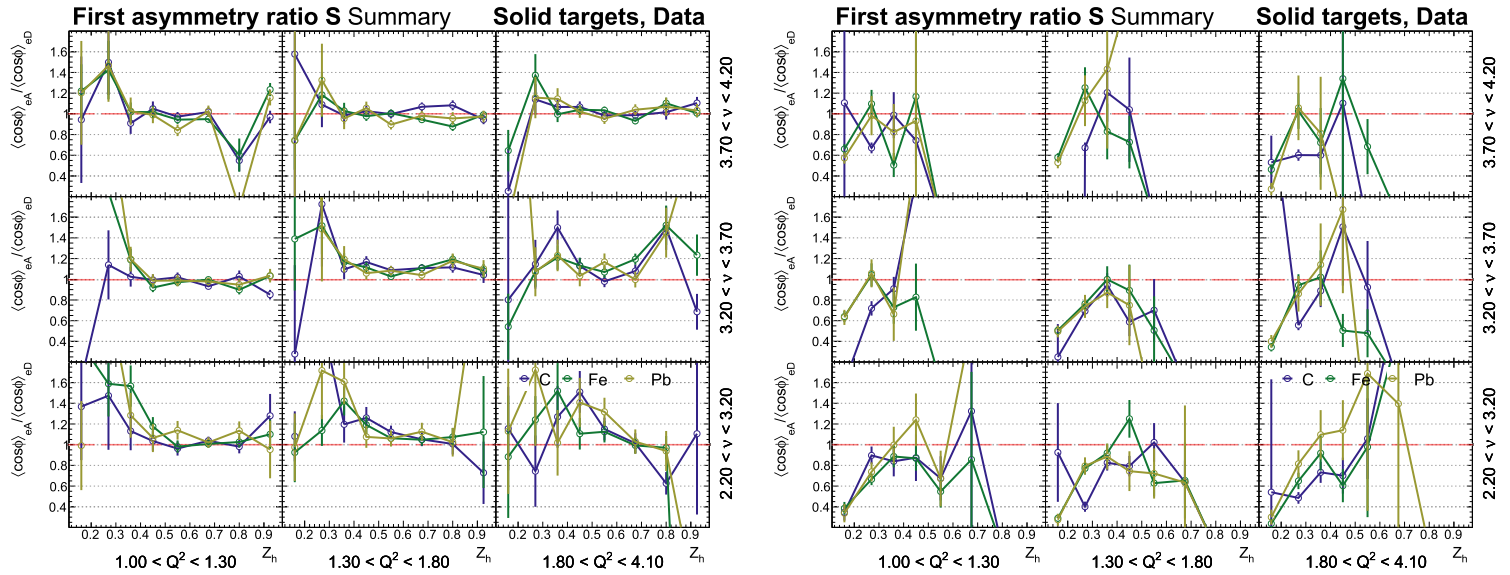

Figure 8.13: Ratio of the first asymmetry parameter (solid over liquid target) as a function of Z_h for events from the Current ($X_f > 0$, left) and Target ($X_f < 0$, right) Fragmentation Regions. A red-dashed line marks the ratio value 1 as a reference, meaning no nuclear effects.

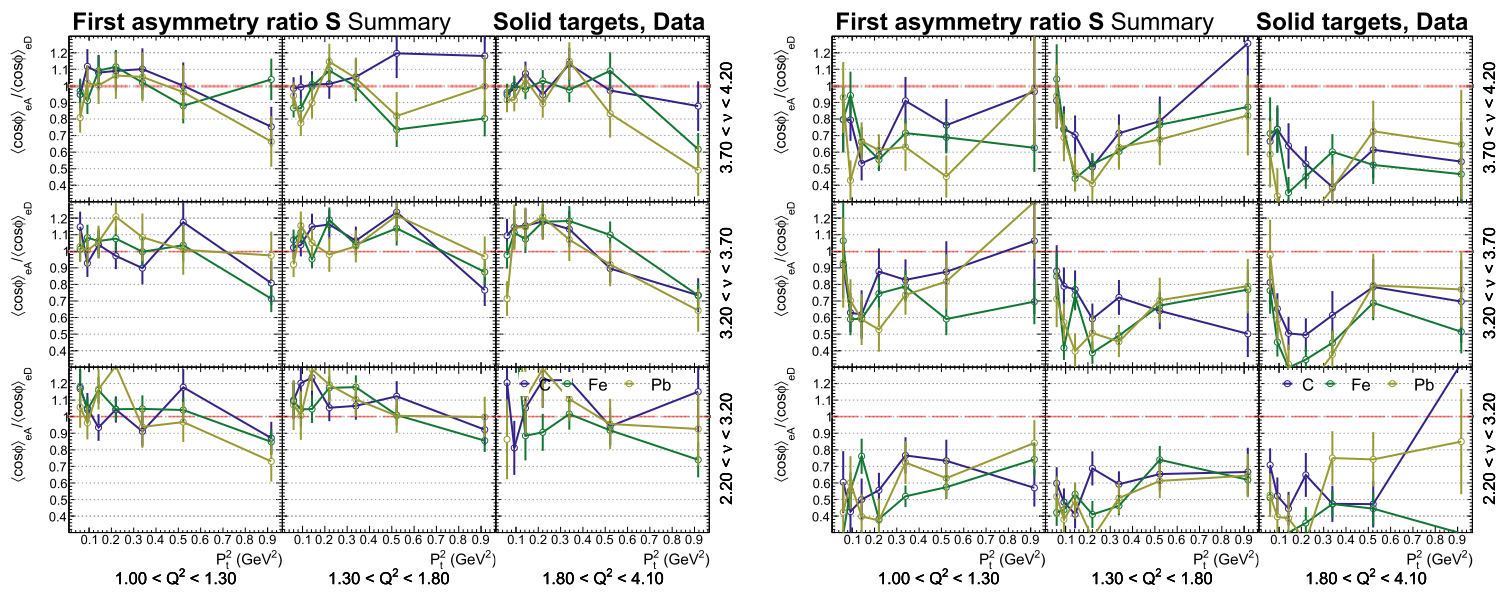

Figure 8.14: Ratio of the first asymmetry parameter (solid over liquid target) as a function of P_t^2 for events from the Current ($X_f > 0$, left) and Target ($X_f < 0$, right) Fragmentation Regions. A red-dashed line marks the ratio value 1 as a reference, meaning no nuclear effects.

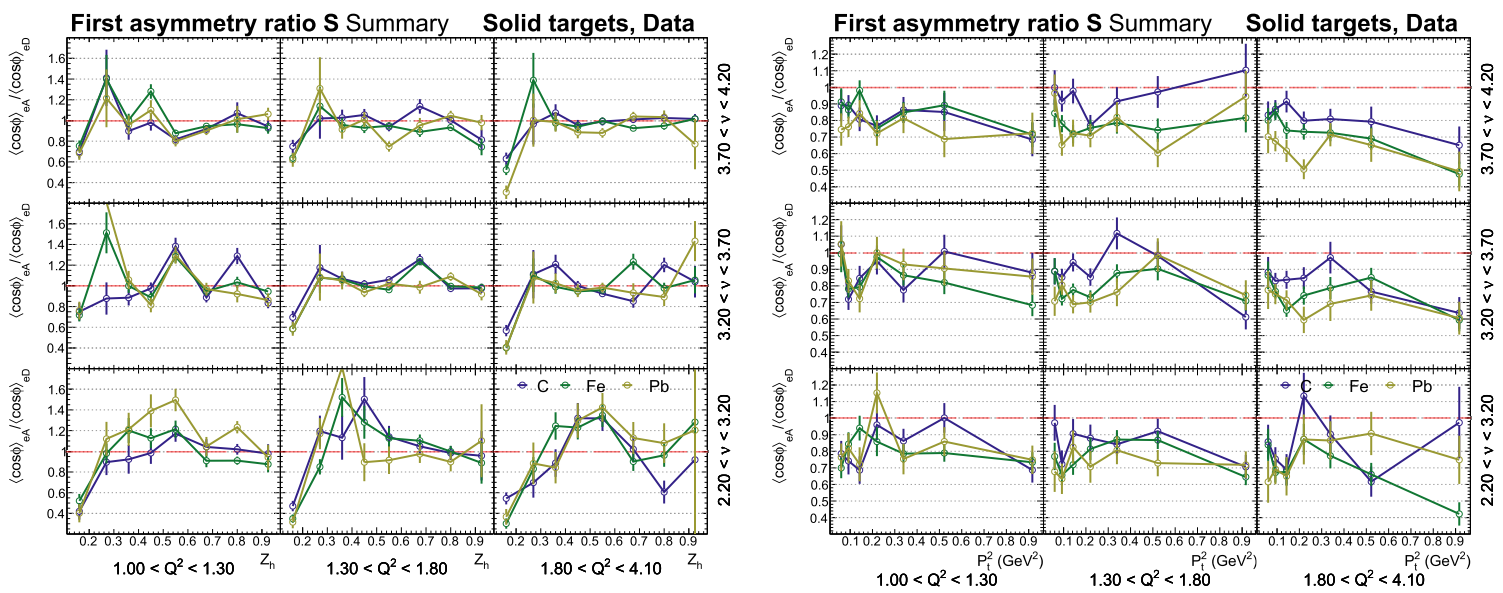

Figure 8.15: Ratio of the first asymmetry parameter (solid over liquid target) using π^+ DC fiducial cuts. The distributions are presented as function of Z_h (left) and P_t^2 (right). A red-dashed line marks the ratio value 1 as a reference, meaning no nuclear effects.

8.3.3 Pion fiducial cuts

Electron's fiducial cuts in DC were introduced in Section 5.2.1. A similar study led to an optimization of parameters to remove the edges of the DCs specifically for π^+ detection. The values were reported in [23]. Though this cut was available in the GetSimpleTuple software, it was not implemented as a default cut selection.

The impact of this cut in the asymmetries is shown in Figure 8.15. Although some points have been displaced, error bars got enlarged and the general tendency is still followed, so no major differences are found in the Z_h part. Likewise, the suggestive trend on P_t^2 keeps showing hints of a nuclear dependency. However, overall it is less conclusive due to the higher fluctuations.

This cut in π^+ has a negligible effect in statistics as was pointed out in previous analyses. Consequently, the ratios were barely changed. This dismisses one of the possible solutions postulated in [1].

8.3.4 Mirror matching

Spots of contamination in the CCs were found at low momentum zones for pions with $P < 2.7\,\mathrm{GeV}$. This topic has been discussed and demonstrated to have a low impact on other observed quantities. A cut of quality was introduced in analyses for electrons [33] and neutral pions [19] to get rid of these concerning elements. A similar decision was

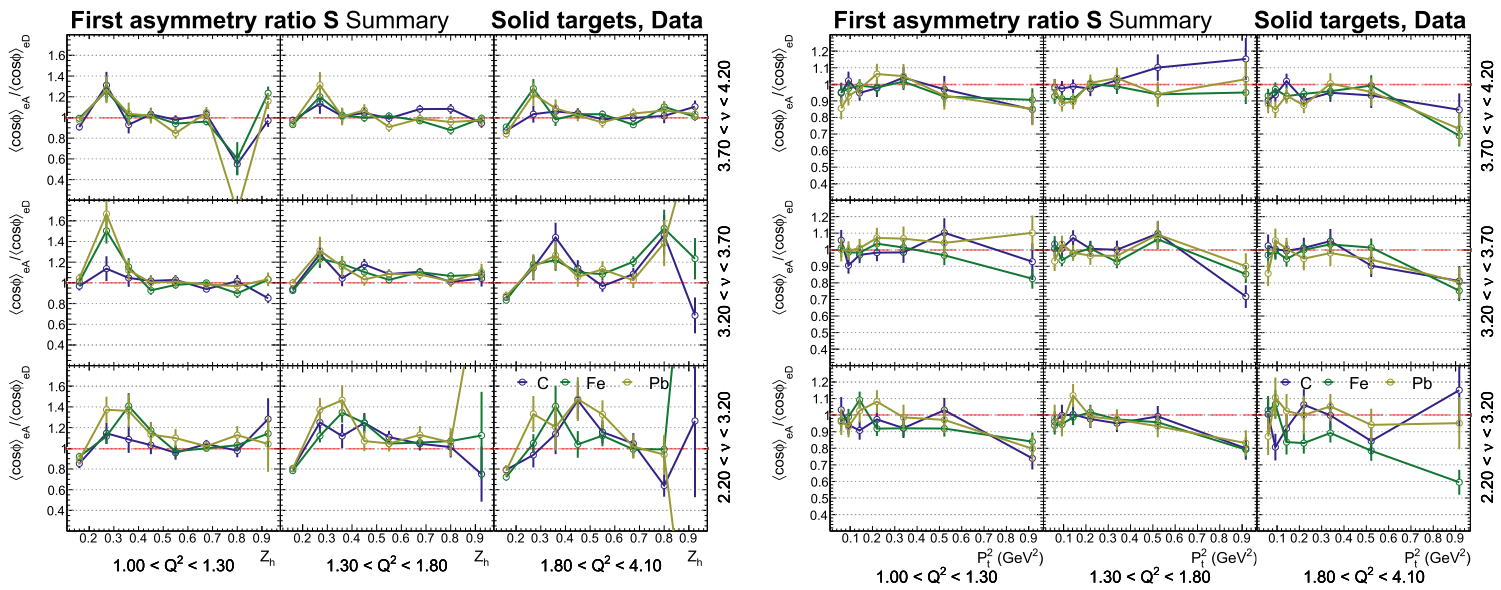

Figure 8.16: Ratio of the first asymmetry parameter (solid over liquid target) using an equivalent cut to the Mirror Matching technique. The distributions are presented as a function of Z_h (left) and P_t^2 (right). A red-dashed line marks the ratio value 1 as a reference, meaning no nuclear effects.

taken in our study in Section 5.2 where the CC signal selection restricts the number of photo-electrons generated by the electron's interactions to be significant enough. Nonetheless, charged pions still present unexpected high signals at this kinematic region as it was previously reported in [1].

The Mirror Matching (MM) is a technique that uses the signal recorded in the CC and makes it to coincide spatially with the TOF signal and other layers of detectors. This task is not easy since no angular information was recorded in the original *BOS*. A refined tuning of the angles removed an anomalous peak spotted at a region with great amount of photo-electrons. In order to produce a close effect, a cut with a similar impact was performed. Only π^+ candidates with a signal of $N_{phe} < 25$ at low momentum will be accepted.

The results presented in Figure 8.16 show a strong suppression of the nuclear effects. First, the initial Z_h enhancement in the second bin is still present but weaker at high ν. On the other hand, the P_t^2 part shows a full inhibition of the nuclear effects reported in the no-cut scenario.

Chapter 9

Conclusions

We analyse the distribution of π^+ generated in SIDIS processes with the electron beam of $5.044\,\mathrm{GeV}$ in the CLAS detector at Hall B of Jefferson Lab. A series of solid targets made of *C*, *Fe*, and *Pb*, and a liquid *D* target were designed to test the effect of different nuclear sizes in hadronization processes with special interest in the distribution around the virtual photon direction, defined as the azimuthal coordinate.

We use a set of Monte Carlo simulations generated with Pythia to get an estimation of the detector response and correct the data from inefficiencies. This last was done by means of a five-dimensional acceptance in order to reduce the model dependency of the correction. Additionally, we introduce a method of control of the acceptance's quality called 'Closure Test' that applies as a self consistent quality check over a three-dimensional binning. The level of closure is slightly deviated from 1, the ideal value, and gets different results for the dependency on Z_h and P_t^2, with an overall performance of 0.98 ± 0.12 and 0.99 ± 0.07, respectively.

The azimuthal asymmetries calculated have a well behaved trend, followed by all of the solid targets and deuterium sub samples. General results are in line with previous measurements carried out by collaborations that work at much more energetic kinematic regions such as *COMPASS* [27, 28], *ZEUS* [29, 30], and *HERMES* [31, 32].

A systematic reduction of the modulations in heavy nuclei was observed as a function of P_t^2, with hints of a nuclear size hierarchy. As a function of Z_h a predominant enhancement of more than 10% is found in the neighbourhood of $\sim 0.3, 0.4$ values, without a clear nuclear size dependency. No nuclear effects were found at higher values with the

exception of events closer to 1, where low statistics hinder substantial conclusions. Conclusive results on higher order asymmetries were not feasible.

The modulations were demonstrated to be fully dominated by events detected in the same sector. An historical problem in the central region of the ϕ_{PQ} distribution was addressed by the use of several strategies. The study of X_f dependency encodes information of the region of origin of the interaction (CFR or TFR). A systematic accentuation of the first asymmetry term is associated with events produced in the TFR, meanwhile CFR events does not present significant nuclear effects. Further studies will be needed to determine the validity of this claim. Other possibilities of solution such as DC fiducial cuts and hard cuts in the CC signal were dismissed. The action of nuclear media was bounded by studying the limit case of no same-sector events, with a complete removal of hierarchy in nuclear sizes. The actual effect should lie between a reduction of the first asymmetry term of 0% to 30%, at least as a function of P_t^2.

9.1 Outlook

Some future tasks with high impact in the study remain unsolved for now. Among others, in order of importance, we get:

- ◇ Apply a correct Mirror Matching or a similar technique to clean the CC response in a more systematic way.
- ◇ Find alternatives to reduce uncertainties in the asymmetries, in order to extract significant results for the second asymmetry parameter.
- ◇ Extend the study to other hadrons such as π^-, taking care of its correct identification.
- ◇ Calculate radiative corrections and their impact on the asymmetries.
- ◇ Make a systematic uncertainties' study.
- ◇ Implement other techniques of correction, with special interest in brand new techniques such as the mentioned Omnifold.

Part II

Towards precision timing instrumentation for HEP experiments

Chapter 10

Introduction

This era of accelerators has reached its top performance. The ongoing *Run 3* of the LHC has defined a new benchmark for colliders and its conclusion will mark the end of a fruitful period of data taking at experiments such as *ATLAS* and *CMS*. Future upgrades of these facilities like the **H**igh **L**uminosity **LHC** (HL-LHC) [34] and brand new projects such as the *EIC*, introduced in Chapter 1, are on their way with new challenges for the technologies.

The HL-LHC proposes a luminosity increased of about a factor of 4 from the current value of $10^{34}\,\mathrm{cm}^{-2}\mathrm{s}^{-1}$. The collaboration has estimated a dramatic rise in the pileup of detection with the present detector's state. This could complicate a successful vertex determination in detriment to the quality of the analyses. As a solution, the use of detectors with a fast and highly precise time determination would add another tool to determine vertex and disentangle multiple tracks. However, the high fluency of ionizing elements will require the sensor to be resistant enough to survive long term direct hits. EIC also aims to reach luminosities in that order of magnitude, presenting similar problems.

These conditions produce a stringent technological requirement for the projects to be feasible: new detectors must achieve time resolutions of around $30\,\mathrm{ps}$ at most and keep functioning with fluences[1] of $1.5 \times 10^{15} n_{eq}\ \mathrm{cm}^{-2}$ to give positive results in the vertex determination and particle identification. Moreover, higher granularity would present a major improvement for subsequent upgrades, such as the **H**igh **E**nergy **LHC** (HE-LHC) that is expected to reach center of mass energies of up to $27\,\mathrm{TeV}$ [35].

[1]The n_{eq} symbol means '$1\,\mathrm{MeV}$ equivalent neutron fluence' and it's a common representation of the total radiation deposited in a detector. It also serves as a standardized measure of the damage any particle could produce in terms of the known neutron effect as reference.

All of these examples would be benefited by what is called a *4d-tracker*. Current detectors have dedicated modules specialized in saving certain information from the tracks left by a particle, such as their time of interaction, energy deposited, position of hit, etc. Good timing performance is usually accompanied by poor spatial information and vice versa. A device capable of obtaining good spatial and timing performance simultaneously would be a breakthrough. A reduction in the number of detector's layers would clean the signal from noise created by secondary interaction and the electronics as well as provide new techniques for particle identification. Our study on characterization of sensors developed by world's recognized institutions intends to calibrate or discard candidates for 4d-trackers.

Chapter 11 gives the basic definitions for understanding the analysis. An introduction to the properties used in the characterization of sensors and their technology is mentioned too. Chapter 12 presents the experimental setup, including a description of the beam, facilities, instrumentation used, and the detectors tested. The main body of the text is in Chapter 13 covering the measurements and presenting the final results. Finally, a brief summary of the performance of the sensors as well as comments and suggestions for future samples is discussed in Chapter 14.

Chapter 11

Low Gain Avalanche Detectors (LGADs)

Depending on the nature and properties of the particle under study, a specific type of detector could be more suitable for a correct identification and tagging of the event candidate. For instance, trajectories of charged particles such as electrons can be curved with magnetic fields due to their sensitivity to the electromagnetic interaction, providing a tool to identify them. This is not possible with neutral particles such as photons or π^0. As a result, a completely different principle of operation should be used for dedicated detectors. A series of examples of these techniques were introduced in Chapter 4 of Part I of this thesis.

The large majority of detector components could be grouped into one of two sets: *scintillators* that record a signal from photons and *proportional counters* that directly collect electrons from the ionization of a material. Scintillators were somewhat covered in the previous part with the description of the Time Of Flight (TOF) and Electromagnetic Calorimeter (ECAL) systems. They generally use reflection properties to focus the signal in an analog way, without complicated electronics in the bulk of the component. On the other hand, proportional counters require an electric field to attract electrons to a reading channel. The cascade or avalanche effect plays a central role in those. A single interaction could trigger a chain reaction that ends up making a signal in a circuit. Examples of this idea were also mentioned in the Drift Chambers (DCs) subsection.

A type of proportional counter using brand new technology will be introduced in this chapter. Their properties and features will be also covered. Other definitions essential for the rest of the work are commented too.

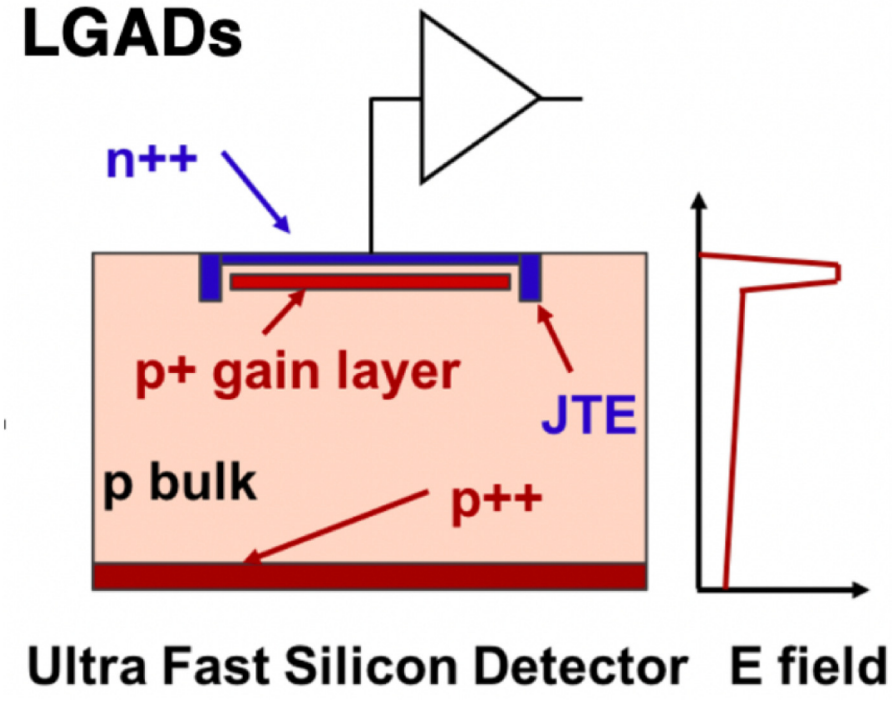

Figure 11.1: Scheme of the main components of a LGAD sensor. A qualitative depiction of the electric field magnitude at different depth of the sensor is shown too.

11.1 The LGAD technology

The devices of interest for this study are generically called **L**ow **G**ain **A**valanche **D**etectors (or **D**iodes) (LGADs). They are silicon detectors that use the avalanche effect in a doped region to amplify a signal that travels through the active thickness of the sensor.

The basic configuration of a LGAD sensor is presented in Figure 11.1. Firstly, the bulk of the interactive media is composed of the substrate and a grown epitaxial layer over it. The main arrangement consists of two layers of doped silicon creating a p-n junction at the top border of the device. A n^{++} implant covers the outermost layer. Below it, a p^{+} silicon layer usually doped with boron is located. A Junction Termination Edge (or Extension) (JTE) is placed around the structure. This later is a mechanism for avoiding charges to travel through certain portions of the detector, to prevent signal leaking and inhomogeneities in the inner electric field. When a bias voltage is applied the p^{+} layer is depleted, leading to an intense electric field. This in turn accelerates any charged particle passing through the zone, stimulating the ionization of the rest of the material. That is the reason why this layer is often called the *gain layer*.

These sensors are designed to work in reversed-bias mode. This makes the device, in principle, sensitive to particles that can generate a significant signal only. On the other

hand, the essential feature of the configuration is the amplification of the signal in the gain layer. This component is expected to increase the number of charges by a factor of 5 to 100. It has been demonstrated that LGADs achieve their best performance at bias voltages near the breakdown [36, 37]. This would also make the device highly sensitive to noise and background that could produce false signals. Consequently, the sensor is functional for particles that don't generate a large current, since this would break the system and very likely kill the sensor. This produces a natural interest in minimum ionizing particles (MIP). MIPs are not a specific entity but the state of any particle when it minimally interacts with the environment. Every charged particle will ionize when passing through a material. Also, it possesses a range of energies/velocities where the media is ionized at an almost constant rate, known as the minimal ionization regime. The Bethe-Block curve models the evolution of the energy deposited and depends on parameters such as the composition of the media, and the velocity and mass of the particle. Figure 11.2 presents a list of particles and their respective curve with diverse materials as a function of the particle's energy. Heavier particles need more energy to be considered a MIP. At lower energy values, all particles end up ionizing at a huge rate until it is completely stopped.

A functional LGAD has the components described above organized as in the left image of Figure 11.3. Special care on the dimensions, like the relation of the thickness and area of the layers, was taken in order to assure an homogeneous inner electric field. The principle of operation requires an ionizing particle to interact with the bulk. A series of electrons and holes will drift due to the internal field mentioned. Since electrons have a faster mean velocity than holes, we use them as prompt to generate the signal, thus they move towards the gain layer. New models of LGADs with other fascinating characteristics use holes for the reading instead [39, 40]. The charges get multiplied after interacting with the gain layer. Later, they are collected by the metallic structure on top. This model receives the current directly from this metal part, thus re-labelled as DC-LGAD afterwards to avoid conflicts with other models such as AC-LGAD, iLGAD, etc.

The same general structure is repeated for AC-LGADs with subtle but fundamental changes. Figure 11.3 right depicts a transverse cut of the model. A dielectric layer is placed between the reading pads and the outer n^+ doped layer. The doping of this last

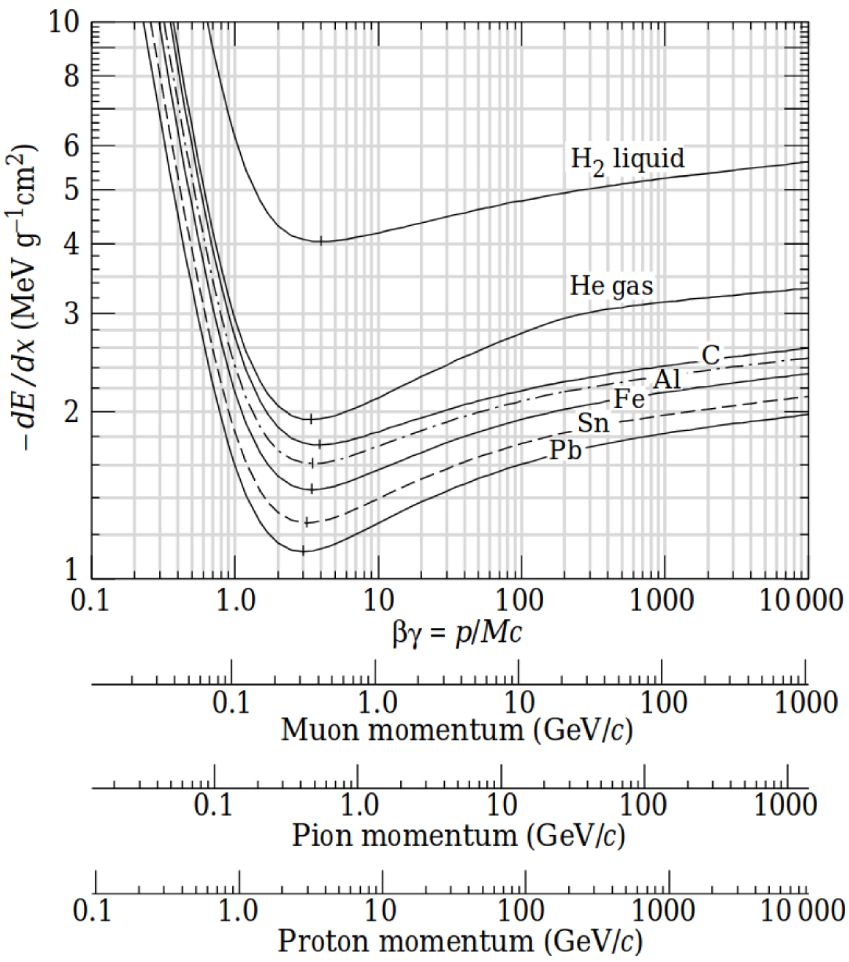

Figure 11.2: Bethe-Bloch curve for a variety of particles and materials in logarithmic scale. Taken from Chapter 34 in [38].

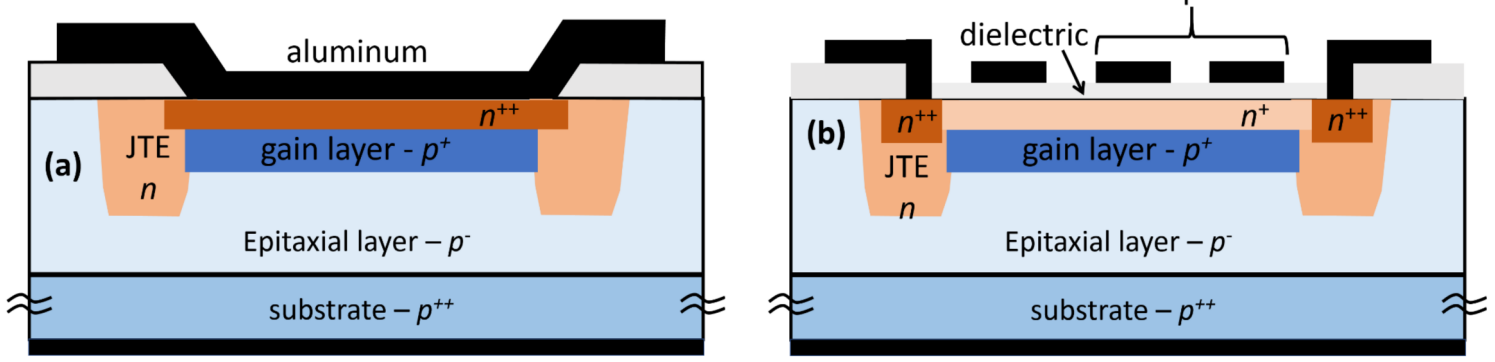

Figure 11.3: Internal structure and composition of a DC (left) and AC (right) LGAD sensor. Diagrams extracted from Reference [41].

one is different so that another n^{++} implant, with a tendency to attract more electrons, is imbedded in certain regions surrounded by JTEs and directly connected to a grounded metal section, different from the pads located over the dielectric. This configuration creates an electric field that permits the ionization current to get collected by these end connections. The charges are forced to travel below the dielectric. Therefore, charge is induced in the pads, generating an AC signal that is recorded by the oscilloscope. This system is said to be of net zero charge since no charge is collected, just induced.

The flow of direct or alternating current produces a pulse shape that can be recorded with an oscilloscope. We define some properties of the wave form that will be useful for characterizing the response of the sensor. An usual feature observed is the oscillation of the signal around a central value. This value is known as *baseline* and the mean deviation from it is regarded as *noise*. Random interactions from external events such as astroparticles or the electronics produce these variations. The height of the peak from the baseline is the maximum *amplitude*. Independent of the model, the pulse shape encodes details about the charge deposited in the sensor by ionization. The integral of the pulse gives a quantity that is proportional to the charge. Assuming an impedance in the order of $\sim 50\,\mathrm{k}\Omega$, the charge would be in the order of the fC.

The time length from the beginning of the pulse to its peak is commonly known as *rise time*. For practical reasons, it's not customary to take the whole range because of the loose definition of the initial time. Instead, a fraction of the total is taken. A $10-90\%$ or $20-80\%$ are the usual selections. The former definition will be used for the rest of the text. Finally, the *slew rate* is a related quantity that could be intuitively thought as the the slope of the pulse. A formal definition would be $\frac{dV}{dt}$ and, in practice, we take the maximum slope as the characteristic value.

The LGAD technology has demonstrated outstanding timing performance. A correct measurement of this quantity requires a careful consideration of all of the contributions. This is imperative especially in these sensors where some terms that are usually neglected could be of a size comparable to the overall performance [42]. Apart from constant offsets and delays, the whole readout system introduces a component of uncertainty named *jitter* associated to the noise. Also, the time walk of the ionization process can be

modelled as a Landau distribution, adding another source of uncertainty. A simplified version of the total time resolution is

$$\sigma_t^2 = \sigma_{\text{Landau}}^2 + \sigma_{\text{jitter}}^2 + \sigma_{\text{delay}}^2. \tag{11.1}$$

The Landau contribution has been set to approximately $30\,\text{ps}$ for the usual $50\,\mu\text{m}$ active region's thickness. This quantity often represents the limiting resolution of the configuration. Additionally, the jitter can be extracted from the pulse shape previously discussed. Its effect is given by two equivalent definitions:

$$\sigma_{\text{jitter}} = \frac{\text{rise time}}{\text{SNR}} = \frac{\text{Noise}}{\text{slew rate}}, \tag{11.2}$$

where $\text{SNR} = \frac{\text{Signal}}{\text{Noise}}$ is the signal-to-noise ratio. The delay contributions are usually small enough to be safely neglected. In summary, the main sources of uncertainty are the Landau (often denominated *Landau floor*) and jitter terms.

A final comment on AC-LGAD's special features. Charge is induced in different amounts in the metal pads of the surface. This could give valuable information about the location of the hit. Since a finite amount of charge is deposited in the device, we can compute how much of it has been split in the channels. We call this effect the *signal sharing* property and we will exploit it to improve the position resolution. The method has a disadvantage, though. Each of the pads could in turn polarize their neighbours. This effect is known as *cross talk* and is similar to the sharing. Both happen at the same time, so it is hard to distinguish one from the other. In terms of the pulse shape, the cross talk affects after having charge deposited in the pads, so we see an asymmetry in the pulse due to an increased time of recombination of the charges.

Chapter 12

Instrumental facilities

In this section the setup used for testing the sensors, a description of the beam and features on the data taking are also reviewed.

12.1 The Fermilab Test Beam Facility (FTBF)

The Fermi National Accelerator Laboratory (Fermilab) is a particle physics laboratory located in Batavia, Illinois, USA. The laboratory is widely known for its involvement in discoveries and research on technology. The discovery of the top quark (t), B_s oscillations, and the observation of two types of Σ baryons are among its most successful contributions. The proton's accelerator system consists of two main structures: the Main Injector Ring and the Tevatron (both presented in Figure 12.1).

Tevatron is the bigger structure and not long ago was recognized as the accelerator with the most energetic beam (a few TeV) and highest luminosity ever achieved (in the order of $10^{32}\,\mathrm{cm}^{-2}\mathrm{s}^{-1}$). It reached energies going up to $1\,\mathrm{TeV}$ and might be the most famous building of the laboratory, being the principal ring and with which most of the discoveries mentioned were done. This accelerator ceased operations in 2011 and cleared the way for the, at that time, recently commissioned LHC, which was just starting to work with around four times higher energy and similar luminosity. Even though nowadays it's not fully working, portions of it are used to help the Main Injector in getting beam to certain experimental halls.

On the other hand, the Main Injector was used along with the Tevatron as the initial beam injection, reaching energies of $150\,\mathrm{GeV}$. Even today it is still used for several ex-

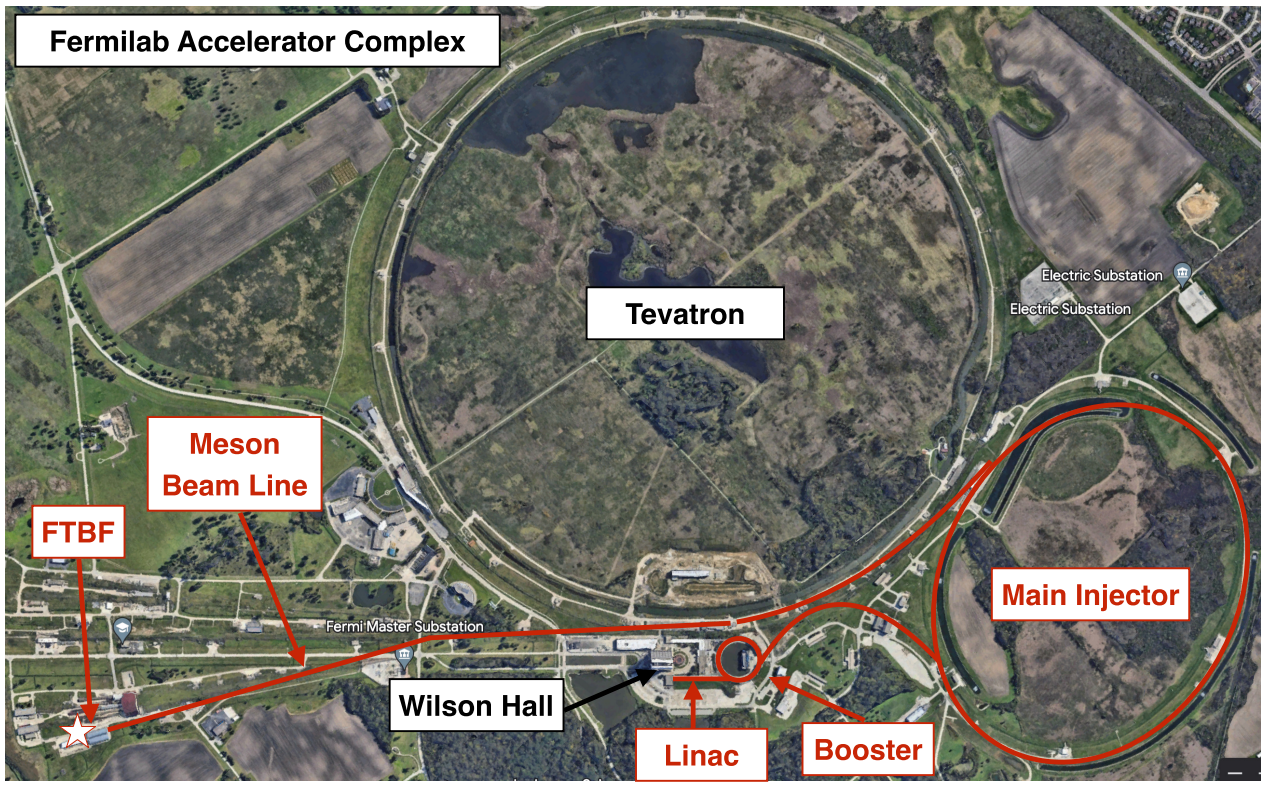

Figure 12.1: Satellite photo of the Fermilab complex with the Main Injector, Tevatron, and Fermilab Test Beam Facility (FTBF) among others highlighted.

periments and there are prospects on using it in future research. Renowned programs such as the *Muon g-2* are currently using this facility. Some neutrino physics studies were performed with this initial beam too by various experiments such as *MINERvA*, *MINOS*, *NOvA*, and *DUNE*.

The left portion of Figure 12.1, where the Meson Beam Line is, separates the beam in three lines. Each of them has a different portion of the initial luminosity and can be used for different purposes. For instance, some radiation tests were developed in the branch with the highest flow. Our interest is in the branch that gets to the Fermilab Test Beam Facility (FTBF) [43].

The FTBF is the building that houses the end of the beam line and where our experimental enclosure is located. The proton beam reaches energies of $120\,\mathrm{GeV}$ at this point. As it was mentioned in Chapter 10, the sensors are expected to work in the outer layers for MIPs, so we must test them in an environment that mimics this situation.

The main feature of the enclosure is the tracking system, named the *Silicon Telescope*. This structure is a dedicated system for charged particles' tracking that achieves high precision measurements with resolutions of $5\,\mu\mathrm{m}$, mounted along the beamline [44]. The Telescope readout system is capable of accumulating up to 150,000 beam tracks per minute with a fast triggering time of a few ns. The whole structure was designed to be

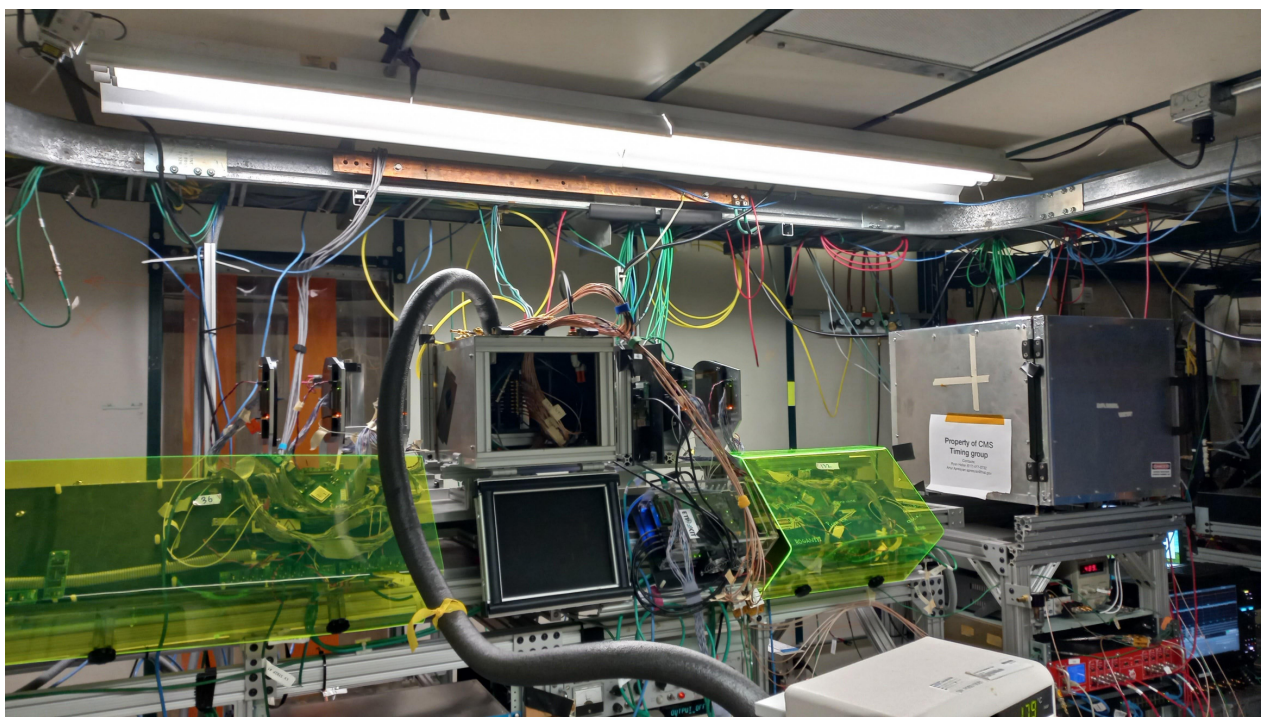

Figure 12.2: Enclosure at FTBF with the DUT box at the center, pixels and strips from the telescope at both sides of it, and the rear box at the right.

minimally interacting, leading to negligible beam-scattering effects. All the components of the tracker only sum up to 11% of the total radiation length of protons. Two types of detector constitute the Telescope: 6 strip stations and 4 pixel planes modules.

The strip stations are composed of two strip arrays each (12 layers in total), oriented orthogonally to get good x and y measurements. The strips are $9\,\mathrm{cm}$ in length, with a thickness of $320\,\mu\mathrm{m}$, and $60\,\mu\mathrm{m}$ pitch. Correctly aligned, the contribution of all of the layers gives an overlap coverage area of $3.84 \times 3.84\,\mathrm{cm}^2$.

The pixel system was made using leftover modules from the CMS Forward Pixel detector and were recently upgraded from Phase 0 CMS pixels to Phase 2 CMS pixels, only available for the 2022 measurements. A total of 4 planes were installed, tilted $90°$ one with respect to the next, giving a difference in the resolution achieved depending on the orientation of the array of pads. The original configuration used pixel cells of size $100 \times 150\,\mu\mathrm{m}^2$, making a total square active area of around $0.81 \times 0.81\,\mathrm{cm}^2$ per pixel. A layer has an array of 2×4 pixels generally, leading to an area of $1.62 \times 3.24\,\mathrm{cm}^2$ for a single layer and, finally, a whole system's overlap coverage area of around $1.6 \times 1.6\,\mathrm{cm}^2$. For the upgrade, cells of $25 \times 100\,\mu\mathrm{m}^2$ were used, in arrays that led to an active area of $1.36 \times 0.96\,\mathrm{cm}^2$. After aligning, the modules overlaps on a region of $0.96 \times 0.96\,\mathrm{cm}^2$, with four expected pixel hits per track.

A Fermilab readout board of 16 independent channels has the device under test (DUT)

mounted on it, giving the flexibility for reading several channels in parallel. External to this system, a micro-channel plate photo multiplier detector (MCP-PMT) commonly called *Photek* with an excellent time resolution of about $10\,\mathrm{ps}$ is connected downstream, inside the rear box, to be used as a time reference (see Figure 12.2). This sensor and the channels of interest of the DUT are connected to a Lecroy Waverunner 8208HD oscilloscope where signals are read, triggered by a scintillator[1], and stored by making use of the DAQ system integrated on the Telescope. The oscilloscope has up to eight readout channels (seven DUT channels + one saved for time reference) with a bandwidth of $2\,\mathrm{GHz}$ and a sampling rate of $10\,\mathrm{GS/s}$ per channel.

12.2 Sensors under test

A selection of LGADs were developed by two main fabricators: KEK/Tsukuba group in collaboration with Hamamatsu Photonics K.K. (HPK) and Brookhaven National Laboratory (BNL). The study of the properties and comparison of the probes was divided in different campaigns of data taking carried out between 2021 and 2022.

Previous studies on radiation strength demonstrated how DC-LGADs were suitable for long term studies in radiation zones with high pileup, requirements introduced in Chapter 10 for future experiments. According to those results, a carbon implant apart from the boron in the gain layer helps in reorganizing the semiconductor structure faster and enhances the sensor's expected lifetime without significant impact on its performance. This feature has been exploited especially by the BNL models.

The AC couplings of sensors with string configuration were read by a wire bond on the ends of the strips in an alternating pattern. This distribution optimizes the space between the connections to the sensor and the readout board and helps in compensating for signal propagation delays by mixing information of neighboring strips. This last consideration is of great importance for larger strips, where significant differences in the readout time of the signals are expected.

The gain layer as well as the bulk and all of the silicon components were produced in a

[1]On the 2021 campaign, the AC-LGAD runs used a DC-LGAD as trigger.

common wafer from which several sensors were cut. This ensures that all of the devices have the same composition in each batch of sensors so that the response is expected to be the same under similar conditions.

12.2.1 First Campaign (2021)

The main purpose of the 2021 campaign was to compare the performance of sensors created by different vendors with different geometries (pads and strips). For the strips case, we had a model from a previous test (so called *BNL 2020*) that was intended to be used as a reference. This involved the commissioning of a new oscilloscope, so any significant improvement in the results obtained for the last year's sensor could be addressed by this. It is important to remark that the Telescope had a previous version of the pixels available at that time, providing an overall worse spatial resolution in the order of $50\,\mu\mathrm{m}$.

The sensors tested are shown in Figure 12.3 and their specifications are listed:

- HPK pads: Pads of $500 \times 500\,\mu\mathrm{m}^2$ were placed in 2×2 arrays using wafers with an active thickness of $50\,\mu\mathrm{m}$ but different doping, labelled as *B2* and *C2*[2]. Both wafers have the same p^{++} doping concentration but C presents a higher n^{+} resistivity (around 3 times) than B. Each sensor has its four pads at different distances, with gaps of 20, 30, 40, and $50\,\mu\mathrm{m}$.
- BNL 2020: An array of 17 strips of $1.7\,\mathrm{mm}$ length and $80\,\mu\mathrm{m}$ width, with a pitch of $100\,\mu\mathrm{m}$ between each strip center. The active region has $50\,\mu\mathrm{m}$ of thickness.
- BNL 2021: An array of three groups of six strips (18 in total) with a variable pitch per group of $100, 150, 200\,\mu\mathrm{m}$. All of them have $2.5\,\mathrm{mm}$ length, $80\,\mu\mathrm{m}$ width, and $50\,\mu\mathrm{m}$ of active thickness.

12.2.2 Second Campaign (2022)

Only BNL sensors were considered for this study. A collection of 15 different AC-LGADs were tested, but the analysis focused on five with similar characteristics to identify the effect certain geometrical parameters had on the properties of the sensor such as the

[2]The nomenclature is explained in Table I of [45] along with the presentation of other models not tested here.

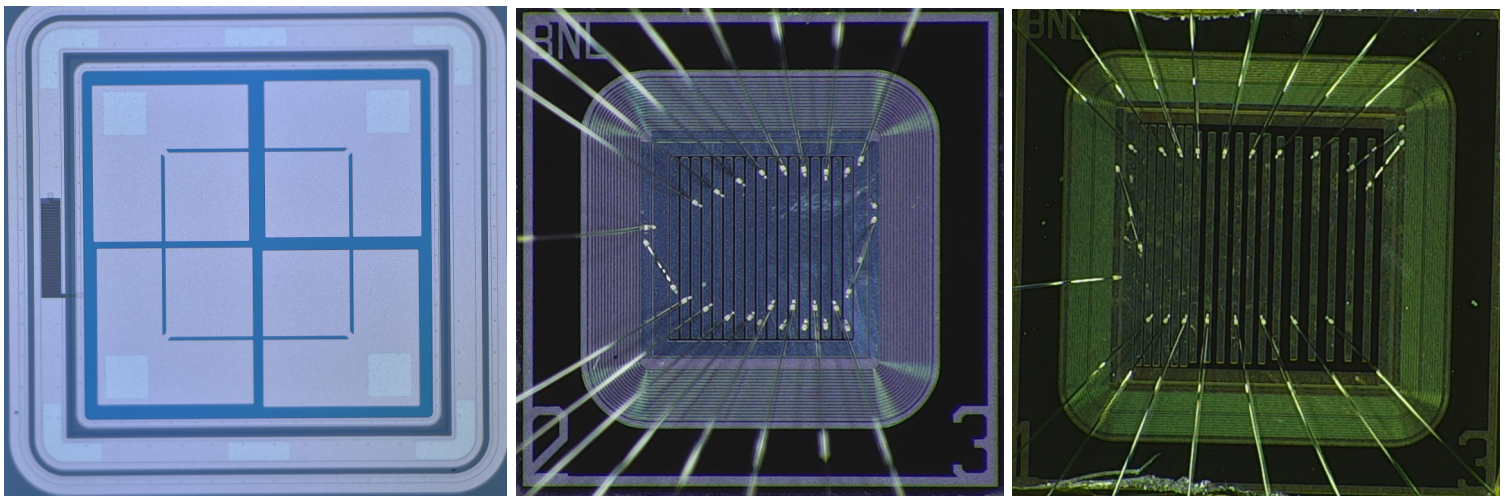

Figure 12.3: Photograph of the sensors tested in the 2021 campaign: HPK pad (left), BNL 2020 (center), and BNL 2021 (right). A detailed description of their geometry is given in the text.

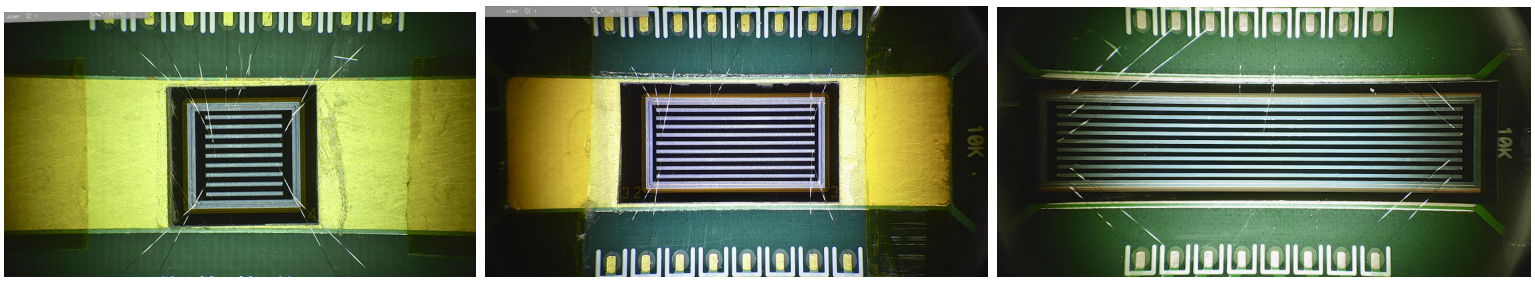

Figure 12.4: Photograph of the sensors tested in the 2022 campaign with strip length of $0.5\,\mathrm{cm}$ (left), $1\,\mathrm{cm}$ (center), and $2.5\,\mathrm{cm}$ (right). A detailed description of the remaining geometric parameters is given in the text.

resolution. The five sensors had the same pitch of $500\,\mu\mathrm{m}$, active thickness of $50\,\mu\mathrm{m}$, and wafer substrate of $300\,\mu\mathrm{m}$. Three of the sensors had $1\,\mathrm{cm}$ long strips with variable width of 100, 200, and $300\,\mu\mathrm{m}$. These are presented in Figure 12.4. The remaining pair of sensors had strips of $200\,\mu\mathrm{m}$ width and different lengths of 0.5 and $2.5\,\mathrm{cm}$, respectively. Given their similarities, we will refer to the elements of this batch by their strip length in mm and width in $\mu\mathrm{m}$, labelling them as *BNL (length* mm*)-(width* $\mu\mathrm{m}$*)*. For example, the sensor of $1\,\mathrm{cm}$ long and $200\,\mu\mathrm{m}$ width will be called *BNL 10-200*.

Chapter 13

Results

The data taking campaigns had the objective of testing the capabilities of different configurations of LGAD sensors and show how their geometries could affect the performance of the whole system. The properties of interest for these configurations are the spatial and temporal resolutions, detection efficiency, and charge deposited, among others that will be properly introduced below.

13.1 First Campaign (2021)

13.1.1 BNL strip sensors

The first focus of the study was in the BNL sensors with variable pitch. A previous publication presented simulations for the response of the AC-LGADs as well as a good performance of the 2020 batch [46]. Nevertheless, these results were limited by the Telescope system capabilities and the readout system. This last point was relevant, since a main feature of these sensors is the charge sharing capacity. This attribute was not fully exploited in the preceding campaign due to the maximum number of channels available in the oscilloscope in usage at that time. Only four channels could be read, resulting in three saved for the strip's responses and one extra saved for the timing reference. Our upgraded setup, introduced in Chapter 12, includes a refined system with capacity of up to 8 channels, providing the environment to study brand new possibilities such as a multi-channel signal readout. The main study is not only focused on the variable pitch response. In addition, updated measurements from the past sensor will quantify the im-

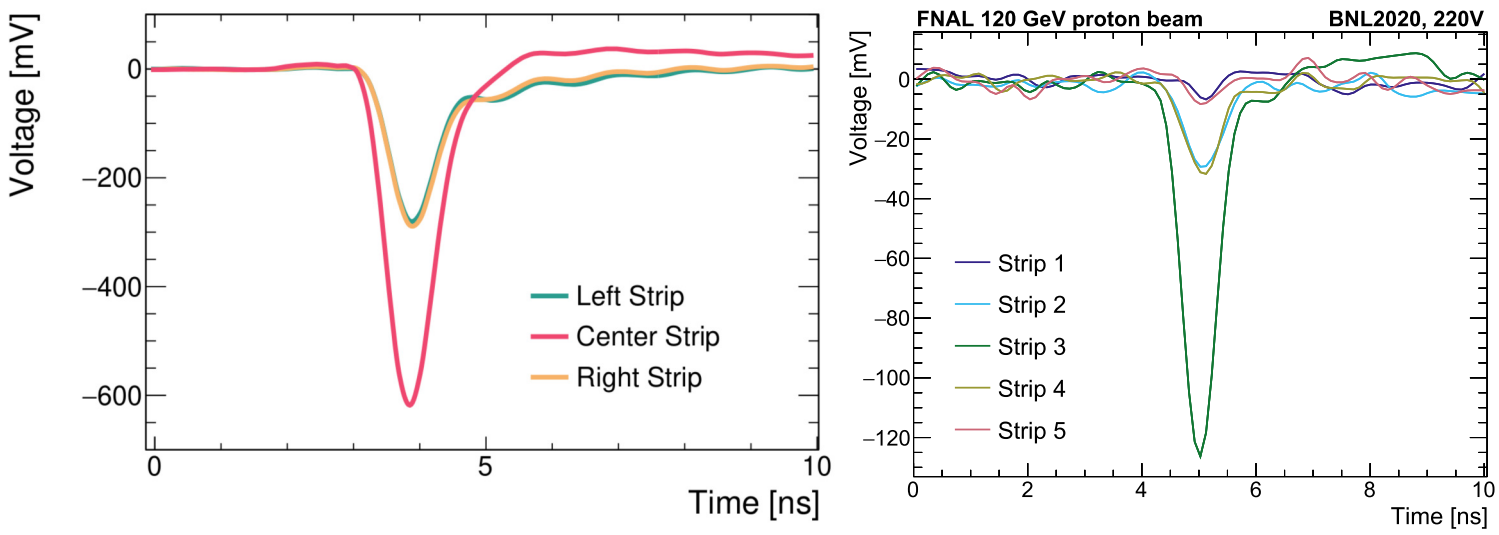

Figure 13.1: Pulse shape in a $10\,\mathrm{ns}$ time window for a direct hit in a strip. The previous result (left), with only three channels available, had the central strip hit. The 2021 result (right), presenting five channels, had the third one hit. The signal recorded in adjacent and next-to-adjacent strips is also presented.

provement of the setup as well as serve as a reference to contrast the characteristics of the new batch.

Healthy signals were reported as presented in Figure 13.1. The neighboring channels are well defined, easily spotted with a smaller amplitude. This is a good sign for the quality of the resistive layer. Note a second peak, an *overshoot*, after the main peak. Its presence is predominant in the hit channel and it's related to the recombination of charge in the AC-pads. The thickness and composition of the p-n junction affect the shape of the wave form. This aspect is crucial for the development of future devices, since a shorter tail of recombination could reduce the dead time of the sensor.

For the analysis, a Constant Fraction Discriminator (CFD) is used to define the timing information. We use a local polynomial fit to reconstruct the first half of the main peak and define different timestamps associated with a certain percentage of the maximum signal. The rise-time is defined as the time required to go from 10% of the peak to 90%. This definition prevents triggering with noise, though it is sensitive to the recombination peak (overshoot). Note that the polarity of the peak, this is the sign of the voltage, is not fixed by construction but is presented as negative for consistency. A substantial overshoot could trigger the collector, thus reducing the efficiency of detection.

The time reference (Photek) is located downstream at a fixed distance from the DUT. The delay is in the order of $10\,\mathrm{ns}$. This constant offset is used to define a narrow time

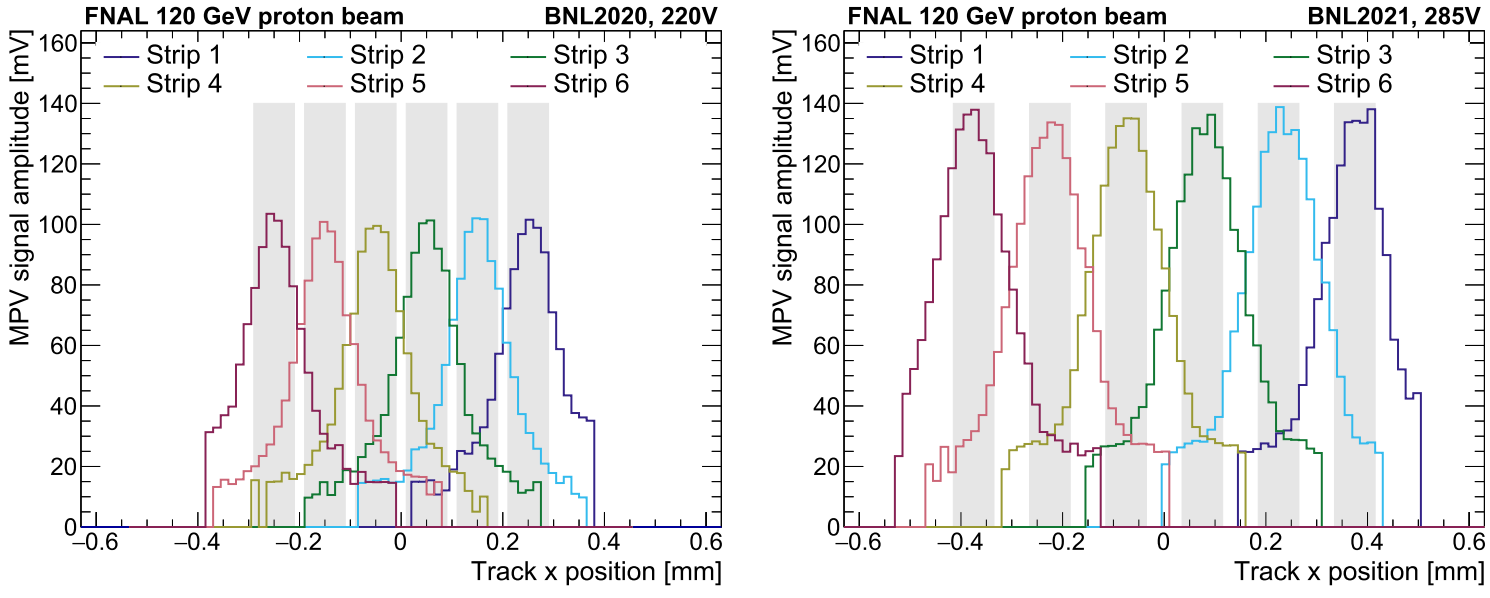

Figure 13.2: Most probable value (MPV) signal amplitude in strip sensors vs x sensor position. BNL 2020 (left) and BNL 2021 with $150\,\mu\mathrm{m}$ pitch (right).

window of $10\,\mathrm{ns}$ in the oscilloscope for taking data. Everything outside that range will be discarded. The tuning of the offset optimizes the use of memory and saves resources.

The peak of the wave form is regarded as the *maximum amplitude* and it is saved for each event in every individual channel. From these quantities we can define a leading channel, the one with the highest portion of signal, and sub-leading channels in decreasing order of amplitude. The most probable value (MPV) of this amplitude distribution is presented for the individual channels in Figure 13.2. The values achieved by the 2020 sensor are around $100\,\mathrm{mV}$ for direct hits. This is clearly smaller than the result in the new batch, with values of $140\,\mathrm{mV}$. Even though both configurations are different in terms of geometric parameters such as pitch and strip length, the discrepancy of the maxima is explained by the bias voltage applied. A higher voltage, near but below breakdown voltage, is expected to produce a larger amplification of the signal.

Two thresholds are defined in order to accept an event from the highest signal's channel or a secondary one. The value for the leading strip was set to $30\,\mathrm{mV}$ for the 2020 device and $40\,\mathrm{mV}$ for the 2021 sensor. The second threshold is implemented to remove noisy signals from the channel with the second highest amplitude. This noise limit was set to $10\,\mathrm{mV}$ and $20\,\mathrm{mV}$ for the 2020 and 2021 devices, respectively.

An algorithm of position reconstruction was developed by taking advantage of the charge sharing. Whenever two or more strips have a signal that is higher than their corresponding threshold an interpolation of the hit position is possible. The reconstruc-

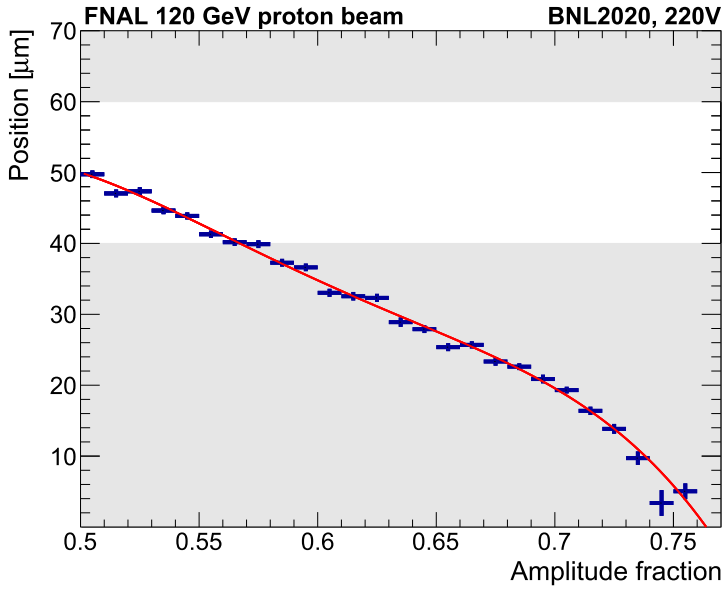

Figure 13.3: Reconstruction function over the original signal profile from the center of the leading channel. A grey rectangle shows half of the leading strip at the bottom.

tion proposed uses the fraction of the total signal at a certain distance from the leading strip to calculate the position of the hit. The fraction is defined as

$$f_i \equiv a_i \Big/ \sum_{j=\{\text{channel}\}} a_j, \tag{13.1}$$

where i is the index of the channel with the highest signal and the sum is over all channels. Negligible improvements were presented after adding extra channels, so only the two leading strips will be considered. The method uses the fact that the profile of the signal sharing is independent of the channel, but depends only on the composition and distribution of the medium. With this, the information from all of the channels can be joined to characterize the charge distribution pattern of the sensor. The distribution is fitted with a polynomial of 4-5 degree as presented in Figure 13.3.

The efficiency of a sensor is defined by the number of events that have the primary and secondary amplitude above their respective thresholds over the total events in the active area. This selection was performed per strip and overall, as it is presented in Figure 13.4. Note how the metallic sections of the strip hit reaches full efficiency over its surface. This extends outside the metal into the gap, with significant efficiency even in hits produced on other strips. Overall, the sensor presents a full efficiency in its region of interest.

The spatial resolution achievable by the sensor depends on the method of reconstruction implemented. The process described above uses the position given by the tracker as a reference and measures how displaced is our estimation from it. Another method

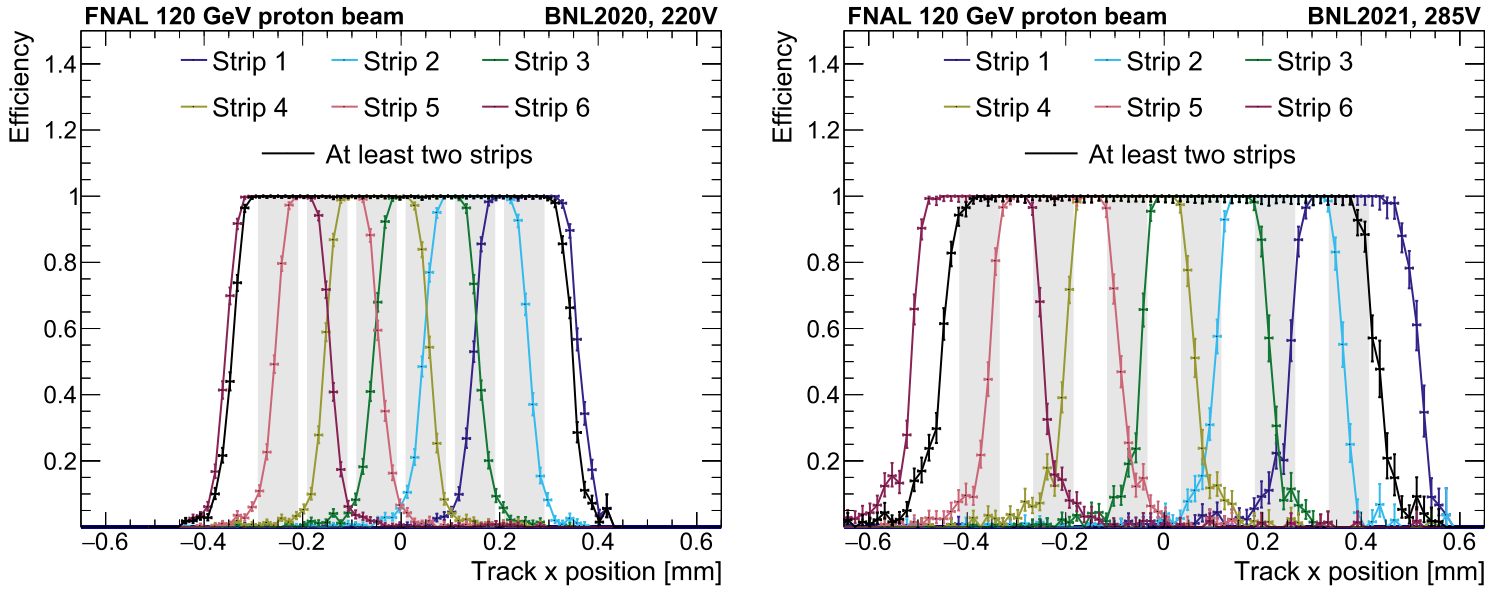

Figure 13.4: Efficiency vs x sensor position. BNL 2020 (left) and BNL 2021 with $150\,\mu\mathrm{m}$ pitch (right). The strips are depicted as grey rectangles in the background for reference.

of reconstruction is called the *binary readout*. As its name suggests it is a dichotomous selection, to accept or reject an event. This is the simplest implementation since we only define the signal threshold and associate the hit to the leading channel. We can certainly limit the region of interaction, but further information is not available so the description is not very precise. The resolution value of this method is given by assuming a uniform distribution in the active region surrounding the channel. This ends up being pitch$/\sqrt{12}$. Both methods are contrasted in Figure 13.6. The x position is defined along the array of strips, perpendicular to them. This formulation is useful for determining the homogeneity of the reconstruction over the active region. A remarkable improvement of the so called *two-strip reconstruction* is found with respect to the binary readout. The tracker's contribution is estimated to be $5\,\mu\mathrm{m}$ and is not subtracted in the plot. In general, the method gives rather uniform values, lower than $8\,\mu\mathrm{m}$, with a tendency to better results in the gaps. Some bins in these interfaces get values down to the tracker's capacity.

The timing performance in previous LGADs has been outstanding. DC-LGADs demonstrated to reach precision of $20 - 30\,\mathrm{ps}$ [47]. Two methods of timing determination were developed, both with the signal sharing as central mechanism. First of all, a fine correction of the time stamp is added for each individual channel, apart from the constant Photek offset. This correction has to do with the wire bonds described in Chapter 10, since adjacent strips are bonded in opposite ends. The correction is in the order of $0.5\,\mathrm{ns}$ in general. The distribution of the difference of these corrected values with the Photek

time is fitted with a Gaussian-ish shape to extract the resolution. A second method uses the signal sharing to make a weighted-average of the hit time, following:

$$t_{w^i} = \sum_{j=\{\text{channel}\}} w_j^i t_j, \qquad w_j \equiv f_j; \tag{13.2}$$

where the weight is the signal fraction of Equation 13.1 taking all channels in principle[1] and i corresponds to an exponent chosen to be 1 or 2. The resulting weighted time uses $i = 1$ for this analysis and is compared to the Photek timestamp too. A summary of the performance of both methods is shown in Figure 13.7. Though a small improvement is observed overall, the multi-channel method tends to have uniform response in the gaps, reaching values below $30\,\mathrm{ps}$.

13.1.2 HPK pad sensors

The same characterization described in the previous subsection was studied in the HPK sensors with metallic square pads as inductive surfaces instead of rectangular channels. Nevertheless, not only a different geometry is tested but also the resistive layer composition as discussed in Chapter 12. Beginning with the MPV signal detected by the different pads in Figure 13.5. We see a clear differentiation in the maxima of both samples. Even though the bias voltage applied on the B2 sensor is higher than on C2, the latter got an amplified signal of up to $130\,\mathrm{mV}$, contrasting with the $100\,\mathrm{mV}$ at most of the former. This is not surprising, since a higher resistance requires more energetic events to be correctly recorded. Also, this explains why the minima are lower in the resistive one too. The total effect could be summarized as a steeper distribution on the profile as the resistance increases.

The reconstruction of both spatial and temporal information uses the same algorithms previously introduced. The summary projections for the C2 pad are presented in Figure 13.6 and 13.7. Without loss of generality, only the x dependence is shown due to the symmetry. The data from top and bottom pairs of pads is summed. Note the non homogeneity in the spatial performance, with a minimum of less than $20\,\mu\mathrm{m}$ in the gap and values that could double that in the inner pads. The multi-channel time reconstruction

[1] As it was discussed previously, usually only the two leading strips are enough to reduce the intrusion of noisy signals.

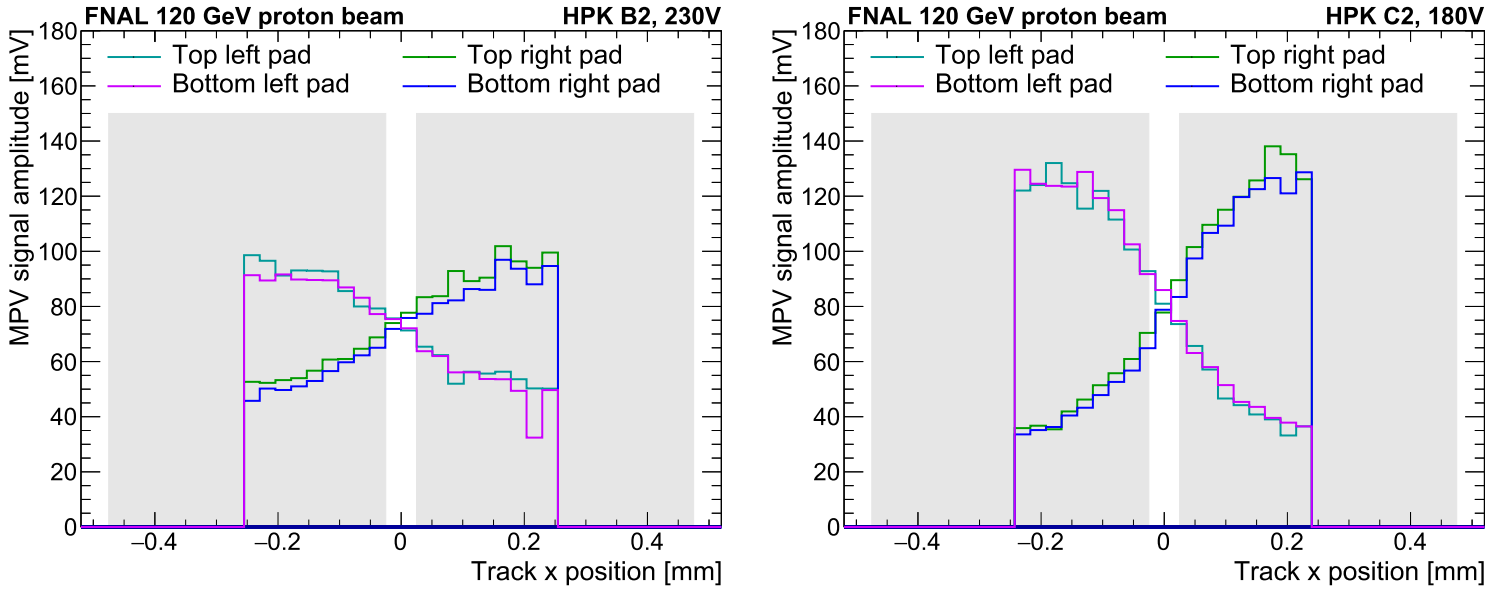

Figure 13.5: Most probable value (MPV) signal amplitude in pad sensors vs x sensor position. HPK B2 (left) and HPK C2 (right).

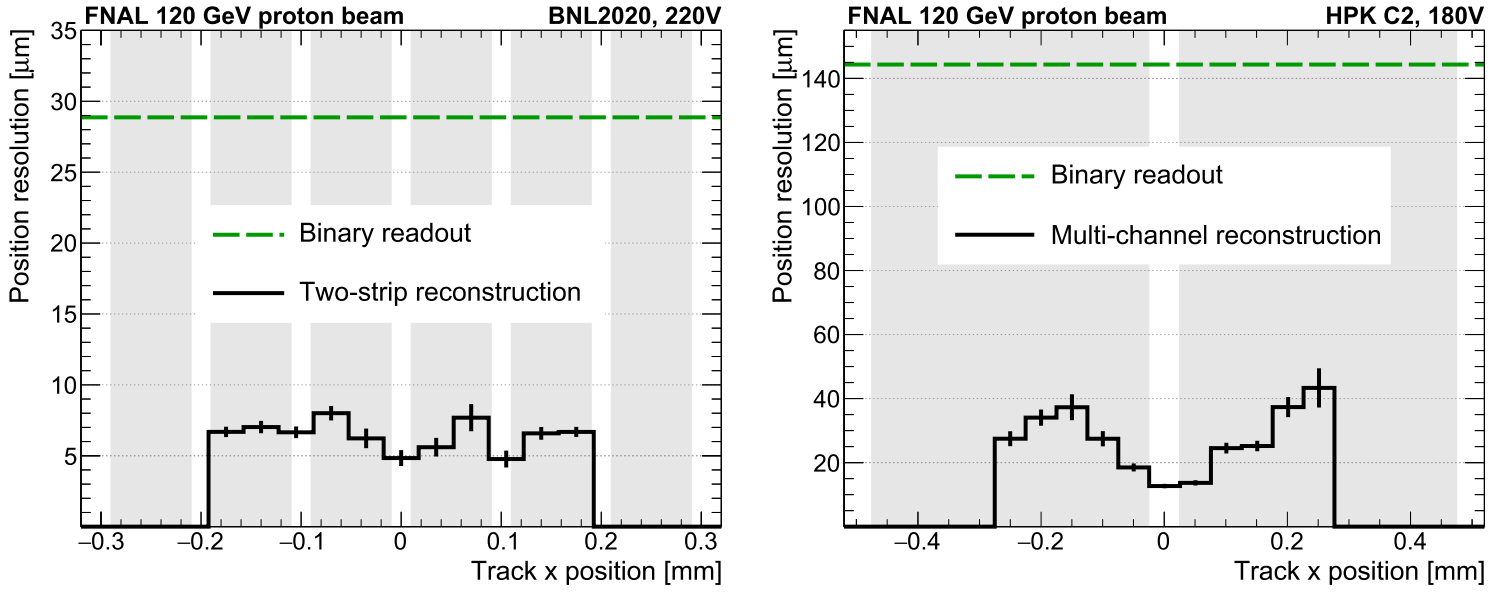

Figure 13.6: Position resolution vs x sensor position. BNL 2020 strips (left) and HPK C2 pads (right).

in pads produces a similar effect as in the strips, slightly improving the resolution in the gap, but with almost no effect in the metal part.

A summary of the quantities reported from all samples, including some not carefully developed in the text, is presented in Table 13.1. The required timing performance was accomplished by all of the samples, with resolutions around $30\,\mathrm{ps}$. A higher pitch increased the signals achieved, probably associated with a higher active area in the surrounding region of each channel. The pads had a sufficient performance, with no clear impact on the results related to the composition of the gain layer. On the other hand, the BNL strips achieved an amazing spatial resolution that competes with that of the tracker system.

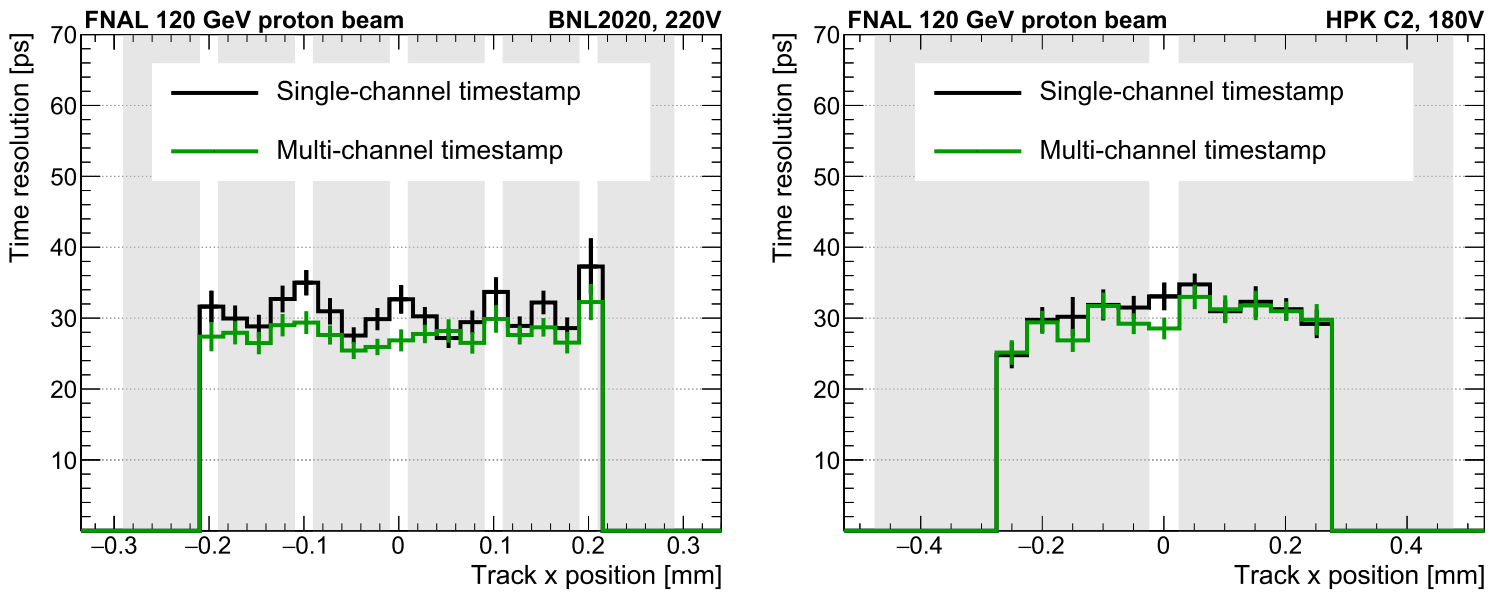

Figure 13.7: Time resolution vs x sensor position. BNL 2020 strips (left) and HPK C2 pads (right).

Table 13.1: Performance summary for BNL strip and HPK pad detectors. A 10% uncertainty is applied to the MPV signal amplitudes, representing the uncertainty in amplifier calibration. The position resolutions quoted for the strips are only upper limits since the measurements are limited by the resolution of the tracker reference. The HPK position resolution and all time resolution uncertainties represent the statistical error, only.

Name Unit	Pitch µm	Primary signal amp. mV	Position res. µm	Time res. ps
BNL 2020	100	101 ± 10	≤ 6	29 ± 1
BNL 2021 Narrow	100	104 ± 10	≤ 9	32 ± 1
BNL 2021 Medium	150	136 ± 13	≤ 11	30 ± 1
BNL 2021 Wide	200	144 ± 14	≤ 9	33 ± 1
HPK C–2	500	128 ± 12	22 ± 1	30 ± 1
HPK B–2	500	95 ± 10	24 ± 1	27 ± 1

13.2 Second Campaign (2022)

The main idea behind the five samples studied is to quantify the impact that some geometric parameters have over the performance of the sensors. Since the pitch was already tested revealing a negligible effect, only two other quantities are varied at a time: strip width and strip length. Our tracking system received the upgrades described in Chapter 12 with a more stable configuration. However, the longest sensors had to receive a special treatment due to their larger size compared to the trigger and the pixels of the telescope. Therefore, a different trigger with a larger transverse area was used for the whole campaign. Additionally, a looser requirement in the number of pixels was applied over the longest strip's data.

In the analysis part, a lot of improvements were added to the framework[2]. A robust process of alignment of the sensor with the telescope system was developed. The sensor's local coordinate system is defined in the sensor's plane, as a 2-dimensional space centered at the very center of the device. This frame is useful for describing what the device 'sees'. But the transformation from the laboratory system is not easy. At best, we can use some observable quantity that gets impacted by the inaccuracy of the alignment of both systems and calibrate based on that. An iterative process was defined using, for instance, the overall spatial resolution in x as a means to correct the rotation of the sensor around the beam axis. This correction was proved to be small for previous samples, given their small sizes. The current batch has dimensions that are more sensitive to it. Figure 13.8 presents the output obtained while tuning the angle of rotation mentioned above. Note how a bad selection could spoil the results from $\sim 26\,\mu\mathrm{m}$ to $40\,\mu\mathrm{m}$. The same process is repeated for the other two angles of rotation (around x and y laboratory) and the z position of the DUT inside the telescope. After two iterations, the parameters converge to values that present variations comparable to the telescope resolution, hence the process is terminated since more precision is impossible.

The pulse shapes of these configurations are summarized in Figure 13.9. Note that each distribution is normalized, thus a correct comparison requires a similar charge deposited. A similar rise time and recombination time is presented for all widths. In con-

[2]Github repository: https://github.com/FNAL-AC-LGAD/TestbeamReco

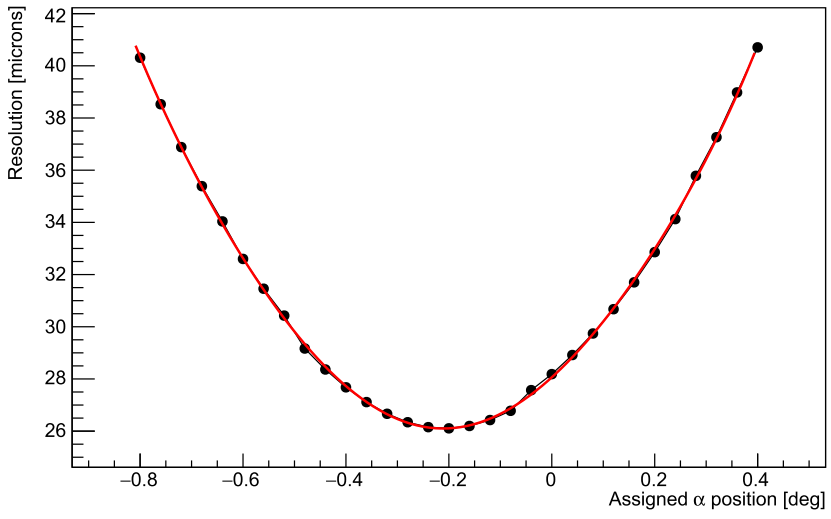

Figure 13.8: Alignment process output for α parameter. Rotation is around the z laboratory axis.

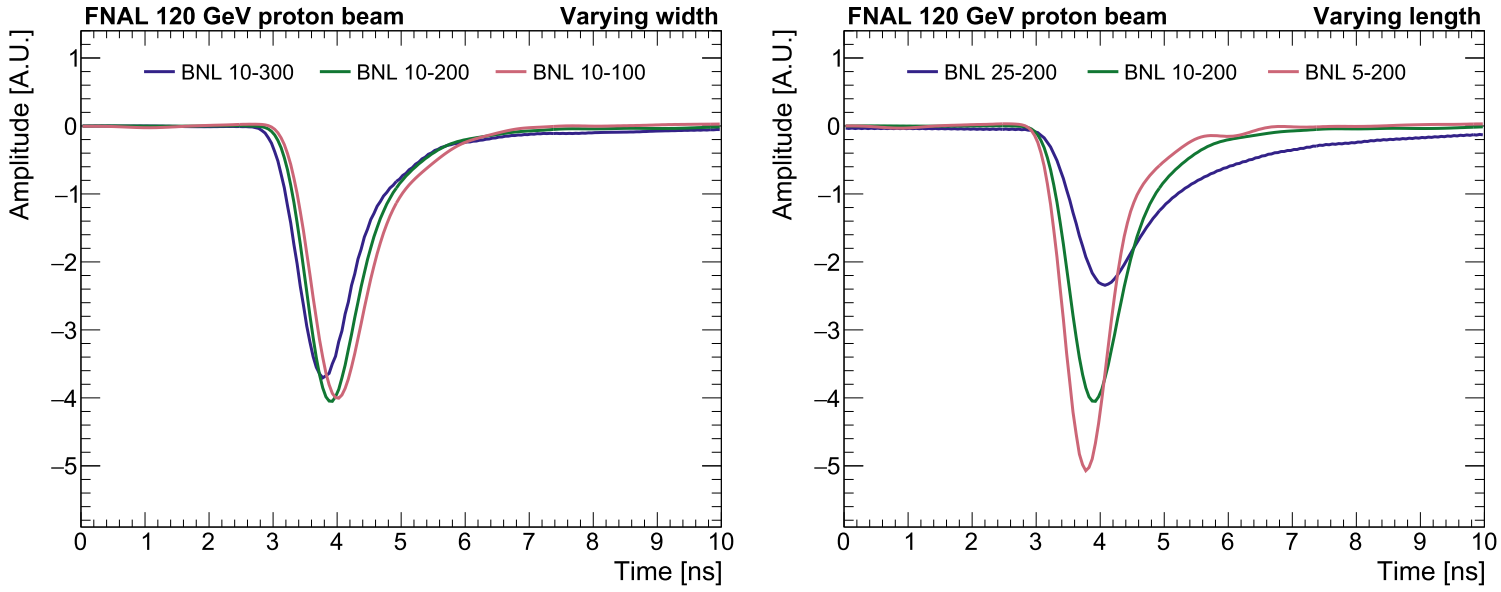

Figure 13.9: Wave form of BNL strip sensors with variable width (left) and variable length (right).

trast, the different lengths have a clear effect on the distributions with a smaller slew rate for shorter strips. This could be explained by recalling the capacitance structure that leads to the induction of the channels. In principle, the main effect should be dominated by the product of width and length. An extra contribution introduced as cross talk in Chapter 10 makes the difference. This quantity should depend directly on the length but not the strips width, so a different response in recombination is not surprising.

To make possible an in-detail characterization of some samples, a huge data set was collected with the $1\,\mathrm{cm}$ sensors of 100 and $200\,\mu\mathrm{m}$ metal width. Some useful representations such as 2-d maps are viable in this context and give a sense of the process better than with 1-d projections. Regarding the amplitudes, we see a lot of features over the surface of all of the samples in Figure 13.10. The signals reach values of around 60 to

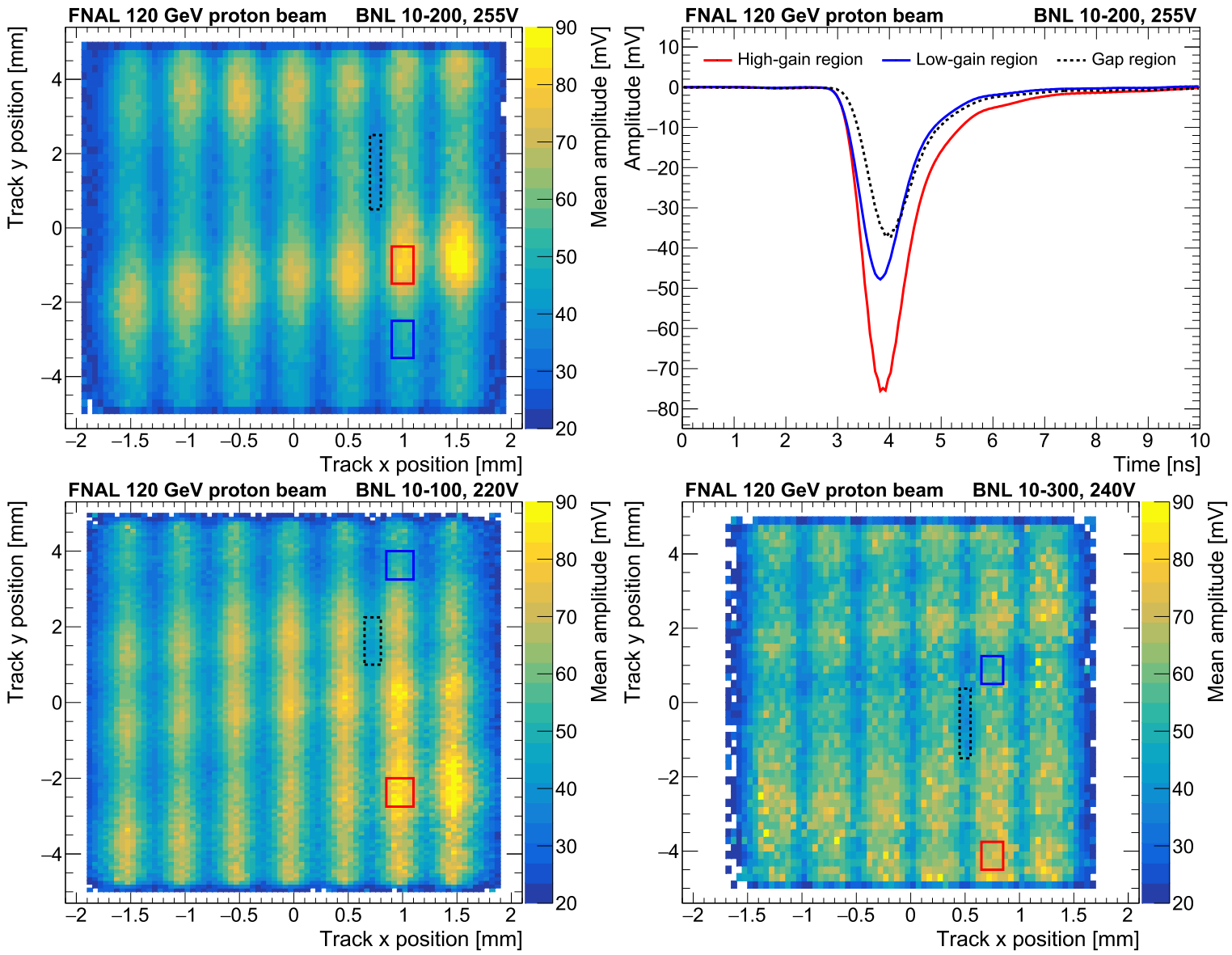

Figure 13.10: Amplitude map of the $1\,\mathrm{cm}$ sensors with varying width of $200\,\mu\mathrm{m}$ (top left), $100\,\mu\mathrm{m}$ (bottom left), and $300\,\mu\mathrm{m}$ (bottom right). The average pulse shapes from regions with different gain from the $200\,\mu\mathrm{m}$ width sensor are presented (top right).

$90\,\mathrm{mV}$, with smaller values in the $300\,\mu\mathrm{m}$ width sensor, attributable to the lower statistics. Significant variations in the signals are detected even along the same strip. This behaviour was determined to come from non-uniformity in the gain layer. Certain regions generate a higher or lower signal, thus denominated *high-gain* and *low-gain regions* represented with red and blue, respectively, in Figure 13.10. The wave forms reveal changes in the risetime and recombination time. This consideration is critical for many performance metrics since the sensors are expected to have their best performance at voltages just below the breakdown. Several inhomogeneities in the gain layer will cause underbiasing in some portions of the sensor, worsening the overall performance. Therefore, the properties of the sensors will depend significantly on the uniformity of the whole active surface. All of the sensors had a signal threshold of $15\,\mathrm{mV}$ to avoid noisy signals.

A more precise description of the reconstruction was implemented. We keep using the reconstruction of Figure 13.3 but in a smaller zone, due to the inaccurate perform-

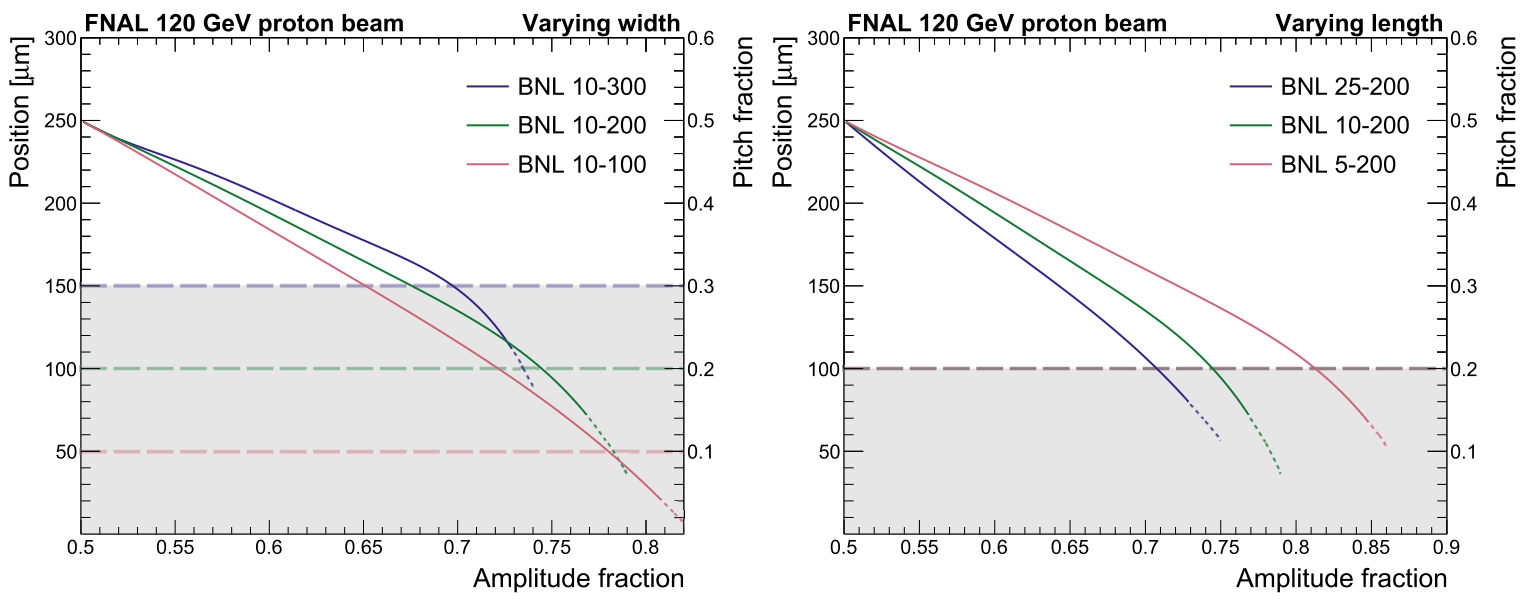

Figure 13.11: Comparison of reconstruction fit for different width (left) and length (right). Grey background depicts the metal edge of the strip. A solid line shows the portion of the fit where the reconstruction is reliable, followed by a dashed part where the binary readout is applied.

ance of the method in the inner metal regions. Figure 13.11 has the fit to the charge fraction profile for all samples. Note that the fit stops working a bit after getting into the metal region. This makes desirable thinner strips to increase the applicability of the reconstruction. Every event with a significant signal in at least two adjacent strips and with an amplitude fraction within the range of use of this fit will have its position reconstructed interpolated as in the previous section. This method will be denoted as *two strip reconstruction*. If at least one of those requirements is not fulfilled, we can't assure the process to be reliable, hence a default method called *one strip reconstruction* is used. This method assumes the hit is in the leading channel. If both methods were fully localized, say all the events in the gap use two strip reconstruction and all events in metal use one strip, then the latter should have a resolution comparable to the binary readout in the metal region, width$/\sqrt{12}$. However, as seen in Figure 13.12, the efficiency of both methods is not full in any of the regions. The efficiency is defined as the ratio of events using one of the methods of reconstruction over the total events in the active area.

The resolutions obtained in the gaps, where the two strip method is dominant, are very uniform and go down to $20\,\mu\mathrm{m}$. The one strip reconstruction, though relatively far from the other method, is also uniform and shows a significant improvement with respect to the original binary readout. A fourth dashed curve is presented with an expected resolution coming from the uncertainty propagation in Equation 13.1. The idealized response gets smaller values than the actual measurement. This is attributed to defects such as

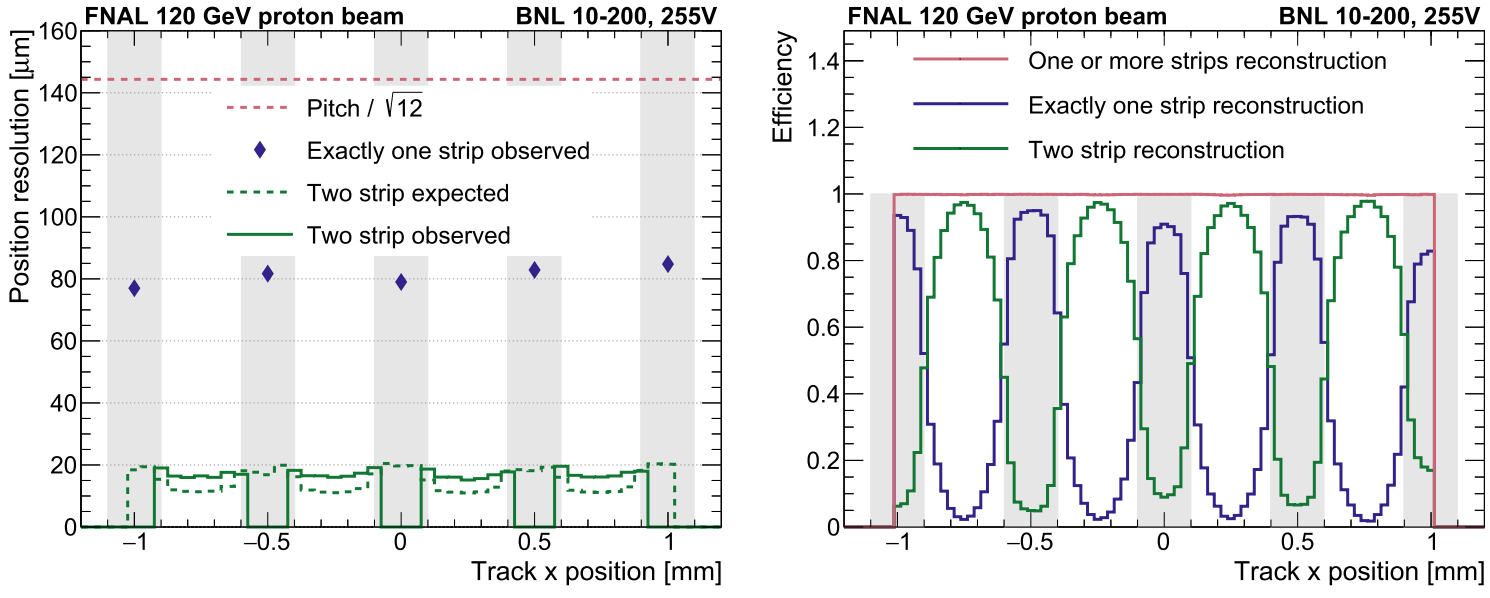

Figure 13.12: BNL $1\,\mathrm{cm}$ length $200\,\mu\mathrm{m}$ metal width results. Position resolution vs x sensor position (left) and efficiency vs x position (right).

the non-uniformity found, specific channel-to-channel variations or contributions from the external tracker. Although both methods give dissimilar results, we observe a tendency to uniform values across the active surface as strips get thinner. This solution also increases the efficiency of the two strip method.

The timing calculation is similar to the one discussed in the previous section. Another fine tuning is added, apart from the reference and channel corrections. An empirical delay map is presented in Figure 13.13. This two-dimensional representation corrects the event time more accurately, similar to the correction per channel. The implementation of this extra layer of detail arose for longer strips, because of the finite velocity of propagation of the signal. Delays of up to $1\,\mathrm{ns}$ were obtained in $2.5\,\mathrm{cm}$ long strips. The impact of these corrections in the time performance is also presented in Figure 13.13. In the plot, the red curve has the resolution without any rectification. In black, the channel-dependent offset is used similarly to the previous batch. Although there is an improvement in the metal section of around $10\,\mathrm{ps}$, the gaps remain problematic. The light blue curve shows the effect of the map correction only with the multi-channel correction introduced in Equation 13.2. The gaps were directly affected with a small effect on the metallic parts. The final curve, in dark green, presents all corrections at the same time, as well as the multi-channel, with a refined algorithm ($i = 2$ in Equation 13.2). Both effects described, in gaps and in metal, are acting together to produce a more uniform response. We report resolution values in the order of $40\,\mathrm{ps}$ for this sensor. This number is averaged over all the surface, including non-uniform parts. Looking at high-gain re-

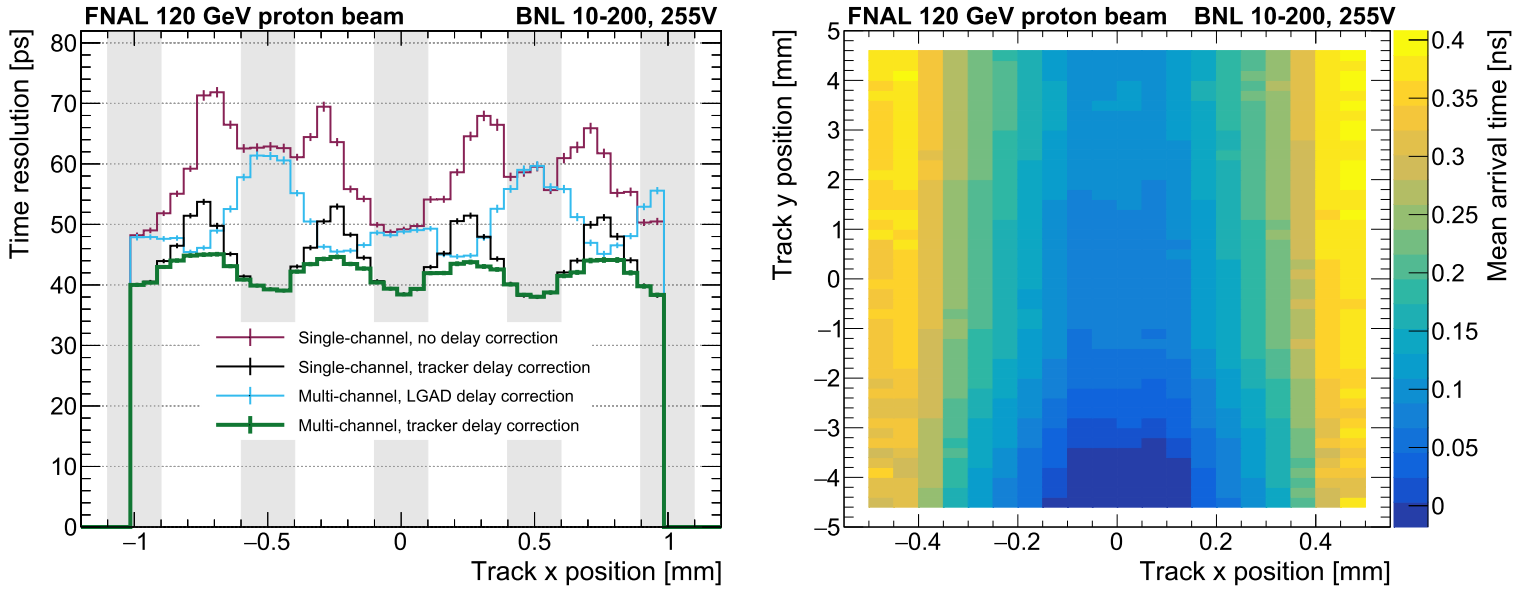

Figure 13.13: BNL $1\,\mathrm{cm}$ length $200\,\mu\mathrm{m}$ metal width results. Time resolution vs x sensor position (left) and delay map (right).

Table 13.2: Summary of spatial and timing performance for the five fully analyzed sensors. The time resolution for the high gain regions is shown. The position resolutions and efficiencies are shown for both the one and two strip categories.

	Time resolution	Spatial resolution			
		Exactly one strip		Two strip	
Name	High gain	Resolution	Eff.	Resolution	Eff.
Unit	ps	µm	-	µm	-
BNL 5–200	30 ± 1	61 ± 1	35%	12 ± 1	65%
BNL 10–100	35 ± 1	69 ± 1	23%	19 ± 1	77%
BNL 10–200	32 ± 1	82 ± 1	43%	18 ± 1	57%
BNL 10–300	36 ± 1	83 ± 1	51%	16 ± 1	49%
BNL 25–200	51 ± 1	128 ± 1	82%	31 ± 1	18%

gions only, the temporal performance is improved to $32\,\mathrm{ps}$. The tracker contribution is estimated to be $10\,\mathrm{ps}$ and is already removed in quadrature.

A summary of the best time resolution in the high-gain region and the detail of each position resolution, as well as the percentage of events using each method, is presented in Table 13.2. The efficiency of the two strip method is increased as the strip width and length are reduced. For longer sensors, thinner strips help in extending the use of the multi-channel reconstruction, though the nominal value seems to get slightly worse. On the other hand, the one strip method tend to the binary readout width$/\sqrt{12}$ value as the length decreases. Time resolutions going down to $30\,\mathrm{ps}$ were obtained even in $1\,\mathrm{cm}$ sensors. The biggest impact comes from the gain layer, so further studies with proper uniformity will be needed to establish a correct limit of the sensor's performance.

Chapter 14

Conclusions

The characterization of several AC-LGAD sensors was performed in two campaigns of data taking developed during 2021 and 2022 using the $120\,\mathrm{GeV}$ proton beam at the Fermilab Test Beam Facility. A series of devices were manufactured by two different institutions: KEK/Tsukuba group in collaboration with Hamamatsu Photonics K.K. (HPK) and Brookhaven National Laboratory (BNL). The former produced sensors with a pad configuration for readout that were tested in the first campaign only. Meanwhile, the latter used a strip configuration with a variety of dimensions, tested along both campaigns.

A framework of analysis was developed to manage the response of the device under study through the oscilloscope and the external tracker information. Several improvements were included since the first campaign, with an emphasis on the proper alignment of the samples with the telescope system.

The first batch of sensors presented an excellent timing performance with time resolutions of about $30\,\mathrm{ps}$ independent of the geometry. The pads had a different composition of the gain layer with a model with higher resistivity that showed a considerable increment in the signal amplitude but a negligible improvement in the position resolution, reaching values slightly higher than $20\,\mu\mathrm{m}$ with both samples. The strip sensors showed an outstanding performance of 6 to $11\,\mu\mathrm{m}$, sometimes limited by the tracker's resolution. Higher signals were reported with increasing pitch. The quantities of interest described were almost unaffected by pitch variations.

The second batch introduced a more detailed methodology of reconstruction and a more extensive study of the effects in variations of strips' length and width. The whole

set of samples presented a non-uniformity of the gain layer, independent of the wafer, detected in the amplitude profile. This issue impacted the overall performance of the sensors, due to an underbiasing in the regions with a lower gain implant. The best timing resolution of $30\,\mathrm{ps}$ was achieved by the shortest sensor with $5\,\mathrm{mm}$ length. The $1\,\mathrm{cm}$ devices had slightly worse values in the high-gain region, with results between 32 and $36\,\mathrm{ps}$. The uniformity issue directly affected the performance of the $2.5\,\mathrm{cm}$ sensor, raising the time to $51\,\mathrm{ps}$. The different lengths also affected the pulse shapes, providing a larger risetime for longer strips that augments the jitter contribution to a level comparable to the reconstruction component.

Two methods of spatial reconstruction were implemented, one with a multi-channel construction identical to the one used in the first campaign and a default that uses single-channel information. The former presented better results consistently, with values ranging from 12 to $19\,\mathrm{\mu m}$ when the method was applicable in more than 50% of the events. Again the longest device presents unsatisfactory results, with more than 80% of the events not able to use the more precise method. As the strip width decreases the resolution gets slightly worse, but the number of events that can use the method increase in a higher proportion, making desirable to work with thinner strips.

Smaller devices tend to present better results, though $1\,\mathrm{cm}$ long samples are not too far from them. Future implementations would be benefited by larger sensors due to cost reasons. Since the increment of about one order of magnitude in the dimensions of the strips has not impacted the performance in the same proportion, a trade off between their capabilities and performance should be evaluated. Furthermore, other factors such as uniformity of the gain layer should be revisited for a proper characterization.

The basic requirements imposed by the collaborations were satisfied in terms of timing performance. Modules for the HL-LHC with these capabilities are in construction. Moreover, there are plans for using these devices not only for time measurements in future upgrades but as first generation 4d-trackers in experiments such as EIC.

References Part I

[1] S. Morán, 'Study of hadronization process using positive pions with CLAS in Jefferson Lab,' 2021.

[2] E. Molina, 'Experimental measurement and phenomenological study of positive pion production in nuclear media.'

[3] J. H. Gao, Z. T. Liang and X. N. Wang, 'Nuclear dependence of azimuthal asymmetry in semi-inclusive deep inelastic scattering,' *Physical Review C - Nuclear Physics*, vol. 81, 6 2010, ISSN: 1089490X. DOI: 10.1103/PhysRevC.81.065211.

[4] J. J. Sakurai, *Modern Quantum Mechanics*. Pearson, 2010.

[5] L. Ananikyan and N. Ivanov, 'Azimuthal asymmetries in DIS as a probe of intrinsic charm content of the proton,' *Nuclear Physics B*, vol. 762, no. 1, pp. 256–283, 2007, ISSN: 0550-3213. DOI: https://doi.org/10.1016/j.nuclphysb.2006.11.008.

[6] A. Bacchetta *et al.*, 'Semi-inclusive deep inelastic scattering at small transverse momentum,' *Journal of High Energy Physics*, vol. 2007, no. 02, p. 093, Feb. 2007. DOI: 10.1088/1126-6708/2007/02/093.

[7] H. Avagyan *et al.*, 'Medium modification of hadronic distributions in SIDIS,' APS Meeting Abstracts, vol. 2014, Sep. 2014.

[8] A. Bacchetta, D. Boer, M. Diehl and P. J. Mulders, 'Matches and mismatches in the descriptions of semi-inclusive processes at low and high transverse momentum,' *Journal of High Energy Physics*, vol. 2008, no. 08, p. 023, Aug. 2008. DOI: 10.1088/1126-6708/2008/08/023.

[9] A. Schäfer, X.-N. Wang and B.-W. Zhang, 'Multiple parton scattering in nuclei: Quark–quark scattering,' *Nuclear Physics A*, vol. 793, no. 1, pp. 128–170, 2007, ISSN: 0375-9474. DOI: https://doi.org/10.1016/j.nuclphysa.2007.06.009.

[10] M. Boglione, J. Collins *et al.*, 'Kinematics of current region fragmentation in semi-inclusive deeply inelastic scattering,' *Physics Letters B*, vol. 766, pp. 245–253, 2017, ISSN: 0370-2693. DOI: https://doi.org/10.1016/j.physletb.2017.01.021.

[11] A. Casher, H. Neuberger and S. Nussinov, 'Chromoelectric-flux-tube model of particle production,' *Phys. Rev. D*, vol. 20, pp. 179–188, 1 Jul. 1979. DOI: 10.1103/PhysRevD.20.179.

[12] S. Ferreres-Solé and T. Sjöstrand, 'The space-time structure of hadronization in the Lund model,' *The European Physical Journal C*, vol. 78, no. 11, Nov. 2018. DOI: 10.1140/epjc/s10052-018-6459-8.

[13] P. Mulders and R. Tangerman, 'The complete tree-level result up to order 1/Q for polarized deep-inelastic leptoproduction,' *Nuclear Physics B*, vol. 461, no. 1, pp. 197–237, 1996, ISSN: 0550-3213. DOI: https://doi.org/10.1016/0550-3213(95)00632-X.

[14] M. Anselmino *et al.*, 'Role of Cahn and Sivers effects in deep inelastic scattering,' *Phys. Rev. D*, vol. 71, p. 074 006, 7 Apr. 2005. DOI: 10.1103/PhysRevD.71.074006.

[15] D. Boer, 'Boer-Mulders function's description webpage http://www.physics4all.nl/BoerMulders.html.'

[16] D. Boer and P. J. Mulders, 'Time-reversal odd distribution functions in leptoproduction,' *Phys. Rev. D*, vol. 57, pp. 5780–5786, 9 May 1998. DOI: 10.1103/PhysRevD.57.5780.

[17] B. Mecking *et al.*, 'The CEBAF large acceptance spectrometer (CLAS),' *Nuclear Instruments and Methods in Physics Research Section A: Accelerators, Spectrometers, Detectors and Associated Equipment*, vol. 503, no. 3, pp. 513–553, 2003, ISSN: 0168-9002. DOI: https://doi.org/10.1016/S0168-9002(03)01001-5.

[18] H. Hakobyan, W. Brooks *et al.*, 'A double-target system for precision measurements of nuclear medium effects,' *Nuclear Instruments and Methods in Physics Research Section A: Accelerators, Spectrometers, Detectors and Associated Equipment*, vol. 592, no. 3, pp. 218–223, 2008, ISSN: 0168-9002. DOI: https://doi.org/10.1016/j.nima.2008.04.055. [Online]. Available: https://www.sciencedirect.com/science/article/pii/S0168900208006098.

[19] T. Mineeva, 'Hadronization studies via pi0 electroproduction off D, C, Fe, and Pb,' 2013.

[20] H. Hakobyan, 'Observation of quark propagation pattern in nuclear medium,' 2008.

[21] A. Bórquez, 'The omega hadronization studies in the nuclear medium with the CLAS spetrometer,' 2021.

[22] S. Morán *et al.*, 'Charged-pion multiplicity ratio measurement with EG2 data,' 2021.

[23] L. Zana, 'Search for the onset of color transparency through rho0 electroproduction on nuclei,' 2010.

[24] T. Sjöstrand, S. Mrenna and P. Skands, 'PYTHIA 6.4 physics and manual,' *Journal of High Energy Physics*, vol. 2006, no. 05, p. 026, May 2006. DOI: 10.1088/1126-6708/2006/05/026.

[25] F. James, *Statistical Methods in Experimental Physics*. Wspc, 2006.

[26] A. Andreassen *et al.*, 'Omnifold: A method to simultaneously unfold all observables,' *Phys. Rev. Lett.*, vol. 124, p. 182 001, 18 May 2020. DOI: 10.1103/PhysRevLett.124.182001.

[27] J. Agarwala *et al.*, 'Contribution of exclusive diffractive processes to the measured azimuthal asymmetries in SIDIS,' *Nuclear Physics B*, vol. 956, p. 115 039, 2020, ISSN: 0550-3213. DOI: https://doi.org/10.1016/j.nuclphysb.2020.115039.

[28] A. Moretti, *TMD observables in unpolarised semi-inclusive DIS at COMPASS*, 2021. arXiv: 2107.10740 [hep-ex].

[29] J. Breitweg *et al.*, 'Measurement of azimuthal asymmetries in deep inelastic scattering,' *Physics Letters B*, vol. 481, no. 2, pp. 199–212, 2000, ISSN: 0370-2693. DOI: https://doi.org/10.1016/S0370-2693(00)00430-5.

[30] S. Chekanov *et al.*, 'Measurement of azimuthal asymmetries in neutral current deep inelastic scattering at HERA,' *The European Physical Journal C*, vol. 51, no. 2, pp. 289–299, May 2007. DOI: 10.1140/epjc/s10052-007-0310-y.

[31] F. Giordano, R. Lamb *et al.*, 'Flavor-dependent azimuthal modulations in unpolarized SIDIS cross section at HERMES,' *Journal of Physics: Conference Series*, vol. 295, no. 1, p. 012 092, May 2011. DOI: 10.1088/1742-6596/295/1/012092.

[32] S. J. Joosten, 'Fragmentation and nucleon structure in semi-inclusive deep-inelastic scattering at the HERMES experiment,' 2013.

[33] G. Fedotov, V. Burkertc, R. Gotheb, V. Mokeeva and I. Skorodumina, 'Analysis report on the ep -> ep pi+ pi- reaction in the CLAS detector with a 2.039 GeV beam for 0.4 GeV2 < Q2 < 1.0 GeV2 and 1.3 GeV < W < 1.825 GeV,' 2017.

References Part II

[34] O. Aberle, I. Béjar Alonso *et al.*, *High-Luminosity Large Hadron Collider (HL-LHC): Technical design report*, ser. CERN Yellow Reports: Monographs. Geneva: CERN, 2020. DOI: 10.23731/CYRM-2020-0010.

[35] A. Abada, M. Abbrescia, S. S. AbdusSalam, I. Abdyukhanov, J. Abelleira Fernandez *et al.*, 'HE-LHC: The High-Energy Large Hadron Collider,' *The European Physical Journal Special Topics*, vol. 228, p. 1382, 2019, ISSN: 1951-6401. DOI: https://doi.org/10.1140/epjst/e2019-900088-6.

[36] R. Heller, C. Madrid, A. Apresyan, W. Brooks, W. Chen, G. D'Amen, G. Giacomini, I. Goya, K. Hara, S. Kita, S. Los, A. Molnar, K. Nakamura, C. Peña, C. San Martín, A. Tricoli, T. Ueda and S. Xie, 'Characterization of BNL and HPK AC-LGAD sensors with a 120 GeV proton beam,' *Journal of Instrumentation*, vol. 17, no. 05, P05001, May 2022. DOI: 10.1088/1748-0221/17/05/P05001.

[37] G. Giacomini, 'Fabrication of Silicon Sensors Based on Low-Gain Avalanche Diodes,' in *Frontiers of Physics*, 2021.

[38] R. L. Workman *et al.*, 'Review of Particle Physics,' *PTEP*, vol. 2022, p. 083C01, 2022. DOI: 10.1093/ptep/ptac097.

[39] E. Currás *et al.*, 'Inverse Low Gain Avalanche Detectors (iLGADs) for precise tracking and timing applications,' *Nuclear Instruments and Methods in Physics Research Section A: Accelerators, Spectrometers, Detectors and Associated Equipment*, vol. 958, p. 162 545, 2020, Proceedings of the Vienna Conference on Instrumentation 2019, ISSN: 0168-9002. DOI: https://doi.org/10.1016/j.nima.2019.162545.

[40] A. Doblas *et al.*, 'Inverse Low Gain Avalanche Detector (iLGAD) periphery design for X-Ray applications,' 2022. arXiv: 2202.01552 [physics.ins-det].

[41] G. Giacomini, W. Chen, G. D'Amen and A. Tricoli, 'Fabrication and performance of AC-coupled LGADs,' *JINST*, 2019.

[42] Q. Sun *et al.*, 'The analog front-end for the LGAD based precision timing application in CMS ETL,' 2020. arXiv: 2012.14526 [physics.ins-det].

[43] Fermilab Test Beam Facility team, 'Silicon telescope webpage https://ftbf.fnal.gov/,' 2022.

[44] S. Kwan, C. Lei, D. Menasce, L. Moroni, J. Ngadiuba, A. Prosser, R. Rivera, S. Terzo, M. Turqueti, L. Uplegger, L. Vigani and M. E. Dinardo, 'The pixel tracking telescope at the Fermilab Test Beam Facility,' *Nucl. Instrum. Methods Phys. Res., A*, vol. 811, 2016.

[45] K. Nakamura1, S. Kita, T. Ueda, K. Hara and H. Suzuki, 'First prototype of finely segmented HPK AC-LGAD detectors,' *JPS Conf. Proc.*, vol. 34, no. 010016, 2021.

[46] A. Apresyan, W. Chen, G. D'Amen, K. D. Petrillo, G. Giacomini, R. Heller, H. Lee, C.-S. Moon and A. Tricoli, 'Measurements of an AC-LGAD strip sensor with a 120 GeV proton beam,' *Journal of Instrumentation*, vol. 15, no. 09, P09038, Sep. 2020. DOI: 10.1088/1748-0221/15/09/P09038.

[47] G. Giacomini, 'LGAD-Based silicon sensors for 4D detectors,' *Sensors*, vol. 23, no. 4, 2023, ISSN: 1424-8220. DOI: 10.3390/s23042132.